CHARACTERISTICS OF COOPERATIVE SPONTANEOUS EMISSION WITH APPLICATIONS TO ATOM MICROSCOPY AND COHERENT XUV RADIATION GENERATION

A Dissertation

by

JUNTAO CHANG

Submitted to the Office of Graduate Studies of
Texas A&M University
in partial fulfillment of the requirements for the degree of

DOCTOR OF PHILOSOPHY

December 2008

Major Subject: Physics

CHARACTERISTICS OF COOPERATIVE SPONTANEOUS EMISSION WITH APPLICATIONS TO ATOM MICROSCOPY AND COHERENT XUV RADIATION GENERATION

A Dissertation

by

JUNTAO CHANG

Submitted to the Office of Graduate Studies of
Texas A&M University
in partial fulfillment of the requirements for the degree of

DOCTOR OF PHILOSOPHY

Approved by:

Co-Chairs of Committee,	M. Suhail Zubairy
	Marlan O. Scully
Committee Members,	George R. Welch
	Andreas Klappenecker
Head of Department,	Edward S. Fry

December 2008

Major Subject: Physics

ABSTRACT

Characteristics of Cooperative Spontaneous Emission

with Applications to Atom Microscopy and Coherent XUV Radiation Generation.

(December 2008)

Juntao Chang, B.S., Peking University;

M.S., Institute of Physics, Chinese Academy of Sciences

Co–Chairs of Advisory Committee: Dr. M. Suhail Zubairy
Dr. Marlan O. Scully

Cooperative effect in the radiation process has been studied in for more than half a century. It is important in the sense of both basic physics and applied science.

In this work, we study the dynamics of the cooperative spontaneous emission from an ensemble of N atoms which is uniformly excited by absorbing a single photon. We reveal that there are two different regimes in which the system exhibits totally different behaviors. One of them is the superradiance type of behavior: the system decays much quicker than single atom decay, with a decay rate proportional to $N(\lambda/R)^2$, where N is the atom numbers, R is the size of the atom cloud, and λ is the wavelength. We call it Markovian regime because the sytem does not persist memory effect. The other regime is called non-Markovian regime and the system oscillates with effective Rabi oscillation frequency Ω while slowly decaying with a rate proportional to the photon escaping rate. The effective Rabi oscillation is a new type of dynamics which analogs well known Cavity QED behavior.

Particularly in the Markovian regime, we study the system dynamics as a many-body eigenfunction and eigenvalue problem. For a dense cloud, we find analytical

solutions for the eigenstates and corresponding eigenvalues, which can help to generally describe the system dynamics for any initial conditions in this regime.

One of the applications is in atom microscopy. We propose a scheme to measure the distance between two atoms/molecules beyond diffraction limit. It covers the whole range from half the wavelength to sub-nanometers, utilizing both the atom localization technique and the collective frequency shift effect due to the cooperative effect in the radiation of the two atoms.

Another application that we propose is to generate Coherent XUV radiation using Raman-type superradaince. We prove that intense short pulses of XUV radiation can be produced by Raman type superradiance from an ensemble of atoms/ions driven by visible or IR laser pulses.

To My Parents: Jibiao Chang and Guoyi Zhao

ACKNOWLEDGMENTS

First of all, many thanks to Dr. M. Suhail Zubairy and Dr. Marlan O. Scully for all the time they have spent with me and all their help, patience, advising, instructions on my research and on my life. I would also thank all the committee members for the guidance and constructive comments during my study and research. Special thanks to Dr. Anatoly Svidzinsky, Dr. Jörg Evers, Dr. Yuri Rostovtsev for fruitful joint work, valuable discussions, and continuous help in conducting my research. It was my great pleasure to work with these people.

Many thanks to Dr. George Welch and Dr. Michael Kash for their help and useful suggestions. Thanks to Dr. Yaping Yang, Dr. Fuli Li and Dr. Shiyao Zhu for their help and advices. Thanks to Dr. Tiegang Di, Dr. Han Xiong and Yu You for all the helps and discussions. Thanks Aihua Zhang, Paul Hsu, Hebin Li, Xi Wang, Dr. Miaochan Zhi for their kindly help in the past five years. And thanks to the Office of Naval Research (Award No. N00014-03-1-0385) and the Robert A. Welch Foundation (Grant No. A-1261), the Air Force Office of Scientific Research, DARPA-QuIST, and the TAMU Telecommunication and Informatics Task Force (TITF) initiative for the support on this research.

Many thanks to Ms. Kimberly Chapin and Mr. Clayton Holle for their cheerful support these years. To all the members of the Institute of Quantum Studies and all my friends in the Physics Department, I thank you for your friendship and your help.

Finally, I would like to thank my family for their support on pursuing my dream in physics.

TABLE OF CONTENTS

CHAPTER Page

LIST OF TABLES

LIST OF FIGURES

FIGURE Page

FIGURE Page

FIGURE Page

FIGURE Page

FIGURE Page

CHAPTER I

INTRODUCTION

In "ordinary" fluorescence phenomena, an ensemble of atoms/molecules (For future convenience, we will indicate them by atoms only in the rest of this paper) initially prepared in the excited state decays spontaneously towards ground states by emitting light. During this process the atoms in the sample can be seen as interacting independently with the radiation field, or in other words, incoherently. This decay takes a characteristic time $\tau \sim \gamma^{-1}$, where γ is the single atom damping rate from the excited state, and the radiation pattern of this atomic sample is essentially isotropic. These features are generally observed in dilute atomic systems.

However, under certain conditions, a collection of atoms can radiate spontaneously much faster and stronger and in a well defined direction depending on the geometry of the sample. This phenomenon, known as superradiance, was first proposed by Dicke [1] in his pioneering work in 1954. He considered theoretically two types of collective radiation phenomena: superradiance and subradiance. Superradiance is the phenomenon that the system radiates to the ground state with a rate much faster (proportional to the atom number N) than that of a single atom. And subradiance is the phenomenon that the system decays very slowly or does not decay at all. His derivation was based on the assumption that all atoms are confined inside a volume which is smaller than one wavelength. He also ignored any possible interactions between atoms.

Since then, the collective or cooperative emission phenomenon has been the subject of a large number of theoretical papers [2, 3, 4, 5, 6, 7]. Eberly and Rehler [4]

The journal model is Physics Reveiw A.

generalized Dicke's description of superradiance to an extended system. Bonifacio and Lugiato brought up the concept of superfluoresecence [6], which describes the cooperative emission from a system of uncorrelated excited atoms. This process is usually started by normal spontaneous emission but later results in correlation within the system. Feld et al. then developed a semiclassical theory for superradiance in an extended, optical thick medium in 1976 [7].

The experimental observations of cooperative emission effects go back at least as far as Hahn's spin echo experiment [8]. Phenomena such as free-induction decay have been observed experimentally afterwards. They can be categorized as "limited superradiance" because only a small fraction of the energy stored in the samples is emitted cooperatively, and the decay of the whole sample is essentially unaffected by it. The development of pulsed dye-laser systems has made it easier to excite a collection of atoms in a very short time. This led to numerous experiments to study superradiance and superfluorescence [9, 10, 11] during the next several decades. The first observation of "strong superradiance" was made in optically pumped HF gas [9] in 1973 by Feld's group in the far infrared region. Later, superradiance emission in the optical [10], infrared [11] and millimeter wave [12] domains was also realized experimentally. One of the most common scenarios of a superradiance experiment would be the following: A collection of atoms is prepared inside a pencil shaped cavity or trap; the atom cloud is fully or partially inverted by an intense pulse laser; after certain delay time τ_D, the system will emit a short radiation burst within the time of the order of τ/N; this process is much faster and stronger than single atom decay.

Cooperative effect in the radiation process is of interest in both fundamental physics and applications. Comparing to laser process, the superradiance phenomenon appears simpler since one can neglect the pumping and relaxation mechanisms and consider only the evolution of atoms by tracing out the coupled radiation field. In

spite of this deceptive simplicity, the phenomenon is actually very complicated and difficult to analyze in detail. It also involves concepts of quantum electrodynamics, many body problem, and non-linear optics. For example, here in this paper, we are going to explore the general description of this system in the language of eigenstates and eigenvalues of a many-body system. There are also interesting questions like quantum fluctuations, radiation trapping caused by random distribution, etc.

From the standpoint of applications, superradiance is interesting as one of the methods to generate coherent emission without coherent pumping. Especially in those regimes like x-ray or γ ray, there are no effective mirrors which have prevented the ordinary stimulated emission process. On the other hand, in the recent advances of quantum informatics, a collection of many two-level particles is suggested to serve as an ideal candidate for Decoherence-Free Subspace (DFS) [13, 14, 15]. More than that, the N two-level atom ensemble with one excitation plays a very important role in quantum memory and quantum networking. Relevant experiments have been carried out by the groups of Lukin [16], Kuzmich [17], Kimble [18], and Vuletić [19] et al.

In this work, we are interested particularly in the time evolution of a specially prepared state obtained by absorption of a single photon [20, 21, 22] in a cloud of N atoms. Similar problems have been of long-standing interest. Dicke [1] first noted the radiation abnormal in this problem. In his words "... the greatest radiation intensity anomaly occurs in the transition to the ground state" [23]. In particular he showed that the collective decay rate for the symmetric state with one excitation is $\Gamma_N = N\gamma$, where he assumed the atomic volume to have smaller dimensions compared with the radiation wavelength. Then Cummings [24] considered the spontaneous emission of a single atom which is initially excited in the presence of $N-1$ initially unexcited identical atoms and M accessible radiation modes. He showed that such an extended system oscillates between the ground state and the excited state with an effective

Rabi frequency $\Omega \sim \sqrt{N}$. Such modification of the spontaneous emission of one atom in the presence of $N-1$ atoms inside a cavity has been studied since then [25, 26]. Buzek [27] studied the dynamics of an excited atom in the presence of $N-1$ unexcited atoms in the free space and predicted that there is a radiation suppression, but he did not report any dynamical oscillations.

In Chapter II, we report novel dynamical oscillations in the evolution of an initial quantum state of the atom cloud, which is prepared by uniformly absorbing a single photon, even without the existence of any optical cavity. We call this an Effective Rabi Oscillation. It is as if the atomic cloud acts to form a new type of "cavity" with the atom cloud volume V replacing the virtual field mode volume $\mathcal{V}_{\rm ph}$ defined by the electromagnetic cavity; in other words, the usual vacuum Rabi frequency $\Omega_{\rm Vac} = (\wp/\hbar)\sqrt{\hbar\omega/(\epsilon_0 \mathcal{V}_{\rm ph})}$ is replaced by $\Omega_0 = (\wp/\hbar)\sqrt{\hbar\omega/(\epsilon_0 V)}$ in the present problem, where $\wp$ is the electric-dipole transition matrix element, $\hbar\omega$ is the photon energy and ϵ_0 is the free space permittivity. The system, if it is in the regime which we call the non-Markovian, will undergo oscillatory decay with a decay rate determined by the photon escape rate. The oscillation frequency equals the effective Rabi oscillations. However, if the oscillation period is much greater then the time of photon flight through the cloud, the atomic state will decay exponentially. This behavior is called single photon superradiance and it is within the usual Markovian limit.

In Chapter III, we study in detail about the dynamics of N-atom cloud with one excitation with more details in the Markovian limit. We derive the equations of motion for the system in the bare state basis. By eliminating the field components in the equations, we are able to obtain the collective damping rate and induced dipole-dipole interaction coefficients between atoms. Then we show that the problem can be reduced to finding the eigenstates of the system evolution. In general, the dynamics

of an arbitrary initial state can be obtained by decomposing it using the eigenstates basis set. For a dense atom cloud, we find analytical solutions for both eigenfuctions and eigenvalues. A similar approach has been used by Ernst [28] without the dipole-dipole interaction term. In addition to that, we show that Fermi's golden rule does not apply to this problem in general, even in the Markovian limit.

Similar to the spontaneous emission process, in the "ordinary" resonant fluorescence experiments, when two well separated atoms or molecules are driven by resonant laser light, each atom emits its own fluorescence light which has a three-peak spectrum (usually it is called Mollow spectrum [29]). However, when the atoms or molecules are close enough to each other, the cooperative effect appears and plays a very important role especially when the inter-atom distance is comparable or shorter than one wavelength. It will modify both the spectrum and intensity-intensity correlation function of the emitted fluorescence light [30, 31, 32, 33, 34, 35, 36, 37, 38, 39, 40].

On the other hand, precise atomic position measurement has been a problem of a great deal of interest for many years. It has many applications such as atom lithography, microscopy and atom imaging. However, due to the optical diffraction, in the classical lens-based far field optical microscopy or imaging, the resolution in the focus plane can not exceed the limit of half the wavelength of the illuminating light. In the past several decades, many methods have been developed to overcome this limit. Lens-based techniques include confocal [41], non-linear femtosecond or stimulated emission depletion microscopy [42]. Also non-classical features such as entanglement [43], quantum interferometry [44] or multi-photon processes [45] can be used to enhance resolution. Somewhat complementary to this, a particularly promising development is the lensless near-field optics, which can achieve nanometer spatial resolution [46]. Another progress was made in 2002 by Hettich et al. [47] following the idea to reach sub-wavelength resolution for non-identical, individually

addressable objects [80].

In Chapter IV, motivated by the idea of localizing single atom inside a standing wave field, we propose a new method to measure the distance betweentwo atoms beyond diffraction limit. Firstly, we investigate the radiation properties of a pair of identical atoms located in a resonant standing wave field, taking account of the cooperative effect. By calculating the collective resonance fluorescence emitted by the pair, we find three different parameter ranges, depending on the distance of the atoms as compared to the transition wavelength. In the small-distance limit, the dynamics is dominated by the dipole-dipole interaction. For large interparticle distances, dipole-dipole coupling is negligible, and the main system dynamics arises from the interaction with the standing wave field. Finally, in the intermediate region, a rich interplay of the various couplings arises, which however is simplified by increasing driving laser field intensity. In each of the cases, we show how to determine the distance of the two particles and their respective positions relative to the nodes of the standing wave field with fractional-wavelength precision. This method relies entirely on far-field measurement techniques. Typically, this scheme will be limited by the difficulties in fixing the position of the two atoms rather than by constraints of the measurement scheme itself, which in principle allows to achieve resolution far below the classical Rayleigh limit of optical microscopy technology. Our results can be applied to physical systems which may be approximated as two-level systems, where the two energy states are connected by an electric-dipole allowed transition. Possible examples include atoms, molecules, or artificial quantum systems such as quantum dots.

Another promising application of the cooperative effect is the generation of coherent XUV radiation using superradiance. As we know, owing to the lack of suitable reflective surfaces, feedback in XUV generation is absent and one must depend on single-pass gain. In Chapter V we discuss the scheme based on Raman-type of super-

radiance. It turns out that the generation of the XUV field from the Raman coherence comes form the same cooperative effect as in Dicke superradiance. It is highly directional and has very short pulse width. The development of ultra-fast pulsed laser technique and multi-photon excitation technique have made it possible to generate the needed Raman coherence in the atomic system. We numerically simulate part of the process.

CHAPTER II

THE DYNAMICAL BEHAVIOR OF THE COOPERATIVE EMISSION FROM AN N-ATOM CLOUD WITH ONE EXCITATION *

In this chapter, we study the dynamics of the correlated spontaneous emission from a dense spherical cloud of N atoms which is uniformly excited at time $t = 0$ by absorbing a single photon. The main result is summarized at Fig. 1. It turns out that there are two different types of dynamical behavior for this system. They are defined by two characteristic time scales: one is the so-called effective Rabi frequency $\Omega \propto \sqrt{N}$ and the other is the time of photon flight through the cloud R/c. If $\Omega R/c \ll 1$, the state exponentially decays with rate $\Omega^2 R/c$ and the state life time is greater then R/c. We call this region Markovian limit and it exhibits the characters of superradiance (the decay rate is $N(\lambda/R)^2$ times faster than single atom decay rate) even there is only one excitation inside the system. In the opposite limit $\Omega R/c \gg 1$, the coupled atom-radiation system oscillates between the collective Timed Dicke state (with no-photons) and the atomic ground state (with one photon) with frequency Ω while it decays at a rate $\propto c/R$. We call this regime Non-Markovian limit and it has features similar to cavity QED but without any assistance of an optical cavity. In the following, we start from the derivation of the interaction Hamiltonian for the system. We then study the system evolution of the initial state prepared by uniformly absorbing one photon in the Timed Dicke (TD) basis.

---

* Reprinted with permission from Anatoly A. Svidzinsky, Jun-Tao Chang, and Marlan O. Scully, Phys. Rev. Lett, 100, 160504 (2008). Copyright (2008) by the American Physical Society.

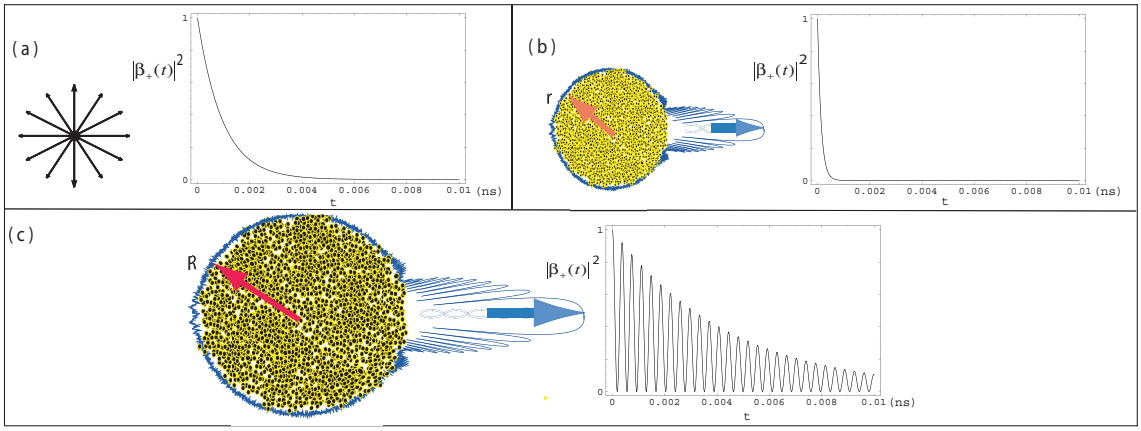

Fig. 1. Comparison of the different dynamical behavior for the correlated spontaneous emission from an N atomic cloud described by the $|+\rangle_{\mathbf{k}_0}$ state of Fig. 2b. The single atom spontaneous decay life time is taken to be $\tau_0 = 10$ ns. We assume that atomic density is $10^{16}\text{cm}^{-3}$and the resonant photon wavelength is $\lambda = 1\mu$m. Plot (a) corresponds to the case when cloud radius is equal to $\lambda/2$, hence the number of atoms is $N_a = 5240$, then the state decay time is $\tau_a = 1.9 \times 10^{-3}$ ns. In plot (b) the cloud radius is $r = 10\lambda$, $N_b = 4.2 \times 10^7$, $\tau_b = 2.7 \times 10^{-4}$ ns. In plot (c) the radius of the atomic cloud is $R = 2$ cm which yields $N_c = 4.2 \times 10^{22}$, $\tau_c = 9 \times 10^{-2}$ ns, while the period of oscillations is 3.7×10^{-3}ns.

A. Atom-field Interaction Hamiltonian

The Hamiltonian of an electron with charge e and mass m interacting with an external electromagnetic field is given by the minimal coupling Hamiltonian [51]

$$\mathcal{H} = \frac{1}{2m}[\hat{\mathbf{p}} - e\mathbf{A}(\mathbf{r}, t)]^2 + eU(\mathbf{r}, t) + V(\mathbf{r})$$

where $\hat{\mathbf{p}}$ is the canonical momentum operator, $\mathbf{A}(\mathbf{r}, t)$ and $U(\mathbf{r}, t)$ are the vector and scalar potentials of the external field, respectively, and $V(\mathbf{r})$ is the electrostatic potential that is normally the atomic binding potential.

We choose the following gauge (Coulomb Gauge/Radiation Gauge)

$$U(\mathbf{r},t)=0 \tag{2.1}$$

$$\nabla\cdot\mathbf{A}=0 \tag{2.2}$$

The system Hamiltonian can be written as

$$\begin{aligned}\mathcal{H} &= \mathcal{H}_F+\frac{1}{2m}[\hat{\mathbf{p}}-e\mathbf{A}(\mathbf{r},t)]^2+V(\mathbf{r})\\ &= \mathcal{H}_F+\frac{p^2}{2m}+V(\mathbf{r})-\frac{e}{2m}(\hat{\mathbf{p}}\cdot\mathbf{A}(\mathbf{r},t)+\mathbf{A}(\mathbf{r},t)\cdot\hat{\mathbf{p}})+\frac{e^2A^2(\mathbf{r},t)}{2m}\\ &= \mathcal{H}_F+\mathcal{H}_A-\frac{e}{2m}(\hat{\mathbf{p}}\cdot\mathbf{A}(\mathbf{r},t)+\mathbf{A}(\mathbf{r},t)\cdot\hat{\mathbf{p}})+\frac{e^2A^2(\mathbf{r},t)}{2m}\end{aligned} \tag{2.3}$$

where $\mathcal{H}_A=\frac{\hat{\mathbf{p}}^2}{2m}+V(\mathbf{r})$ is the unperturbed Hamiltonian of the electron.

So the interaction Hamiltonian is

$$\mathcal{H}_{int}=-\frac{e}{2m}(\hat{\mathbf{p}}\cdot\mathbf{A}(\mathbf{r},t)+\mathbf{A}(\mathbf{r},t)\cdot\hat{\mathbf{p}})+\frac{e^2A^2(\mathbf{r},t)}{2m} \tag{2.4}$$

Next we applying the following approximations:

(I) Dipole Approximation: when $\mathbf{k}\cdot\mathbf{r}'\ll 1$, as

$$\begin{aligned}A(\mathbf{r}_0+\mathbf{r}',t) &= \mathbf{A}(t)exp[i\mathbf{k}\cdot(\mathbf{r}_0+\mathbf{r}')]\\ &= \mathbf{A}(t)exp(i\mathbf{k}\cdot\mathbf{r}_0)(1+i\mathbf{k}\cdot\mathbf{r}'+...)\\ &\simeq \mathbf{A}(t)exp(i\mathbf{k}\cdot\mathbf{r}_0)\\ &= \mathbf{A}(\mathbf{r}_0,t)\,;\end{aligned} \tag{2.5}$$

(II) Low Field Intensity. That is we assume that we can ignore the interaction term $e^2\mathbf{A}^2/2m$ as compared with the term $e\hat{\mathbf{p}}\cdot\mathbf{A}/m$ [52].

Then taking into account that we are using the radiation gauge (2.2), $\hat{\mathbf{p}}$ and $\mathbf{A}(\mathbf{r},t)$ are commuting variables ($\hat{\mathbf{p}}\cdot\mathbf{A}(\mathbf{r},t)=\mathbf{A}(\mathbf{r},t)\cdot\hat{\mathbf{p}}$) [52], we get the simplified

expression for the interaction energy as

$$\mathcal{H}_{int} = -\frac{e}{m}\hat{\mathbf{p}} \cdot \mathbf{A}(\mathbf{r}_0, t)\,, \tag{2.6}$$

Now the interaction of a radiation field with a single-electron atom can be described by the following Hamiltonian in the dipole approximation:

$$\mathcal{H} = \mathcal{H}_F + \mathcal{H}_A + \mathcal{H}_{int}\,, \tag{2.7}$$

where $\mathcal{H}_F$ and $\mathcal{H}_A$ are the energies of the radiation field and the atom, respectively, in the absence of the interaction, and $\mathcal{H}_F = \sum_{\mathbf{k},\lambda}(a_{\mathbf{k},\lambda}a^{\dagger}_{\mathbf{k},\lambda} + \frac{1}{2})\hbar\nu_{\mathbf{k}}$, and $\mathbf{r}$ is the position of the electron, and $\mathcal{H}_{int} = -\frac{e}{m}\hat{\mathbf{p}} \cdot \mathbf{A}(\mathbf{r}_0, t)$ is the interaction energy.

Next we examine the model of two-level atom interaction with radiation field. Let the $|a\rangle$ and $|b\rangle$ represent the upper and lower states of the two-level atom, i.e., they are the eigenstates of the atomic energy Hamiltonian $\mathcal{H}_A$ with the eigenvalues E_a and E_b. Then

$$\begin{aligned}
\mathcal{H}_A &= (|a\rangle\langle a| + |b\rangle\langle b|)\mathcal{H}_A(|a\rangle\langle a| + |b\rangle\langle b|) \\
&= E_a|a\rangle\langle a| + E_b|b\rangle\langle b| \\
&= \frac{1}{2}\hbar\omega(|a\rangle\langle a| - |b\rangle\langle b|) + \frac{1}{2}(E_a + E_b)
\end{aligned} \tag{2.8}$$

where we have used the following complete and orthogonality relations

$$\langle a|b\rangle = 0, \qquad \langle a|a\rangle = \langle b|b\rangle = 1, \qquad |a\rangle\langle a| + |b\rangle\langle b| = 1 \tag{2.9}$$

Define

$$\sigma_z = (|a\rangle\langle a| - |b\rangle\langle b|)/2, \tag{2.10}$$

$$\sigma_+ = |a\rangle\langle b| \tag{2.11}$$

$$\sigma_- = |b\rangle\langle a| \tag{2.12}$$

Then the atomic energy is

$$\mathcal{H}_A = E_0 + \hbar\omega\sigma_z \tag{2.13}$$

The energy of the free field $\mathcal{H}_F$ is given in the terms of the creation and annihilation operators by

$$\mathcal{H}_F = \sum_{\mathbf{k},\lambda} \hbar\nu_k \left(a^\dagger_{\mathbf{k},\lambda} a_{\mathbf{k},\lambda} + \frac{1}{2} \right) . \tag{2.14}$$

The vector potential in equation (2.6) can be expressed as

$$\mathbf{A}(\mathbf{r},t) = \frac{1}{V_{ph}} \sum_{\mathbf{k},\lambda} \left(\frac{\hbar}{2\nu_k \epsilon_0} \right)^{1/2} [\hat{a}_{\mathbf{k},\lambda} \mathcal{E}_{\mathbf{k},\lambda} e^{i[\mathbf{k}\cdot\mathbf{r}_0 - \nu_k(t)]} + h.c.] \tag{2.15}$$

Electron canonical momentum in equation (2.6) is

$$\hat{\mathbf{p}} = \frac{m\dot{\hat{\wp}}}{e} , \tag{2.16}$$

where $\hat{\wp}$ is the atomic dipole moment operator. For an atom, $\hat{\wp}$ is defined as $\hat{\wp} = \sum_i e\hat{\mathbf{r}}_i$ where $\mathbf{r}_i$ is the position of the atomic electron of charge e. For the two level atoms, we can express it as

$$\begin{aligned} \hat{\wp} &= (|a\rangle\langle a| + |b\rangle\langle b|)\hat{\wp}(|a\rangle\langle a| + |b\rangle\langle b|) \\ &= \wp_{aa}|a\rangle\langle a| + \wp_{bb}|b\rangle\langle b| + \wp_{ba}|b\rangle\langle a| + \wp_{ab}|a\rangle\langle b| , \end{aligned} \tag{2.17}$$

where $\wp_{ij}$ is the matrix element of $\langle i|\hat{\wp}|j\rangle$ $(i,j=a,b)$. Due to the parity, $\wp_{aa}=\wp_{bb}=0$.

So the interacting Hamiltonian can be written as

$$\hat{\wp}=\wp_{ba}|b\rangle\langle a|+\wp_{ab}|a\rangle\langle b|=\wp_{ba}\sigma_{-}+\wp_{ba}^{*}\sigma_{+} \tag{2.18}$$

Rate of the change of the dipole moment $\hat{\wp}$ can be obtained from Heisenberg's Equation of motion

$$\begin{aligned}\frac{d\hat{\wp}}{dt} &= \frac{1}{i\hbar}[\hat{\wp},\hat{\mathcal{H}}_A]\\ &= \frac{1}{i\hbar}[\wp_{ba}\sigma_{-}+\wp_{ba}^{*}\sigma_{+},\hbar\omega\sigma_z+E_0]\\ &= -i\omega(\wp_{ba}\sigma_{-}(t)-\wp_{ba}^{*}\sigma_{+}(t))\end{aligned} \tag{2.19}$$

Similarly, we can have

$$\sigma_{-}(t)=\sigma_{-}(0)e^{i\omega t}\,. \tag{2.20}$$

Now, for the convenience of future calculations, we can write the interaction Hamiltonian in the interaction picture

$$\begin{aligned}\mathcal{H}_{int}^{I} &= -\frac{e}{m}\frac{m}{e}\dot{\hat{\wp}}\cdot\mathbf{A}(\mathbf{r}_0,t)\\ &= \frac{i\omega}{\sqrt{V_{ph}}}\sum_{\mathbf{k},\lambda}\left(\frac{\hbar}{2\nu_k\epsilon_0}\right)^{1/2}[\wp_{ba}\cdot\mathcal{E}_{\mathbf{k},\lambda}^{*}\sigma_{-}\hat{a}_{\mathbf{k},\lambda}^{\dagger}e^{-i\mathbf{k}\cdot\mathbf{r}_0}e^{i(\nu_k-\omega)t}+a.c.]\ ,\end{aligned} \tag{2.21}$$

where we have discarded terms oscillating at optical or higher frequencies, because they make negligible contributions after averaging over time interval Δt which is many optical periods. This is known as Rotating Wave Approximation.

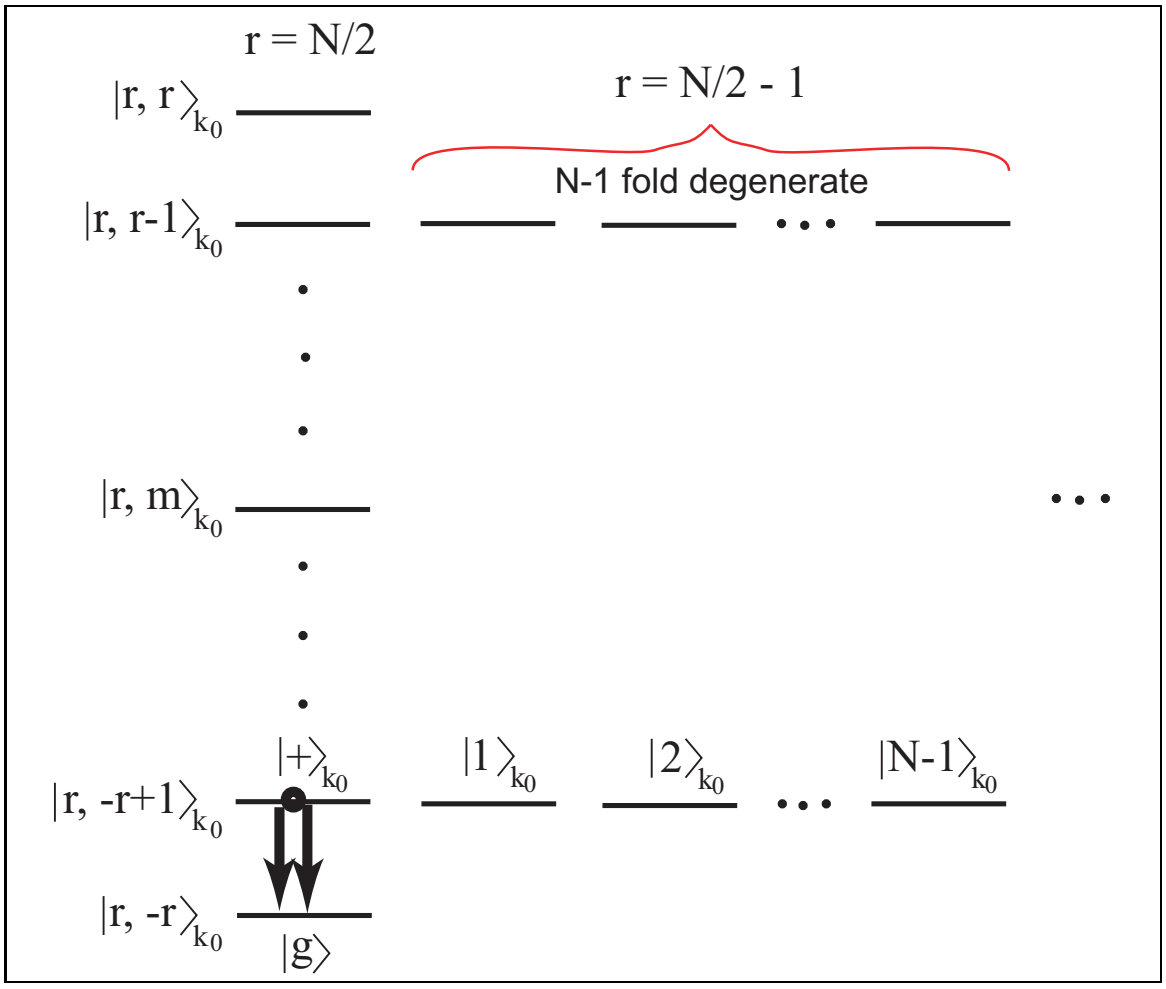

Fig. 2. Timed Dicke states associated with absorption of radiation of wave vector $\mathbf{k}_0$: the initial state $|+\rangle_{\mathbf{k}_0}$ decays directly to the grand state $|g\rangle$.

For N atoms interacting with a common field, ignoring field polarization, we obtain

$$\hat{H}_{\rm int} = \sum_{\mathbf{k}} \sum_{j=1}^{N} g_{\mathbf{k}} \left[\hat{\sigma}_j \hat{a}_k^{\dagger} \exp(i(\nu_k - \omega)t - i\mathbf{k}\cdot\mathbf{r}_j) + \hat{\sigma}_j^{\dagger} \hat{a}_k \exp(-i(\nu_k - \omega)t + i\mathbf{k}\cdot\mathbf{r}_j) \right], \tag{2.22}$$

where, σ_j and σ_j^+ is the σ_- and σ_+ for jth atom, and the coupling constant is

$$g_k = \omega \frac{\wp_{ab}}{\hbar} \sqrt{\frac{\hbar}{\epsilon_0 \nu_k V_{\rm ph}}}\,, \tag{2.23}$$

B. Dynamics of N-Atoms with Single Excitation

We consider a system of N two-level (a excited and b ground) atoms, initially one of them is in the excited state a (with no information which one), $E_a - E_b = \hbar\omega$, and the multi-mode radiation field is in the vacuum. Atoms are located at positions $\mathbf{r}_j$ ($j = 1, ..., N$). The whole set of states can be expressed as those in Fig. 2 [21], where $|j\rangle \ = |b_1, b_2, ..., b_{j-1}, a_j, b_{j+1}...b_N\rangle$ represents the state in which the j^{th} atom is exited but the others are in the ground state and $|g\rangle = |b_1, b_2, ..., b_N\rangle$ is the state with all the atoms in the ground state. The atomic state prepared by uniformly absorbing one single photon with wavevector $\mathbf{k}_0$ is exactly the $|+\rangle_{\mathbf{k}_0}$ state of Fig 3.

The state vector for the atom-field system at time t can be then written as

$$|\Psi(t)\rangle = [\beta_+(t)|+\rangle_{\mathbf{k}_0} + \beta_1(t)|1\rangle_{k_0} + \beta_2(t)|2\rangle_{k_0} + ...$$

$$+\beta_{N-1}(t)|N-1\rangle]|0\rangle + \sum_k \gamma_k(t)|g\rangle|1_k\rangle\,, \tag{2.24}$$

with initial conditions $\beta_+(0) = 1$ and all other probability amplitudes are zero. In the dipole approximation the atom-field interaction is described by the Hamiltonian

$$\hat{H}_{\rm int} = \sum_{\mathbf{k}} \sum_{j=1}^{N} \hbar g_k \left[\hat{\sigma}_j \hat{a}_k^\dagger \exp(i(\omega_k - \omega)t - i\mathbf{k}\cdot\mathbf{r}_j) + \text{adj}\right], \tag{2.25}$$

where $\hat{\sigma}_j$ is the lowering operator for atom j, $\hat{a}_k$ is the photon operator and $g_k = \wp\sqrt{\hbar\omega_k/(\epsilon_0 \mathcal{V}_{\rm ph})}$ is the atom-photon coupling constant for the $\mathbf{k}$ mode, ω_k is the photon frequency and $\omega = ck_0$ is the energy difference between level a and b, c is the speed of light. For simplicity, we neglect the effects of photon polarization. The dynamical

$$
\begin{aligned}
|+\rangle_{\mathbf{k}_0} &= \frac{1}{\sqrt{N}} \sum_j e^{i\mathbf{k}_0\cdot\mathbf{r}_j}|j\rangle \\
|1\rangle_{\mathbf{k}_0} &= \frac{1}{\sqrt{2}}\left[|1\rangle e^{i\mathbf{k}_0\cdot\mathbf{r}_1} - |2\rangle e^{i\mathbf{k}_0\cdot\mathbf{r}_2}\right] \\
|2\rangle_{\mathbf{k}_0} &= \frac{1}{\sqrt{6}}\left[|1\rangle e^{i\mathbf{k}_0\cdot\mathbf{r}_1} + |2\rangle e^{i\mathbf{k}_0\cdot\mathbf{r}_2} - 2|3\rangle e^{i\mathbf{k}_0\cdot\mathbf{r}_3}\right] \\
&\;\;\vdots \\
|N-1\rangle_{\mathbf{k}_0} &= \frac{1}{\sqrt{(N-1)N}}[|1\rangle e^{i\mathbf{k}_0\cdot\mathbf{r}_1} + |2\rangle e^{i\mathbf{k}_0\cdot\mathbf{r}_2} + \cdots \\
&\quad + |N-1\rangle e^{i\mathbf{k}_0\cdot\mathbf{r}_{N-1}} - (N-1)|N\rangle e^{i\mathbf{k}_0\cdot\mathbf{r}_N}]
\end{aligned}
$$

Fig. 3. Timed Dicke states associated with absorption of radiation of wave vector $\mathbf{k}_0$: the timed Dicke states corresponding to single photon excitations.

evolution is then totally determined by the Schrödinger's equation. Plugging the state vector and interaction Hamiltonian into the Schrödinger's equation, we get the equation of motion as the following:

$$\begin{aligned}\dot{\beta}_+ &= -\int dt' \sum_{\vec{k}} g_k^2 e^{-ic(|\vec{k}|-k_a)(t-t')} \times \sum_j e^{i[(\vec{k}-\vec{k}_0)\cdot\vec{r}_j]} \\ &\times\Big\{ \frac{\beta_+(t')}{\sqrt{N\cdot N}} \left(e^{-i(\vec{k}-\vec{k}_0)\cdot\vec{r}_1} + e^{-i(\vec{k}-\vec{k}_0)\cdot\vec{r}_2} + ... + e^{-i(\vec{k}-\vec{k}_0)\cdot\vec{r}_N} \right) \\ &+ \frac{\beta_1(t')}{\sqrt{N\cdot 2}} \left(e^{-i(\vec{k}-\vec{k}_0)\cdot r_1} - e^{-i(\vec{k}-\vec{k}_0)\cdot\vec{r}_2} \right) + ... \\ &+ \frac{\beta_{N-1}(t')}{\sqrt{N(N-1)}} \left(e^{-i(\vec{k}-\vec{k}_0)\cdot\vec{r}_1} + ... + e^{-i(\vec{k}-\vec{k}_0)\cdot\vec{r}_{N-1}} - (N-1)e^{-i(\vec{k}-\vec{k}_0)\cdot\vec{r}_N} \right) \Big\},\end{aligned} \tag{2.26}$$

where $k_a = \omega/c$. We proceed by noting that $\sum_j e^{i(\vec{k}-\vec{k}_0)\cdot\vec{r}_j} \Rightarrow \delta(\vec{k}-\vec{k}_0)$ and all of the subradiant trapping states $\beta_1, ...\beta_{N-1}$ in Eq. 2.26 vanish, which, will be explained in next chapter, indicates that there is no Agarwal-Fano coupling [53]. And we now find [21]

$$\begin{aligned}\dot{\beta}_+(t) = -\frac{1}{N}\int_0^t dt' \sum_{\mathbf{k}} \sum_{i,j=1}^{N} g_{\mathbf{k}}^2 \exp[i(\omega_k-\omega)(t'-t)] \\ \cdot \exp[i(\mathbf{k}-\mathbf{k}_0)\cdot(\mathbf{r}_i-\mathbf{r}_j)]\beta_+(t').\end{aligned} \tag{2.27}$$

1. Non-Markovian Behavior: Effective Rabi Oscillation and Photon Escape Time

For a dense cloud one can treat the atom distribution as continuous, we then have $\sum_{i,j} \to (N/V)^2 \int d\mathbf{r} \int d\mathbf{r}'$, where $V = 4\pi R^3/3$ is the volume of the spherical atomic cloud. The summation over $\mathbf{k}$ can also be replaced by integration

$$\sum_{\mathbf{k}} \to \mathcal{V}_{\rm ph}/(2\pi)^3 \int d\mathbf{k}, \tag{2.28}$$

where $\mathcal{V}_{\rm ph}$ is the photon volume. Then the equation of motion reads

$$\begin{aligned}\dot{\beta}_+(t) = -\frac{\mathcal{V}_{\rm ph}}{(2\pi)^3}\frac{N}{V^2}\int d\mathbf{k}\int d\mathbf{r}\int d\mathbf{r}' g_k^2 \int_0^t dt' \beta_+(t') \\ \cdot \exp[i(\omega_k-\omega)(t'-t) + i(\mathbf{k}-\mathbf{k}_0)\cdot(\mathbf{r}-\mathbf{r}')]\,.\end{aligned} \tag{2.29}$$

In the limit $R \to \infty$ integration over $\mathbf{r}'$ gives the delta-function

$$\int d\mathbf{r}' \exp[-i(\mathbf{k}-\mathbf{k}_0)\mathbf{r}'] = (2\pi)^3 \delta(\mathbf{k}-\mathbf{k}_0),$$

and thus we obtain

$$\dot{\beta}_+(t) = -N\Omega_0^2 \int_0^t dt' \beta_+(t')\,, \tag{2.30}$$

where we have defined $\Omega_0 = (\wp/\hbar)\sqrt{\hbar\omega/(\epsilon_0 V)}$, which is like vacuum Rabi frequency but with atomic volume V replacing photon volume $\mathcal{V}_{\rm ph}$.

Differentiating both sides of Eq. (2.30) yields a harmonic oscillator equation

$$\ddot{\beta}_+(t) + \Omega^2 \beta_+(t) = 0, \tag{2.31}$$

where $\Omega = \sqrt{N}\Omega_0$ is an effective Rabi frequency. Therefore in the limit $R \to \infty$ the atomic state undergoes harmonic oscillations with the effective Rabi frequency Ω

$$\beta_+(t) = \cos(\Omega t). \tag{2.32}$$

To find a solution of Eq. (3.84) at finite R, but yet $k_0 R \gg 1$, we rewrite it as

$$\dot{\beta}_+(t) = -\frac{2\mathcal{V}_{\rm ph} N}{\pi V^2} \int d\mathbf{k} g_k^2 \int_0^t dt' \beta_+(t') e^{i(\omega_k - \omega)(t'-t)} S(\mathbf{k}, R)^2, \tag{2.33}$$

where

$$\begin{aligned} S(\mathbf{k}, R) &= \frac{1}{4\pi} \int_V d\mathbf{r} \exp[i(\mathbf{k}-\mathbf{k}_0)\mathbf{r}] \\ &= \frac{\sin(|\mathbf{k}-\mathbf{k}_0|R)}{|\mathbf{k}-\mathbf{k}_0|^3} - \frac{R\cos(|\mathbf{k}-\mathbf{k}_0|R)}{|\mathbf{k}-\mathbf{k}_0|^2}. \end{aligned} \tag{2.34}$$

Next we approximate $g_k^2 \approx g_{k_0}^2$ and replace integration over $\mathbf{k}$ by integration over $\mathbf{p} = \mathbf{k} - \mathbf{k}_0$. The main contribution to the integral comes from the region $p \ll R^{-1}$. That is under the exponent one can replace $k - k_0 \simeq \mathbf{k}_0 \cdot \mathbf{p}/k_0$. Then Eq. (2.33) reads

$$\dot{\beta}_+(t) = -\frac{2}{\pi} N\Omega_0^2 \int d\mathbf{p} \int_0^t dt' \beta_+(t') e^{[ic\mathbf{k}_0 \cdot \mathbf{p}(t'-t)/k_0]}$$

$$\left[\frac{\sin(pR)}{p^3}-\frac{R\cos(pR)}{p^2}\right]^2. \tag{2.35}$$

Integration over directions of $\mathbf{p}$ yields

$$\dot{\beta}_+(t)=-\frac{8}{c}N\Omega_0^2\int_0^\infty pdp\int_0^t dt'\beta_+(t')$$
$$\cdot\frac{\sin[cp(t'-t)]}{(t'-t)}\left[\frac{\sin(pR)}{p^3}-\frac{R\cos(pR)}{p^2}\right]^2. \tag{2.36}$$

To integrate over p we use the following formula

$$\int_0^\infty pdp\frac{\sin[cp(t'-t)]}{(t'-t)}\left[\frac{\sin(pR)}{p^3}-\frac{R\cos(pR)}{p^2}\right]^2=$$
$$\begin{cases}\frac{\pi c}{96}\left[16R^3+12cR^2(t'-t)-c^3(t'-t)^3\right], & c|t'-t|<2R\\ 0, \quad \text{otherwise}\end{cases} \tag{2.37}$$

which gives

$$\dot{\beta}_+(t)=-\frac{1}{16}N\Omega_0^2\int_0^t dt'\beta_+(t')\left[16+12\frac{c}{R}(t'-t)\right.$$
$$\left.-\frac{c^3}{R^3}(t'-t)^3\right]\Theta\left[c(t'-t)+2R\right]. \tag{2.38}$$

Next we note that the function $16+12\frac{c}{R}(t'-t)-\frac{c^3}{R^3}(t'-t)^3$ and its derivative over t' is equal to zero when $c(t'-t)+2R=0$. Taking derivative of both sides of Eq. (2.38) twice we obtain:

$$\dddot{\beta}_+(t)=-N\Omega_0^2\left\{\dot{\beta}_+(t)-\frac{3c}{4R}\beta_+(t)-\right.$$
$$\left.\frac{3c^3}{8R^3}\int_0^t dt'\beta(t')(t'-t)\Theta\left[c(t'-t)+2R\right]\right\}. \tag{2.39}$$

Next we assume that

$$N\Omega_0^2\frac{R^2}{c^2}\gg 1, \quad \text{or} \quad \frac{\Omega R}{c}\gg 1. \tag{2.40}$$

Then one can omit the last term in Eq. (2.39) which yields

$$\dddot{\beta}_+(t)+\Omega^2\dot{\beta}_+(t)-\frac{3c\Omega^2}{4R}\beta_+(t)=0. \tag{2.41}$$

Solution of Eq. (2.41) under the condition (2.40) is given by

$$\beta_+(t) = \cos(\Omega t) \exp\left(-\frac{3c}{8R}t\right), \tag{2.42}$$

which describes rapid oscillations with the effective Rabi frequency Ω superimposed by the exponential decay. The state decays during the time of the photon flight through the atomic cloud. The emitted photon is reabsorbed and reemitted many times before it leaves the cloud.

2. Markovian Limit

In the opposite limit, $\Omega R/c \ll 1$, one can use the Markovian approximation. We integrate Eq. (2.38) over t' assuming $\beta_+(t')$ is a slow varying function of t' and approximate $\beta_+(t') \approx \beta_+(t)$. Then for $t > 2R/c$ we obtain

$$\dot{\beta}_+(t) = -\Gamma\beta_+(t), \tag{2.43}$$

which yields an exponentially decaying solution

$$\beta_+(t) = \beta_+(0)e^{-\Gamma t}. \tag{2.44}$$

Here $\Gamma = 3\Omega^2 R/4c = 27N\gamma/8(k_0R)^2$ and $\gamma = (\omega^3\wp_{ab}^2)/(6\pi\epsilon_0\hbar c^3)$ is the spontaneous decay rate for one atom.

For the distribution of the emitted photon we find

$$\gamma_{\mathbf{k}}(t) = \frac{ig_k\sqrt{N}\left[e^{-\Gamma t + ic(k-k_0)t} - 1\right]}{\Gamma - ic(k-k_0)} \exp\left[-\frac{(\mathbf{k}-\mathbf{k}_0)^2R^2}{4}\right]. \tag{2.45}$$

In particular, for $k = k_0$ we obtain

$$\gamma_{k_0}(t) = \frac{ig_k\sqrt{N}}{\Gamma}\left[e^{-\Gamma t} - 1\right] \exp\left[-k_0^2R^2\sin^2(\theta/2)\right], \tag{2.46}$$

where θ is the angle between $\mathbf{k}$ and $\mathbf{k}_0$. Eq. (2.46) shows that the photon is emitted

in the diffraction angle $\theta \sim 2/k_0 R = \lambda_0/\pi R$.

In this limit, the decay rate $\Gamma \sim R\Omega^2/c \approx (3/4\pi)N\gamma(\lambda^2/R^2)$ can be understood from a simple physical consideration. If we prepare the $|+\rangle_{k_0}$ state for N atoms then Dicke-like arguments [1] for a coherent decay would yield the decay rate of $N\gamma$. However the spontaneous decay rate γ is due to emission in all (random) directions, while the $|+\rangle_{k_0}$ state emits photon mostly in the direction $\mathbf{k}_0$. This directional emission reduces the cooperative decay rate due to reduction of the phase volume in which photon is emitted. The rate γ corresponds to the decay into the number of photon states $V4\pi k_0^2 dk/(2\pi)^3$, while the $|+\rangle_{k_0}$ state decays only into $Rdk/2\pi$ states. Hence the reduction factor due to the difference in the density of states is

$$\frac{Rdk}{2\pi}\frac{(2\pi)^3}{V4\pi k_0^2 dk} = \frac{\pi R}{Vk_0^2} = \frac{3}{4\pi}\frac{\lambda^2}{R^2}. \tag{2.47}$$

Multiplying this by $N\gamma$ we obtain Γ for the total decay rate. The decay rate Γ is smaller then $N\gamma$ in the factor of $\lambda^2/R^2 \ll 1$, where λ is the wavelength of the emitted light. This factor is essentially the ratio of the solid diffraction angle in which the photon is emitted to 4π sr.

C. Discussion

The effective Rabi frequency $\Omega = \sqrt{N}\Omega_0$ we found from quantum mechanical consideration can be written as $\Omega = \sqrt{(3/4\pi^2)\gamma\omega(N/V)\lambda^3} = \sqrt{n\omega\wp_{ab}^2/\epsilon_0\hbar}$. This result is analogous to the plasma frequency and can be obtained in a classical model by treating atoms as classical harmonic oscillators [54]. Indeed, replacing the electric-dipole transition matrix element by $\wp_{ab} = e \cdot d$, where $d = \sqrt{\hbar/m\omega}$ is the oscillator length, yields precisely the plasma frequency $\Omega = \sqrt{ne^2/m\epsilon_0}$.

Relevant experiments have been carried out by the groups of Lukin [16], Kuzmich

[17], Kimble [18] and Vuletić [19] et al. For realistic physical situations such as $n = 10^{14}\text{cm}^{-3}$, $\omega/2\pi = 6 \times 10^{14}\text{Hz}$, $R = 10$ cm ($N = 4 \times 10^{17}$) and $|\wp_{ab}| = 10^{-29}\text{C}\cdot\text{m}$, we obtain that the state decay is accompanied by a few oscillations with the effective Rabi frequency $\Omega \approx 2 \times 10^{10}\text{Hz}$ and the decay time is about $R/c \sim 3 \times 10^{-10}\text{s}$. One can observe a crossover to the exponentially decaying regime, e.g., by decreasing the size of the atomic cloud.

In summary, we study correlated spontaneous emission of a totally symmetric N-atom state prepared by an absorption of a single photon. This is an extension of the result obtained in Refs. [20, 21]. Decay of such a state occurs via photon emission in the direction of the incident photon for large enough density. We found that time evolution of the initial state depends on the relation between an effective Rabi frequency $\Omega \propto \sqrt{N} g_{k_0}$ and the time of photon flight through the cloud R/c. If $\Omega R/c < 1$ the state exponentially decays with the rate $\Omega^2 R/c$ which is determined by the Dicke superradiance rate $N\gamma$ reduced by the factor of λ^2/R^2 due to smaller finite state phase volume in the case of directional emission. In the opposite limit $\Omega R/c \gg 1$ the decay is accompanied by oscillations with the effective Rabi frequency Ω and the decay time is given by R/c.

CHAPTER III

SINGLE PHOTON SUPERRADIANCE AND SUBRADIANCE FROM AN N-ATOM CLOUD *

In this chapter, we consider the Markovian regime of the emission of a single photon from a N-atom cloud with one excitation inside it. For a dense cloud, this problem is reduced to finding eigenfunctions and eigenvalues of an integral equation. Once the eigenfunctions and eigenvalues are determined, the system dynamics at arbitrary initial states can be obtained by decomposing it into different eigenstates. For a spherically symmetric atomic cloud we present an exact analytical solution for eigenvalues and eigenstates. We noticed that some states decay much faster then the single atom decay rate, corresponding to the superradiance (SD) states. While other states are trapped or undergo very slow decay and they are the so called subradiance state.

In section A we derive the equations of motion of the system and induced atom-atom interaction coefficients between two atoms, inducing both the induced dipole-dipole interaction coefficient and the collective damping rate. Then we transformed the problem of the system dynamics to an eigenequation of the system; In section B we solve the eigenvalues and eigenfunctions for the equation analytically; In section C we provide the numerical results for two limiting regimes: Dicke limit and large ensemble limit; At the end, as a complementary introduction, we discuss the condition for applying Femi's Golden Rule to such a many body radiation problem. The details of solving the integral equation in section C will be presented in Appendix A.

---

* Reprinted with permission from Anatoly A. Svidzinsky and Jun-Tao Chang, Phys. Rev. A, 77, 043833 (2008) . Copyright (2008) by the American Physical Society.

A. Collective Damping and Cooperative Energy Shift

For a dense cloud, Ernst [28] studied it under the track of Weisskopf and Wigner approximation and Ressayre and Tallet [55] and Andreev [56] etc also studied it under different approximations. However, In all these previous work, only the collective damping effect was included. It is well known that, when the inter-atomic distances comes small, which is the case for dense cloud, there is dipole-dipole interaction induced by the exchange of photons with the common electromagnetic field [57].

We consider a system of two level (a and b) atoms, initially one of them is in the excited state a and $E_a - E_b = \hbar\omega$. Initially there are no photons. Atoms are located at positions $\mathbf{r}_j$ $(j = 1, ..., N)$. In the dipole approximation the interaction of atoms with photons is described by the Hamiltonian (we disregard polarization effects)

$$\hat{H}_{\rm int} = \sum_{\mathbf{k}} \sum_{j=1}^{N} g_k (\hat{\sigma}_j e^{-i\omega t} + \hat{\sigma}_j^{\dagger} e^{i\omega t}) \left(\hat{a}_k^{\dagger} e^{i\nu_k t - i\mathbf{k}\cdot\mathbf{r}_j} + \hat{a}_k e^{-i\nu_k t + i\mathbf{k}\cdot\mathbf{r}_j} \right), \tag{3.1}$$

where $\hat{\sigma}_j$ is the lowering operator for atom j, $\hat{a}_k$ is the photon operator and g_k is the atom-photon coupling constant for the k mode [**?**]

$$g_k = \omega \frac{\wp}{\hbar} \sqrt{\frac{\hbar}{\epsilon_0 \nu_k V_{\rm ph}}}, \tag{3.2}$$

where $\wp$ is the electric-dipole transition matrix element and $V_{\rm ph}$ is the photon volume. Please note that we do not make the rotating wave approximation in Eq. (3.1).

We look for a solution of the Schrödinger equation for the atoms and the field as a superposition of Fock states

$$\begin{aligned} \Psi = & \sum_{j=1}^{N} \beta_j(t) |b_1 b_2 ... a_j ... b_N > | \, 0 > + \sum_{\mathbf{k}} \gamma_{\mathbf{k}}(t) |b_1 b_2 ... b_N > |1_{\mathbf{k}} > \\ & + \sum_{m<n} \sum_{\mathbf{k}} \alpha_{mn,\mathbf{k}}(t) |b_1, b_2, ... a_m, ... a_n, .. b_N \rangle |1_{\mathbf{k}}\rangle, \end{aligned} \tag{3.3}$$

where $\alpha_{mn,\mathbf{k}} = \alpha_{nm,\mathbf{k}}$. States in the first sum correspond to zero number of photons, while in the second sum the photon occupation number is equal to one and all atoms are in the ground state b. The third term corresponds to presence of two excited atoms inside the cloud and one (virtual) photon with "negative" energy. Substitute of Eq. (3.3) into the Schrödinger equation yields the following equations for $\beta_j(t)$, $\gamma_k(t)$ and $\alpha_{mn,\mathbf{k}}(t)$ (we put $\hbar = 1$)

$$\dot{\beta}_j(t) = -i\sum_{\mathbf{k}} g_k\gamma_k(t)\exp[-i(\nu_k-\omega)t + i\mathbf{k}\cdot\mathbf{r}_j] - i\sum_{\mathbf{k}} g_k \sum_{j'=1,j'\neq j}^{N} \alpha_{jj',\mathbf{k}} e^{i\mathbf{k}\cdot\mathbf{r}_{j'}} e^{-i(\nu_k+\omega)t}, \tag{3.4}$$

$$\dot{\gamma}_{\mathbf{k}}(t) = -i\sum_{j=1}^{N} g_k\beta_j(t)\exp[i(\nu_k-\omega)t - i\mathbf{k}\cdot\mathbf{r}_j], \tag{3.5}$$

$$\dot{\alpha}_{mn,\mathbf{k}}(t) = -ig_k\beta_n(t)\exp[i(\nu_k+\omega)t - i\mathbf{k}\cdot\mathbf{r}_m] + (n \longleftrightarrow m). \tag{3.6}$$

Next we introduce a new function

$$\xi_{\mathbf{k},j}(t) = \sum_{j'=1,j'\neq j}^{N} \alpha_{jj',\mathbf{k}}(t) e^{i\mathbf{k}\cdot(\mathbf{r}_{j'}+\mathbf{r}_j)}. \tag{3.7}$$

Then Eqs. (3.6) and (3.4) yield

$$\dot{\xi}_{\mathbf{k},m} = -i\sum_{n=1,n\neq m}^{N} g_k\beta_n(t)\exp[i(\nu_k+\omega)t+i\mathbf{k}\cdot\mathbf{r}_n] - i(N-1)g_k\beta_m(t)\exp[i(\nu_k+\omega)t+i\mathbf{k}\cdot\mathbf{r}_m]. \tag{3.8}$$

$$\dot{\beta}_j(t) = -i\sum_{\mathbf{k}} g_k\gamma_k(t)\exp[-i(\nu_k-\omega)t + i\mathbf{k}\cdot\mathbf{r}_j] - i\sum_{\mathbf{k}} g_k\xi_{\mathbf{k},j}(t)[-i(\nu_k+\omega)t - i\mathbf{k}\cdot\mathbf{r}_j], \tag{3.9}$$

Integrating Eqs. (3.5) and (3.6) over time gives [$\gamma_k(0) = 0$, $\xi_{\mathbf{k},j}(0) = 0$]

$$\gamma_{\mathbf{k}}(t) = -i\int_0^t dt' \sum_{j=1}^{N} g_k\beta_j(t')\exp[i(\nu_k-\omega)t' - i\mathbf{k}\cdot\mathbf{r}_j], \tag{3.10}$$

$$\xi_{\mathbf{k},m}(t) = -i \sum_{n=1,n\neq m}^{N} \int_0^t dt' g_k \beta_n(t') \exp[i(\nu_k+\omega)t' + i\mathbf{k}\cdot\mathbf{r}_n]$$

$$-i(N-1) g_k \int_0^t dt' \beta_m(t') \exp[i(\nu_k+\omega)t' + i\mathbf{k}\cdot\mathbf{r}_m]. \tag{3.11}$$

Substituting this into Eq. (3.9) we obtain equation for $\beta_j(t)$

$$\dot{\beta}_j(t) = -\sum_{\mathbf{k}} \sum_{j'=1}^{N} \int_0^t dt' g_k^2 \beta_{j'}(t') e^{i(\nu_k-\omega)(t'-t)+i\mathbf{k}\cdot(\mathbf{r}_j-\mathbf{r}_{j'})}$$

$$-\sum_{\mathbf{k}} \sum_{j'=1,j'\neq j}^{N} \int_0^t dt' g_k^2 \beta_{j'}(t') e^{i(\nu_k+\omega)(t'-t)-i\mathbf{k}\cdot(\mathbf{r}_j-\mathbf{r}_{j'})} - (N-1) \sum_{\mathbf{k}} g_k^2 \int_0^t dt' \beta_j(t') e^{i(\nu_k+\omega)(t'-t)}. \tag{3.12}$$

Next we assume that initially the system is prepared in an eigenstate and the state decays exponentially, that is

$$\beta_j(t) = \beta_j e^{-\lambda_n t}, \tag{3.13}$$

where $\mathrm{Re}(\lambda_n) > 0$. Substitute Eq. (3.13) into Eq. (3.12) and integrating over t' yields

$$\lambda_n \beta_j = -i\beta_j \sum_{\mathbf{k}} g_k^2 \left(\frac{1 - e^{-i(\nu_k-\omega+i\lambda_n)t}}{\nu_k - \omega + i\lambda_n} \right) - i(N-1)\beta_j \sum_{\mathbf{k}} g_k^2 \left(\frac{1 - e^{-i(\nu_k+\omega+i\lambda_n)t}}{\nu_k + \omega + i\lambda_n} \right)$$

$$-i \sum_{\mathbf{k}} \sum_{j'=1,j'\neq j}^{N} g_k^2 \left[\left(\frac{1 - e^{-i(\nu_k-\omega+i\lambda_n)t}}{\nu_k - \omega + i\lambda_n} \right) e^{i\mathbf{k}\cdot(\mathbf{r}_j-\mathbf{r}_{j'})} + \left(\frac{1 - e^{-i(\nu_k+\omega+i\lambda_n)t}}{\nu_k + \omega + i\lambda_n} \right) e^{-i\mathbf{k}\cdot(\mathbf{r}_j-\mathbf{r}_{j'})} \right] \beta_{j'}. \tag{3.14}$$

Next we replace summation over $\mathbf{k}$ by integration and obtain

$$\lambda_n \beta_j = -\frac{2iV_{\mathrm{ph}}}{(2\pi)^3} \beta_j \int d^3\mathbf{k} g_k^2 \left(\frac{1 - e^{-i(\nu_k-\omega+i\lambda_n)t}}{\nu_k - \omega + i\lambda_n} \right) - (N-1) \frac{2iV_{\mathrm{ph}}}{(2\pi)^3} \beta_j \int d^3\mathbf{k} g_k^2 \left(\frac{1 - e^{-i(\nu_k+\omega+i\lambda_n)t}}{\nu_k + \omega + i\lambda_n} \right)$$

$$-\frac{2iV_{\mathrm{ph}}}{(2\pi)^3} \int d^3\mathbf{k} \sum_{j'=1,j'\neq j}^{N} g_k^2 \left[\left(\frac{1 - e^{-i(\nu_k-\omega+i\lambda_n)t}}{\nu_k - \omega + i\lambda_n} \right) e^{i\mathbf{k}\cdot(\mathbf{r}_j-\mathbf{r}_{j'})} + \left(\frac{1 - e^{-i(\nu_k+\omega+i\lambda_n)t}}{\nu_k + \omega + i\lambda_n} \right) e^{-i\mathbf{k}\cdot(\mathbf{r}_j-\mathbf{r}_{j'})} \right] \beta_{j'} \tag{3.15}$$

where V_{ph} is the photon quantization volume. Integration over $\mathbf{k}$ directions gives

($\nu_k = ck$, $k_0 = \omega/c$)

$$\lambda_n \beta_j = -\frac{iV_{\rm ph}}{\pi^2 c}\beta_j \int_0^\infty dk k^2 g_k^2 \left(\frac{1-e^{-ic(k-k_0+i\lambda_n/c)t}}{k-k_0+i\lambda_n/c}\right)$$
$$-(N-1)\frac{iV_{\rm ph}}{\pi^2 c}\beta_j \int_0^\infty dk k^2 g_k^2 \left(\frac{1-e^{-ic(k+k_0+i\lambda_n/c)t}}{k+k_0+i\lambda_n/c}\right)$$

$$-\frac{iV_{\rm ph}}{\pi^2 c}\int_0^\infty dk k^2 g_k^2 \sum_{j'\neq j}^{N}\left[\frac{1-e^{-ic(k-k_0+i\lambda_n/c)t}}{k-k_0+i\lambda_n/c}+\frac{1-e^{-ic(k+k_0+i\lambda_n/c)t}}{k+k_0+i\lambda_n/c}\right]\frac{\sin(k|\mathbf{r}_j-\mathbf{r}_{j'}|)}{k|\mathbf{r}_j-\mathbf{r}_{j'}|}\beta_{j'}. \tag{3.16}$$

Next we make an assumption of slow decay (Markovian approximation) and put $\lambda_n \approx 0$ under the integral. This is valid provided $\lambda_n R/c \ll 1$, where R is the size of the atomic cloud. We also take $t \to \infty$ and obtain

$$\lambda_n \beta_j = -\frac{iV_{\rm ph}}{\pi^2 c}\beta_j \int_0^\infty dk k^2 g_k^2 \left(\frac{1}{k-k_0-i0}\right) - (N-1)\frac{iV_{\rm ph}}{\pi^2 c}\beta_j \int_0^\infty dk k^2 g_k^2 \left(\frac{1}{k+k_0-i0}\right)$$

$$-\frac{iV_{\rm ph}}{\pi^2 c}\sum_{j'\neq j}^{N}\int_0^\infty dk k^2 g_k^2 \left[\frac{1}{k-k_0-i0}+\frac{1}{k+k_0-i0}\right]\frac{\sin(k|\mathbf{r}_j-\mathbf{r}_{j'}|)}{k|\mathbf{r}_j-\mathbf{r}_{j'}|}\beta_{j'}. \tag{3.17}$$

Further we apply the relation [58]:

$$\frac{1}{x-i0} = P\frac{1}{x} + i\pi\delta(x),$$

where P stands for the Cauchy principle part. Then one can rewrite Eq. (3.24) as

$$\lambda_n \beta_j = -\frac{i\gamma}{\pi k_0}\beta_j \int_0^\infty dk k \left(P\frac{1}{k-k_0} + i\pi\delta(k-k_0)\right)$$
$$-\frac{i\gamma}{\pi k_0}(N-1)\beta_j \int_0^\infty dk k \left(P\frac{1}{k+k_0} + i\pi\delta(k+k_0)\right)$$

$$-\frac{i\gamma}{\pi k_0}\sum_{j'\neq j}^{N}\int_0^\infty dk\left[P\frac{1}{k-k_0}+i\pi\delta(k-k_0)+P\frac{1}{k+k_0}+i\pi\delta(k+k_0)\right]\frac{\sin(k|\mathbf{r}_j-\mathbf{r}_{j'}|)}{|\mathbf{r}_j-\mathbf{r}_{j'}|}\beta_{j'}, \tag{3.18}$$

where $\gamma=(k_0^3\wp^2)/(\pi\epsilon_0\hbar)$ is the single atom decay rate. The integral over dk in last term can be transformed into an integral from $-\infty$ to ∞ as

$$\begin{aligned}\int_0^\infty dk\left[P\frac{1}{k-k_0}+i\pi\delta(k-k_0)+P\frac{1}{k+k_0}+i\pi\delta(k+k_0)\right]\sin(k|\mathbf{r}_j-\mathbf{r}_{j'}|)\\ =\int_{-\infty}^\infty dk\left(P\frac{1}{k-k_0}+i\pi\delta(k-k_0)\right)\sin(k|\mathbf{r}_j-\mathbf{r}_{j'}|)\\ =\frac{1}{2i}\int_{-\infty}^\infty dk\left(\frac{\exp(ik|\mathbf{r}_j-\mathbf{r}_{j'}|)}{k-k_0-i0}-\frac{\exp(-ik|\mathbf{r}_j-\mathbf{r}_{j'}|)}{k-k_0-i0}\right).\end{aligned} \tag{3.19}$$

Integration over k in Eq. (3.84) is performed by contour method. For the first term we close the integration contour in the upper half-plane of complex k, while for the second term in the lower half-plane. Integration of the second term gives zero. As a result, Eq. (3.85) yields

$$\begin{aligned}\lambda_n\beta_j=-\frac{i\gamma}{\pi k_0}\beta_j\int_0^\infty dkk\left[P\frac{1}{k-k_0}+P\frac{N-1}{k+k_0}\right]\\ +\gamma\beta_j-i\gamma\sum_{j'\neq j}^{N}\frac{\exp(ik_0|\mathbf{r}_j-\mathbf{r}_{j'}|)}{k_0|\mathbf{r}_j-\mathbf{r}_{j'}|}\beta_{j'}.\end{aligned} \tag{3.20}$$

The first term in Eq. (3.87) corresponds to a frequency shift by the same value for all eigenstates of the problem. This constant shift will be ignored in the following discussion. Finally we obtain

$$\lambda_n\beta_j=\gamma\beta_j-i\gamma\sum_{j'\neq j}\frac{\exp(ik_0|\mathbf{r}_j-\mathbf{r}_{j'}|)}{k_0|\mathbf{r}_j-\mathbf{r}_{j'}|}\beta_{j'}. \tag{3.21}$$

Inclusion of light polarization changes the kernel of Eq. (3.21). Such general equation has been considered for the case of two identical atoms in [59, 60] and for N atoms in [61, 62, 63].

B. Eigenfunctions and Eigenvalues for a Dense Cloud

For a dense cloud one can go to the continuous limit, then the eigenvalue equation (3.21) reads

$$-i\gamma\frac{N}{V}\int d\mathbf{r}'\frac{\exp(ik_0|\mathbf{r}-\mathbf{r}'|)}{k_0|\mathbf{r}-\mathbf{r}'|}\beta(\mathbf{r}')=\lambda_n\beta(\mathbf{r}), \tag{3.22}$$

or

$$\gamma\frac{N}{V}\int d\mathbf{r}'\left[\frac{\sin(k_0|\mathbf{r}-\mathbf{r}'|)}{k_0|\mathbf{r}-\mathbf{r}'|}-i\frac{\cos(k_0|\mathbf{r}-\mathbf{r}'|)}{k_0|\mathbf{r}-\mathbf{r}'|}\right]\beta(\mathbf{r}')=\lambda_n\beta(\mathbf{r}), \tag{3.23}$$

where $V=4\pi R^3/3$ is the volume of the atomic spherical cloud. We assume that atoms are uniformly distributed with density N/V.

To find solution of Eq. (3.80) we note that

$$|\mathbf{r}-\mathbf{r}'|=\sqrt{r^2+r'^2-2rr'(\hat{r}\cdot\hat{r}')}, \tag{3.24}$$

where $\hat{r}$ and $\hat{r}'$ are unit vectors in the directions of $\mathbf{r}$ and $\mathbf{r}'$ respectively, and use the following identity [64]

$$\frac{\exp(ik_0|\mathbf{r}-\mathbf{r}'|)}{k_0|\mathbf{r}-\mathbf{r}'|}=4\pi i\sum_{k=0}^{\infty}\sum_{s=-k}^{k}Y_{ks}(\hat{r})Y_{ks}^*(\hat{r}')\begin{cases} j_k(k_0r')h_k^{(1)}(k_0r), & r>r' \\ j_k(k_0r)h_k^{(1)}(k_0r'), & r\le r' \end{cases}, \tag{3.25}$$

where

$$j_k(z)=\sqrt{\frac{\pi}{2z}}J_{k+1/2}(z), \quad h_k^{(1)}(z)=\sqrt{\frac{\pi}{2z}}H_{k+1/2}^{(1)}(z) \tag{3.26}$$

are the spherical Bessel functions,

$$H_k^{(1)}(x)=J_k(x)+iY_k(x)$$

are the Hankel functions of the first kind, $J_{k+1/2}(x)$ and $Y_{k+1/2}(x)$ are Bessel functions of the first and the second kind respectively and $Y_{nm}(\hat{r})\equiv Y_{nm}(\theta,\varphi)$ are spherical harmonic functions.

We look for $\beta(\mathbf{r})$ in the form

$$\beta(\mathbf{r}) = \beta(r) Y_{nm}(\hat{r}). \tag{3.27}$$

Taking into account Eqs. (3.25) and (3.27) we obtain

$$4\pi\gamma \frac{N}{V} \int d\mathbf{r}' \beta(r') Y_{nm}(\hat{r}') \sum_{k=0}^{\infty} \sum_{s=-k}^{k} Y_{ks}(\hat{r}) Y_{ks}^*(\hat{r}') \begin{cases} j_k(k_0 r') h_k^{(1)}(k_0 r), & r > r' \\ j_k(k_0 r) h_k^{(1)}(k_0 r'), & r \leq r' \end{cases} =$$

$$\lambda_n \beta(r) Y_{nm}(\hat{r}). \tag{3.28}$$

One can perform integration over directions of $\mathbf{r}'$ using the orthogonality condition for spherical harmonic functions

$$\int d\Omega_{r'} Y_{ls}^*(\hat{r}') Y_{nm}(\hat{r}') = \delta_{nl} \delta_{sm} \tag{3.29}$$

which yields

$$4\pi\gamma \frac{N}{V} \int_0^R dr' r'^2 \beta(r') \begin{cases} j_n(k_0 r') h_n^{(1)}(k_0 r), & r > r' \\ j_n(k_0 r) h_n^{(1)}(k_0 r'), & r \leq r' \end{cases} = \lambda_n \beta(r). \tag{3.30}$$

In Appendix A we obtain analytical solution of the integral Eq. (3.30). The eigenfunctions are given by

$$\beta(\mathbf{r}) = j_n\left(a k_0 r\right) Y_{nm}(\hat{r}), \tag{3.31}$$

where

$$a = \sqrt{1 - \frac{i}{\tilde{\lambda}_n}}, \quad \tilde{\lambda}_n = \frac{k_0^3 R^3}{3\gamma N} \lambda_n. \tag{3.32}$$

Eigenvalues λ_n are determined from the following equation for a

$$a = \frac{j_n\left(a k_0 R\right)}{j_{n-1}\left(a k_0 R\right)} \frac{h_{n-1}^{(1)}(k_0 R)}{h_n^{(1)}(k_0 R)}. \tag{3.33}$$

For $n = 0$

$$j_0(x) = \frac{\sin(x)}{x}, \quad j_{-1}(x) = \frac{\cos(x)}{x}, \tag{3.34}$$

$$h_0^{(1)}(x) = \frac{e^{ix}}{ix}, \quad h_{-1}^{(1)}(x) = \frac{e^{ix}}{x}, \tag{3.35}$$

and Eq. (3.33) reduces to

$$a = i\tan(ak_0R). \tag{3.36}$$

1. Dicke Limit $k_0R \ll 1$

In the Dicke limit we have

$$\frac{h_{n-1}^{(1)}(k_0R)}{h_n^{(1)}(k_0R)} \approx i\frac{(k_0R)^{2n}}{[(2n-1)!!]^2} + \begin{cases} 0, & n = 0 \\ \frac{k_0R}{2n-1}, & n > 0 \end{cases}. \tag{3.37}$$

Next we keep only the imaginary part in the right hand side of Eq. (3.37). Then Eq. (3.33) reduces to

$$aj_{n-1}(ak_0R) \approx i\frac{(k_0R)^{2n}}{[(2n-1)!!]^2} j_n(ak_0R). \tag{3.38}$$

Using the identity

$$\frac{d}{dx}(xj_{n-1}(x)) = nj_{n-1}(x) - xj_n(x) \tag{3.39}$$

we expand the left hand side of Eq. (3.38) near $ak_0R = A_{nl}$, where A_{nl} is a positive zero of the Bessel function $j_{n-1}(x)$. We find

$$-A_{nl}(ak_0R - A_{nl}) = i\frac{(k_0R)^{2n+1}}{[(2n-1)!!]^2} \tag{3.40}$$

and therefore

$$a \approx \frac{A_{nl}}{k_0R} - i\frac{(k_0R)^{2n}}{A_{nl}[(2n-1)!!]^2} \tag{3.41}$$

Hence the corresponding eigenvalues are

$$\tilde{\lambda}_{nl} \approx -\frac{i(k_0R)^2}{A_{nl}^2} + \frac{2(k_0R)^{2n+3}}{A_{nl}^4[(2n-1)!!]^2}, \tag{3.42}$$

and

$$\lambda_{nl} \approx -\frac{3i\gamma N}{A_{nl}^2 k_0 R} + \frac{6\gamma N (k_0 R)^{2n}}{A_{nl}^4 [(2n-1)!!]^2}, \tag{3.43}$$

$$\beta_{nlm}(\mathbf{r}) = j_n \left(A_{nl} \frac{r}{R} \right) Y_{nm}(\hat{r}). \tag{3.44}$$

In particular, $A_{0l} = (1+2l)\pi/2$ and $A_{1l} = \pi l$, $l > 0$. In the long wavelength limit ($k_0 R \ll 1$) only eigenvalues with $n = 0$ have large real part and decay fast (Dicke superradiance [1]), while eigenvalues with $n > 0$ are suppressed by a factor $(k_0 R)^{2n}$. Those states are trapped.

One should note that

$$\sum_{l=0}^{\infty} \mathrm{Re}(\lambda_{0l}) = \sum_{l=0}^{\infty} \frac{6\gamma N}{A_{0l}^4} = \gamma N, \tag{3.45}$$

as expected from general arguments.

2. Limit $k_0 R \gg 1$

Let us now consider the limit $k_0 R \gg 1$. In this case $\tilde{\lambda}_n \gg 1$ and $|a-1| \ll 1$. We rewrite Eq. (3.33) as

$$a j_{n-1}(a k_0 R)\, h_n^{(1)}(k_0 R) - j_n(a k_0 R)\, h_{n-1}^{(1)}(k_0 R) = 0 \tag{3.46}$$

and then expand Eq. (3.46) near $a = 1$, we obtain

$$h_n^{(1)} j_{n-1}(k_0 R) + h_n^{(1)}(k_0 R)(n \cdot j_{n-1}(k_0 R) - k_0 R \cdot j_n(k_0 R)) \cdot (a-1)$$

$$-h_{n-1}^{(1)}(k_0 R) j_n(k_0 R) - h_{n-1}^{(1)}(k_0 R)(-k_0 R \cdot j_{n+1}(k_0 R) + n \cdot j_n(k_0 R))(a-1) = 0\,. \tag{3.47}$$

Eq. (3.47) yields

$$a = 1 + \frac{i}{-n \cdot i + (k_0 R)^3 \cdot (h_{n-1}^{(1)}(k_0 R) j_{n+1}(k_0 R) - h_n^{(1)}(k_0 R) j_n(k_0 R))}\,. \tag{3.48}$$

Taking into account (3.32) and (3.26), and apply the asymptotic of Bessel function:

$$J_n(x) \approx \left(\frac{2}{\pi x}\right)^{1/2} \left[\cos(x - n\pi/2 - \pi/4) - \frac{4n^2-1}{8x}\sin(x - n\pi/2 - \pi/4)\right], \quad (3.49)$$

$$Y_n(x) \approx \left(\frac{2}{\pi x}\right)^{1/2} \left[\sin(x - n\pi/2 - \pi/4) + \frac{4n^2-1}{8x}\cos(x - n\pi/2 - \pi/4)\right], \quad (3.50)$$

we obtain

$$\lambda_n \approx \frac{3\gamma N}{2(k_0R)^2}\left(1 + \frac{i(-1)^n}{2k_0R} exp(2ik_0R)\right). \quad (3.51)$$

One can see that in the limit $k_0R \gg 1$ the contribution from the extra $\cos x/x$ term in the kernel is smaller by a factor $1/k_0R$ then those from the $\sin x/x$ piece.

To get complete solutions for possible eigenvalues and eigenfunctions, we need to consider the case that $|a| \not\sim 1$. In the following, I give analytical solutions for the $n = 0$ case. Similar approach can be applied to higher oder eigenvalues[66].

For $n = 0$, the equation we need to solve is as the following:

$$a = i\tan(ak_0R) \quad (3.52)$$

or

$$a = i\tan(as) \quad (3.53)$$

where $s = k_0R$.

From Eq. (3.53), we have

$$\tan(as) = -ia\,. \quad (3.54)$$

From the definition of inverse tangential function (arctan), we have

$$as = \arctan(-ia) + l\pi \quad \text{where } l \text{ is arbitrary integer.} \quad (3.55)$$

Noticed that (8) is correct because we have $(-ia)^2 \neq -1$. The reason of that is if

$(-ia)^2 = -1$, then $a = \pm 1$, since s is a real number, then Eq.(3.54) can not be true.

Now, suppose $y = -ia$, then $a = iy$, Eq. (3.54) comes to be

$$iys = \arctan(y) + l\pi \,. \tag{3.56}$$

From the mathematic handbook [65],

$$\begin{aligned} \arctan y &= y - \frac{y^3}{3} + \frac{y^5}{5} - \frac{z^7}{7} + ... \qquad (|y| \leqslant 1 \& y^2 \neq -1) && (3.57) \\ &= \frac{\pi}{2} - \frac{1}{y} + \frac{1}{3y^3} - \frac{1}{5y^5} + ... \qquad (|y| \geqslant 1 \& y^2 \neq -1) && (3.58) \end{aligned}$$

Next, if $|y| \leqslant 1$, then Eq. (3.56)

$$iys = (y - \frac{y^3}{3} + \frac{y^5}{5} - \frac{z^7}{7} + ...) + l\pi \,. \tag{3.59}$$

Then the first order approximation can be written as

$$iy_0 s = y_0 + l\pi \,, \tag{3.60}$$

which then gives

$$y_0 = \frac{l\pi}{is - 1} \,. \tag{3.61}$$

Please notice to satisfy $|y| \leqslant 1$, we have to have $l\pi \leqslant \sqrt{s^2 + 1}$, in the case that $s \gg 1$, it is approximately $l\pi \leqslant s$.

Under this situation, $a = iy_0 = \frac{l\pi(s-i)}{s^2+1}$

$$1 - a^2 \approx \frac{s^4 - l^2\pi^2 s^2 + 2l^2\pi^2 si}{s^4} \tag{3.62}$$

The corresponding eigenvalue (0^{th} approximation)

$$\lambda^0_{0,l} = \frac{3iN}{s^3(1 - a^2)} = \frac{3iN}{-i(s^3 - l^2\pi^2 s) + 2l^2\pi^2} \,. \tag{3.63}$$

Plot $\lambda^0_{0,l}$ *v.s.* l ($l < s/\pi$), we get Fig. 4.

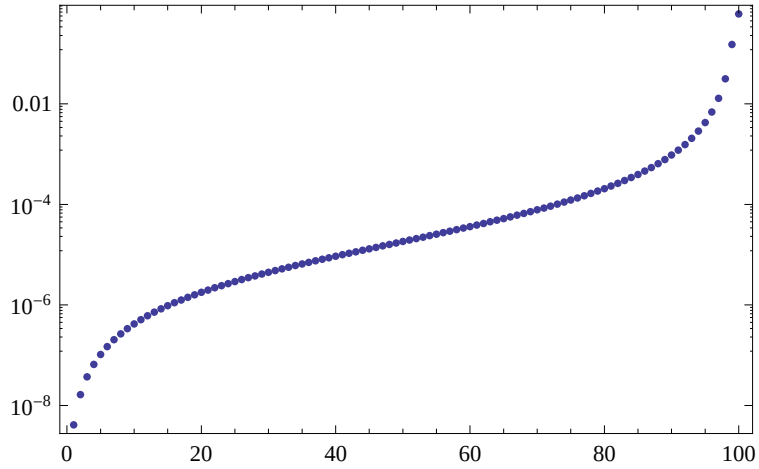

Fig. 4. The real part of the eigenvalues $\lambda_{0,l}/(3N\gamma/(2s^2))$ for l from 1 to 100, where $s = 99.75 * \pi$.

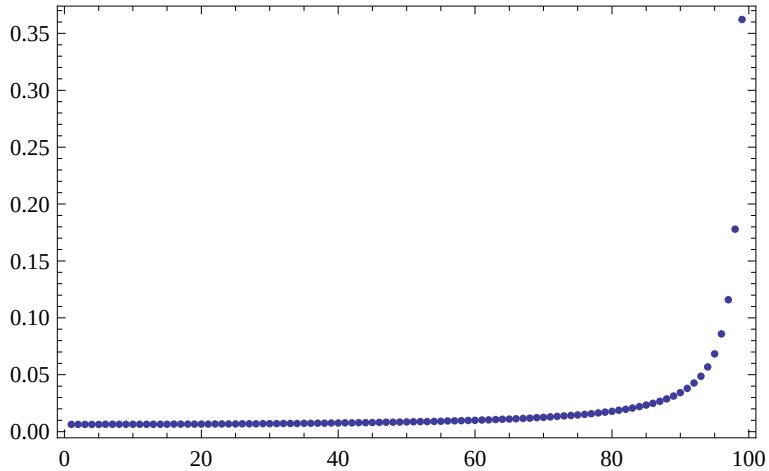

Fig. 5. The imaginary part of the eigenvalues $\lambda_{0,l}/(3N\gamma/(2s^2))$ for l from 1 to 100,where $s = 99.75 * \pi$.

We can even get higher accuracy by easily including the first order correction very easily:

$$iy_1 s = y_1 - \frac{y_1^3}{3} + l\pi \tag{3.64}$$

Solve this equation, and take the solution which satisfies $|y_1| < 1$, we get

$$\begin{aligned} y_1 &= -\frac{(1+i\sqrt{3})(81n\pi+\sqrt{6561n^2\pi^2+4(-9+9is)^3})^{(1/3)}}{62^(1/3)} \\ &+ \frac{(1-i\sqrt{3})(-9+9is)}{(32^(2/3)(81n\pi+\sqrt{6561n^2\pi^2+4(-9+9is)^3})^{1/3}}\,. \end{aligned} \tag{3.65}$$

Then we can substitute y_1 into Eq. (3), thus get the eigenvalue $\lambda_{0,l}$. Plot it regarding to l from 1 to 100, we get the same distribution as in Fig. 4.

Now, we go to the region $|y| > 1$, then we have

$$iys = (\frac{\pi}{2} - \frac{1}{y} + \frac{1}{3y^3} - \frac{1}{5y^5} + ...) + l\pi \tag{3.66}$$

first, we take the zero's order approximation,

$$iy_0 s = \frac{\pi}{2} + l\pi\,, \tag{3.67}$$

which gives

$$y_0 = \frac{\frac{\pi}{2} + l\pi}{is}\,. \tag{3.68}$$

Since $|y_0| \geqslant 1$, we have $l\pi > s - \frac{\pi}{2}$.

However, if we calculate the corresponding eigenvalues, it gives

$$\lambda^0_{0,l} = \frac{3iN}{s^3 - (\frac{\pi}{2} + l\pi)^2 s} \tag{3.69}$$

which is pure imaginary. We know that this is not even close to the real physical situation, so we have to include the first order corrections:

$$iy_1 s = \frac{\pi}{2} - \frac{1}{y_1} + l\pi\ . \tag{3.70}$$

We get

$$y_1^{1,2} = \frac{1}{2}(-i(\frac{\frac{\pi}{2} + l\pi}{s}) \pm \sqrt{-\frac{\pi^2}{s^2}(\frac{1}{2}+l)^2 + 4i\frac{1}{s}}) \tag{3.71}$$

Since $|y_1| > 1$, we take

$$y_1 = \frac{1}{2}(-i(\frac{\frac{\pi}{2}+l\pi}{s}) - \sqrt{-\frac{\pi^2}{s^2}(\frac{1}{2}+l)^2 + 4i\frac{1}{s}}) \tag{3.72}$$

Then the corresponding eigenvalues can be expressed

$$\begin{aligned} \lambda^1_{0,l} &= \frac{3iN}{s^3(1-a^2)} = \frac{3iN}{s^3(1+y_1^2)} \\ &= \frac{3iN}{s^3(1+(\frac{1}{2}(-i(\frac{\frac{\pi}{2}+l\pi}{s}) - \sqrt{-\frac{\pi^2}{s^2}(\frac{1}{2}+l)^2 + 4i\frac{1}{s}}))^2)} . \end{aligned} \tag{3.73}$$

Again, here we require $l\pi > s - \frac{\pi}{2}$. Plot the real and imaginary part of $\lambda^1_{0,l}$ for $l > 100$, we get Fig. 6 and Fig. 7.

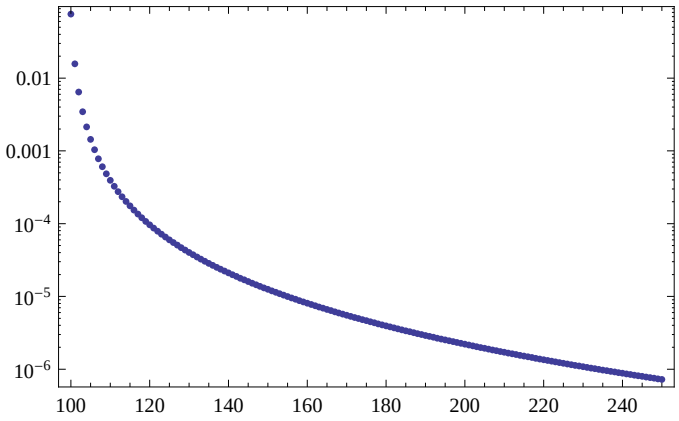

Fig. 6. The real part of the eigenvalues $\lambda_{0,l}/(3N\gamma/(2s^2))$ for l from 101 to 250, where $s = 99.75 * \pi$.

Put Fig. 4 and Fig. 6, Fig. 5 and Fig. 7, together, we get the distribution of the eigenvalues $\lambda_{0,l}/(3N\gamma/(2s^2))$ regarding to l in the full region, Fig. 8 and Fig. 9.

Next, we can check the behavior of the the analytical solutions regarding to the changing of the size (s)of the cloud.

Fig. 10 are the plots based on Eq. (3.65) for $l = 1, 2,$ and 3. The Y-axis indicates the magnitude of the damping rate (the real part of the eigenvalues) in the unit of $3N\gamma$. The X-axis is the size of the atomic cloud ($s = k_0R$). Please notice

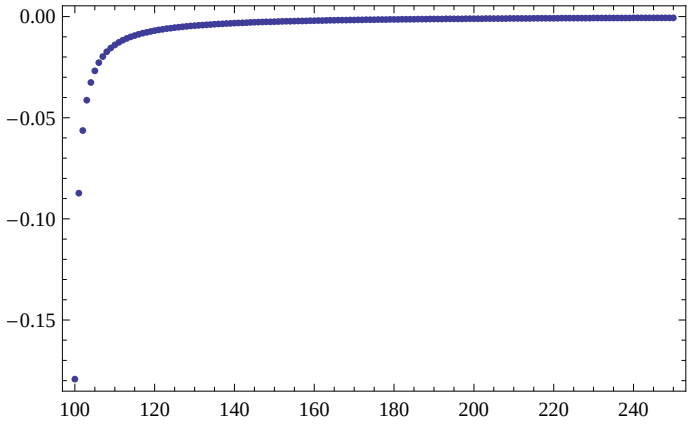

Fig. 7. The imaginary part of the eigenvalues $\lambda_{0,l}/(3N\gamma/(2s^2))$ for l from 101 to 250,where $s = 99.75 * \pi$.

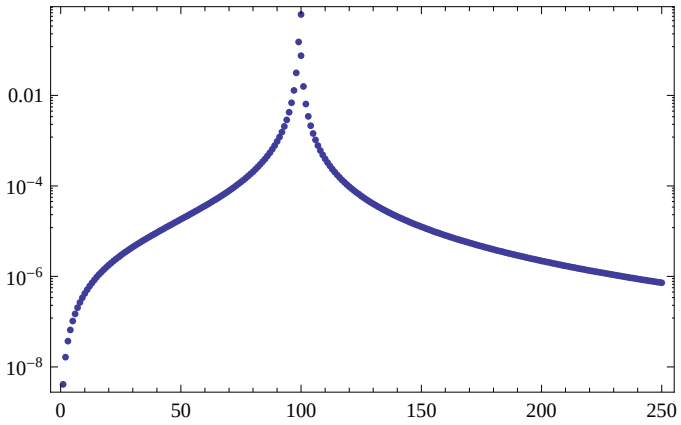

Fig. 8. The real part of the eigenvalues $\lambda_{0,l}/(3N\gamma/(2s^2))$ for l from 1 to 250, where $s = 99.75 * \pi$.

that, for example, for $l = 1$ curve, the turning points appears around $s \sim \pi$, for $l = 2$ curve, the turning points appears around $s \sim 2\pi$.

C. Numerical Results

Figures 11-14 show real and imaginary part of λ_{nl} as a function of $k_0 R$ obtained by solving Eq. (3.33) numerically. We plot the result for $n = 0$ and $l = 0, 1, 2$ in Figs. 11 and 12, while Figs. 13 and 14 show the answer for $n = 1$.

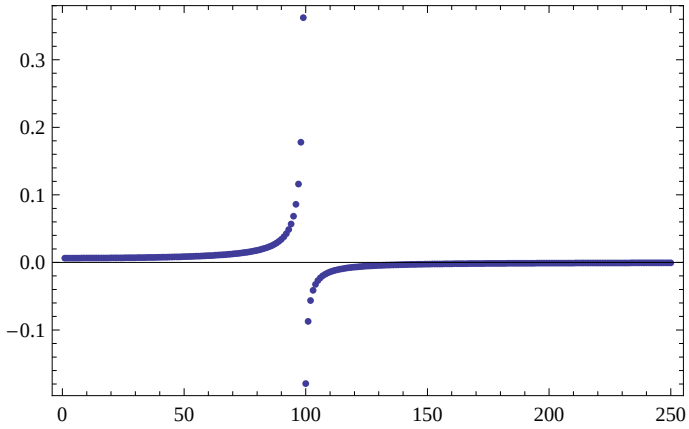

Fig. 9. The imaginary part of the eigenvalues $\lambda_{0,l}/(3N\gamma/(2s^2))$ for l from 1 to 250,where $s = 99.75 * \pi$.

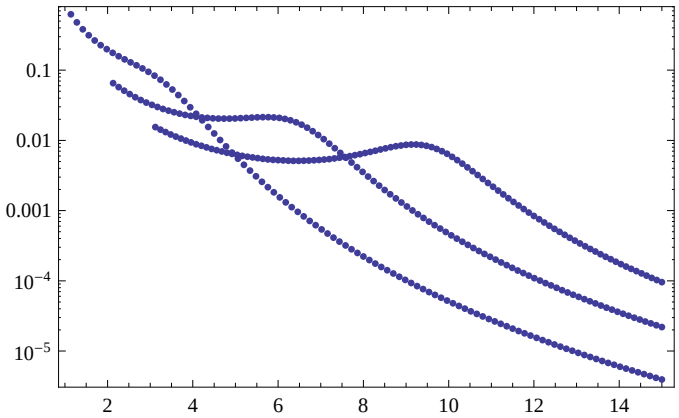

Fig. 10. The real part of the eigenvalues $\lambda_{0,l}/(3N\gamma)$ for l =1, 2, 3, where $s = 99.75 * \pi$.

D. Fermi's Golden Rules and Cooperative Radiation

In this section, we want to point out that, Fermi's Golden Rule does not generally adequate enough to describe cooperative decay from a multi-atom system. The simplest example of two-atom cooperative decay has been studied in many publications [67]. The golden rule does not work for even this very simple problem since Fano coupling is present. We discuss this in section 2. The golden rule does not generally describe the physics of N atom cooperative radiation but it does work in particular situation

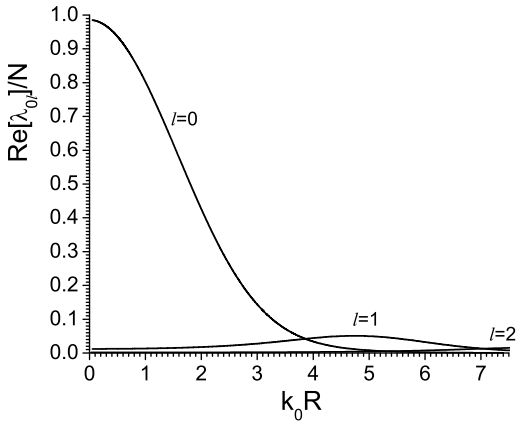

Fig. 11. Real part of λ_{0l} as a function of k_0R for $l = 0$, 1 and 2.

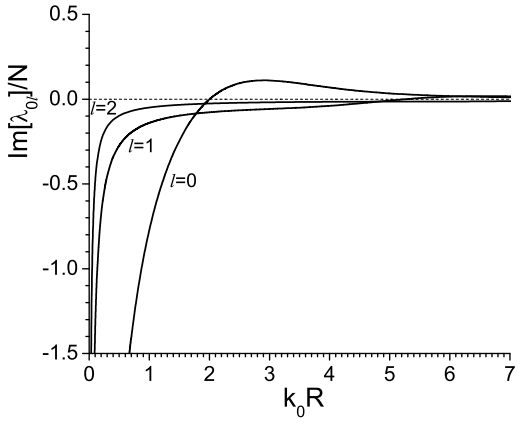

Fig. 12. Imaginary part of λ_{0l} as a function of k_0R for $l = 0$, 1 and 2.

which will be described in Section 3. In describing the decay of an initial state, it is correct to first order in perturbation theory. For the decay of a superradiant state by photon emission, first order perturbation theory describes the electromagnetic process in which the initial state makes a transition to a final state with all atoms in their ground states and an emitted photon which leaves the system without any further

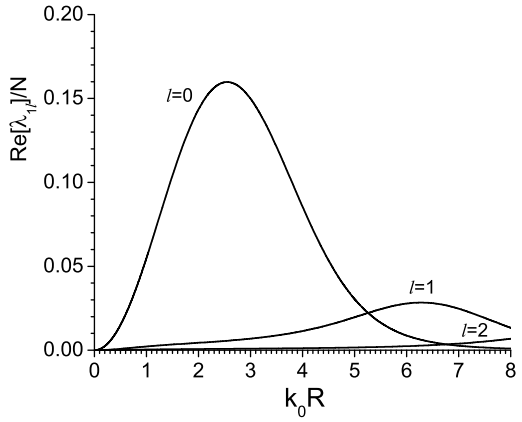

Fig. 13. Real part of λ_{1l} as a function of k_0R for $l = 0$, 1 and 2.

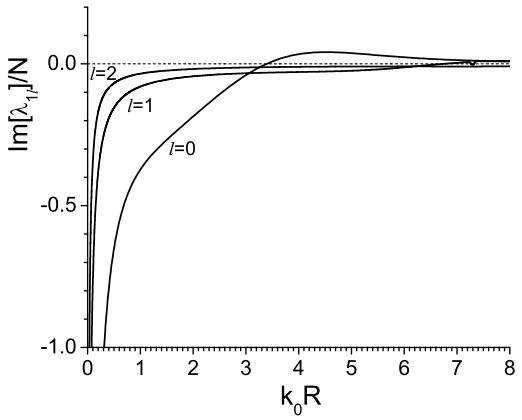

Fig. 14. Imaginary part of λ_{1l} as a function of k_0R for $l = 0$, 1 and 2.

interactions. This is clearly valid for a single atom decay. But it is not valid for a system where the photon can interact with other atom(s) before leaving the system.

1. Single Atom Decay

First we apply Fermi's golden rule to the decay of one "two-level atom", where the golden rule tells the "whole" story. Then we will consider the case of a degenerate upper level and show how such a "three-level atom" requires us to go beyond the golden rule and thus introduce the concept of Fano coupling. Here we consider a two-level (a excited and b ground) atom which is initially in the excited state and there are no photons in the field modes $|a, 0>$, $E_a - E_b = \hbar\omega$. The interaction of the atom with photons is described by the Hamiltonian $V = \sum_{\mathbf{k}} g_k \left(\hat{\sigma}\hat{a}^+_{\mathbf{k}} + \text{adj.}\right)$, where $\hat{\sigma}$ is the lowering operator for the atom, $\hat{a}_{\mathbf{k}}$ is the photon annihilation operator and g_k is the atom-photon coupling constant for the $\mathbf{k}$ mode. For the square of the matrix element between the initial state and the final state in which there is one photon with momentum $\mathbf{k}$, $|b, 1_k>$, we obtain $|<b|V|a>|^2 = g_k^2$. The Fermi's golden rule decay rate γ is then given by

$$\gamma = 2\pi \sum_{\mathbf{k}} |<b|V|a>|^2 \delta(ck - ck_0)$$

$$= \frac{8\pi^2}{c} \int dk D(k) g_k^2 \delta(k - k_0) = \frac{8\pi^2}{c} D(k_0) g_{k_0}^2, \tag{3.74}$$

where $k_0 = \omega/c$, $D(k_0) = V_{\text{ph}} k_0^2/(2\pi)^3$ is the density of photon states at $k = k_0$ and V_{ph} is the photon quantization volume. Weisskopf-Wigner theory yields the same answer for the spontaneous decay rate of a single atom.

Let us next consider the case of three-level (a_1, a_2 excited but degenerate and b ground) atom where the atom-field state vector is given by

$$|\Psi(t)\rangle = \beta_1(t)|a_1, 0\rangle + \beta_2(t)|a_2, 0\rangle + \sum_{\mathbf{k}} \gamma_{\mathbf{k}}(t)|b, 1_{\mathbf{k}}> . \tag{3.75}$$

The interaction Hamiltonian is

$$\hat{H}_{\rm int} = \sum_{\mathbf{k}} \hbar \hat{a}_k^\dagger \left[g_{k1}\hat{\sigma}_1 + g_{k2}\hat{\sigma}_2 \right] \exp[i(\nu_k - \omega)t - i\mathbf{k}\cdot\mathbf{r}] + \text{adj}\,, \tag{3.76}$$

where g_{ki} is the atom-photon coupling constant for the $\mathbf{k}$ mode and transition dipole from state a_i to b. Now we find that in Weisskopf-Wigner theory the probability amplitudes β_1 and β_2 are coupled as follows (see Appendix B in Ref. [21])

$$\dot{\beta}_1 = -\gamma_1\beta_1(t) - \sqrt{\gamma_1\gamma_2}\beta_2(t), \tag{3.77}$$

$$\dot{\beta}_2 = -\gamma_2\beta_2(t) - \sqrt{\gamma_1\gamma_2}\beta_1(t), \tag{3.78}$$

where $\gamma_i = 8\pi^2 D(k_i) g_{k_i}^2/c$. We refer to such coupling of β_1 and β_2 as "Fano coupling". Fano arrived at similar coupled equations in the context of continuum states in atoms and molecules.

Agarwal was the first to arrive at level coupling due to spontaneous emission. Clearly the physics here goes beyond the golden rule. Finally we consider the case in which $\gamma_1 = \gamma_2 = \gamma$, then the quantities $\beta_\pm = \beta_1 \pm \beta_2$ obey the equations $\dot{\beta}_+ = -2\gamma\beta_+$, $\dot{\beta}_- = 0$. The + and − combinations are the essence of the $|1,0>$ and $|0,0>$ Dicke states to which we now turn.

2. Two Atom Decay

While the golden rule explains the decay of a single two-level atom, this is not the case for a few such atoms. Let us show that the Fermi's golden rule gives the wrong answer for the decay rate of a pair of two-level atoms. We consider two atoms (a excited and b ground states) located at $\mathbf{r}_1$ and $\mathbf{r}_2$. The interaction Hamiltonian is

$$V = \sum_{\mathbf{k}} g_k \left(\left[\hat{\sigma}_1 \exp(-i\mathbf{k}\cdot\mathbf{r}_1) + \hat{\sigma}_2 \exp(-i\mathbf{k}\cdot\mathbf{r}_2) \right] \hat{a}_k^+ + \text{adj.} \right). \tag{3.79}$$

We assume that the initial atom state is an entangled state

$$|+>_{k_0}= \frac{1}{\sqrt{2}}\left[\exp(i\mathbf{k}_0\cdot\mathbf{r}_1)|a_1b_2> + \exp(i\mathbf{k}_0\cdot\mathbf{r}_2)|b_1a_2>\right] \tag{3.80}$$

in which one atom is excited, but we don't know which one. This state is prepared when a single photon with momentum $\mathbf{k}_0$ is absorbed by the atoms. Applying the Fermi's golden rule we obtain the (incorrect) decay rate

$$\Gamma = \gamma\left[1+\cos[\mathbf{k}_0\cdot\mathbf{r}_{12}]\frac{\sin(k_0r_{12})}{k_0r_{12}}\right], \tag{3.81}$$

where $\mathbf{r}_{12}=\mathbf{r}_2-\mathbf{r}_1$. Now let us treat the problem via the Weisskopf-Wigner theory. The other atomic state associated with single photon absorption is

$$|->_{k_0}= \frac{1}{\sqrt{2}}\left[\exp(i\mathbf{k}_0\cdot\mathbf{r}_1)|a_1b_2> - \exp(i\mathbf{k}_0\cdot\mathbf{r}_2)|b_1a_2>\right]. \tag{3.82}$$

The evolution of the state vector

$$|\Psi(t)\rangle = \beta_+(t)|+\rangle_{k_0} + \beta_-(t)|-\rangle_{k_0} + \sum_{\mathbf{k}}\gamma_{\mathbf{k}}(t)|b_1b_2>|1_{\mathbf{k}}>, \tag{3.83}$$

is described (see Appendix C in Ref. [21]) by the coupled equations for $\beta_+(t)$ and $\beta_-(t)$

$$\dot{\beta}_+(t) = -\gamma F_+\beta_+(t) - i\gamma F\beta_-(t), \tag{3.84}$$

$$\dot{\beta}_-(t) = -\gamma F_-\beta_-(t) + i\gamma F\beta_+(t), \tag{3.85}$$

where

$$F_\pm = 1\pm\cos(\mathbf{k}_0\cdot\mathbf{r}_{12})\frac{\sin(k_0r_{12})}{k_0r_{12}}, \quad F=\sin(\mathbf{k}_0\cdot\mathbf{r}_{12})\frac{\sin(k_0r_{12})}{k_0r_{12}}. \tag{3.86}$$

Eqs. (3.84) and (3.85) have the form obtained by Fano in which the amplitudes β_+ and β_- are coupled in the equation of motion; they yield

$$\beta_+(t) = C_1 e^{-\Gamma_+ t} + C_2 e^{-\Gamma_- t}, \tag{3.87}$$

where

$$\Gamma_\pm = \gamma \left(1 \pm \frac{\sin(k_0 r_{12})}{k_0 r_{12}}\right). \tag{3.88}$$

Eqs. (3.87) and (3.88) differ substantially from the Fermi's golden rule result (3.81). Fano coupling between $\beta_+(t)$ and $\beta_-(t)$ is the reason why the Fermi's golden rule yields an incorrect answer.

3. N-atom Decay

As what we have seen in Chapter II, for the case that $N \gg 1$, there is no Fano coupling between the $|+\rangle$ state and other $|j\rangle_{k_0}$ states. We are thus left with an equation for β_+ of the form

$$\begin{aligned}
\dot{\beta}_+(t) \;=\; & -\int dt' \sum_{\vec{k}} g_k^2 e^{-ic(k-k_0)(t-t')} \beta_+(t') + \\
& -\int dt' \sum_{\vec{k}} g_k^2 \frac{\beta_+(t')}{N} e^{-ic(k-k_0)(t-t')} \Big\{ e^{i(\vec{k}-\vec{k}_0)\cdot\vec{r}_1} [\underbrace{0}_1 + e^{i(\vec{k}-\vec{k}_0)\cdot\vec{r}_2} + ... \\
& + e^{i(\vec{k}-\vec{k}_0)\cdot\vec{r}_N}] + e^{i(\vec{k}-\vec{k}_0)\cdot\vec{r}_2} \left[e^{i(\vec{k}-\vec{k}_0)\cdot\vec{r}_1} + \underbrace{0}_2 + ... + e^{i(\vec{k}-\vec{k}_0)\cdot\vec{r}_N} \right] + ... \\
& + e^{i(\vec{k}-\vec{k}_0)\cdot\vec{r}_N} \left[e^{i(\vec{k}-\vec{k}_0)\cdot\vec{r}_1} + e^{i(\vec{k}-\vec{k}_0)\cdot\vec{r}_2} + ... + \underbrace{0}_N \right] \Big\},
\end{aligned} \tag{3.89}$$

where we have then $k_a = k_0$ and have separated off the terms of the same atomic index. The notation $\underbrace{0}_i$ means to remind us that these terms have been removed and now are contained in the first integral of (E5). Next we note that each of the square bracketed terms in (E5) yield a delta function, e.g.,

$$\left[\underbrace{0}_1 + e^{i(\vec{k}-\vec{k}_0)\cdot\vec{r}_2} + ... + e^{i(\vec{k}-\vec{k}_0)\cdot\vec{r}_N}\right] = (2\pi)^3 \frac{N-1}{V} \delta(\vec{k}-\vec{k}_0). \tag{3.90}$$

We may back transform and write the delta function in terms of the magnitude of k and solid angle unit vectors $\hat{\Omega}_k$, etc., as

$$\begin{aligned}\delta(\vec{k}-\vec{k}_0) &= \delta(k-k_0)\delta(\hat{\Omega}_k-\hat{\Omega}_{k_0})/k^2 \\ &\cong (2\pi)^3\left[\frac{1}{2\pi}\int_{-R}^{R} e^{i(k-k_0)r}dr\right]\frac{\delta(\hat{\Omega}_k-\hat{\Omega}_{k_0})}{k^2},\end{aligned} \tag{3.91}$$

where R is the radius of the atomic cloud, which is taken to be large enough so that the integral approximates $\delta(k-k_0)$. Thus (3.89) now reads

$$\begin{aligned}\dot{\beta}_+(t) &= -\int dt' \sum_{\vec{k}} g_k^2 e^{-ic(k-k_0)(t-t')}\beta_+(t') \\ &\quad -\int dt' \sum_{\vec{k}} g_k^2 e^{-ic(k-k_0)(t-t')}\left(\frac{(N-1)(2\pi)^2}{Vk^2}\right)\int_{-R}^{R} dr e^{i(k-k_0)r}\delta(\hat{\Omega}_k-\hat{\Omega}_{k_0})\beta_+(t').\end{aligned} \tag{3.92}$$

We noticed that, only at the limiting case that N is large enough that $\sum_j e^{i(\mathbf{k}-\mathbf{k}_0)\cdot\mathbf{r}_j}$ $\Rightarrow \delta(\mathbf{k}-\mathbf{k}_0)$, the factors multiplying all of the states $\beta_1, ...\beta_{N-1}$ in Eq. (2.34) vanish. We are thus left with an equation for $\beta_+(t)$ without Fano cross terms and the Fermi's golden rule can give us the right answer. However, this is not the case for general N atoms problem. Even in the large number N limit, Fano coupling does not vanish for the states $|m\rangle_{k_0}$. Thus the golden rule does not describe their time evolution.

Finally, we would like to point out that the situation is much more complicated in the case of a superradiant nuclear excited state emitting a photon which then goes through a thick crystal. One then has to take into account the energy spectrum of the photon wave which is broader than the natural line width of the resonance of a single nucleus. The energy spectrum of the wave changes as it passes through a crystal which has a very complicated energy-dependent index of refraction. We do not discuss this case in the present paper.

During photon emission some energy is transferred to atomic kinetic energy (re-

coil energy). For optical photons the recoil energy of an atom $R = (\hbar\omega)^2/2Mc^2$, where M is the atom mass, is of the order of $10^4 s^{-1}$. This value is much smaller then γ and hence recoil effect can be disregarded. However, for $X-$rays this is not necessarily the case. One can avoid recoil effect by placing atoms in a crystal lattice. The probability that an atom can recoil elastically without transferring energy to the lattice vibrations is given by the Debye-Waller factor which in a simple approximation is equal to $\exp(-R/E_D)$, where E_D is the Debye energy. The Debye energy is of the order of 0.01 eV. For photons with energy much smaller then 10 keV the Debye-Waller factor is very close to one that is the entire crystal acts as the recoiling body. For such photons one can neglect the recoil effect by placing atoms in a crystal lattice.

CHAPTER IV

APPLICATION OF COOPERATIVE EFFECT ON ATOM MICROSCOPY *

In this chapter, we discuss the application of the cooperative effect in atom microscopy. We studied the property of two-atom resonant fluorescence driven by standing wave laser. It turns out that the resonant fluorescence spectrum and intensity-intensity correlation function reveal the distance information between these two atoms. Based on that, we propose novel schemes to measure the inter-atomic distance which is smaller than half the wavelength of the illuminating light.

The outline of this chapter is the following: In section A, we first give a short introduction about the problem of inter-atom distance measurement beyond the diffraction limit; in section B, we then introduce the atom localization inside a standing wave field which was the key motivation of this work; in section C, we describe the system and derive expressions for the first and second order correlation functions, which give us the necessary tools to calculate the resonant fluorescence spectrum and intensity-intensity correlation function spectrum; in section D we calculate the fluorescence spectrum numerically and find different behavior in three regions. We discuss the corresponding measurement scheme as well; in section E we discuss the intensity-intensity spectrum and the method to read out distance information from that; finally, in section F, we discuss the limitation of this method and the detection geometry issue.

---

* Reprinted with permission from Jun-Tao Chang, Joerg Evers, and M. Suhail Zubairy, Phys. Rev. A, 74, 043820 (2006) and Jun-Tao Chang, Joerg Evers, Marlan O. Scully, and M. Suhail Zubairy, Phys. Rev. A, 73, 031803 (R) (2006). Copyright (2006) by the American Physical Society.

A. Far-feld Optical Microscopy and Diffraction Limit

The measurement of small distances is an important problem with applications to for example nano- and bioscience [70]. For many atomic and molecular systems, this goes to the search for schemes which allow us to locate one or two atoms or molecules as precisely as possible, frequently with the help of optical methods [44, 71, 72, 73, 74, 75, 76, 77, 78, 79, 80, 47]. Classically, the spatial resolution of optical devices is limited (by diffraction) to about $\lambda/2$, where λ is the optical wavelength, which is also called Rayleigh limit.

Recently, however, several schemes have been proposed which allow us to localize single atoms with sub-wavelength precision and to beat the classical limit. The general idea here is to encode the position information in observables which do not suffer from the diffraction limit [71, 72, 73, 74, 75, 76, 77, 78, 79]. Frequently, these studies have focused on single particles, where the position is the only spatial degree of freedom. Other techniques have been proposed for few-particle systems with non-identical constituents. For example, the transition frequencies of the respective atoms could be different, and the particles can be addressed individually regardless of their separation [80]. This idea has been verified experimentally in [47], where also the modification of optical spectra due to dipole couplings in the small-distance limit has been observed. In another approach, probing of two identical particles has been studied [44], together with related advances in microscopy and lithography [43].

In this work, we proposal a new method by measuring the spectrum or intensity-intensity correlation function power spectrum of the emitted fluorescence by two adjacent atoms locating inside a standing wave field, which can cover the full range beyond diffraction limit from half wavelength down to sub nanometer region.

B. Atom Localization via Resonant Fluorescence

The motivation of this work comes from atom localization, an subject which has been studied theoretically and experimentally for many years.

Storey et al. and Marte and Zoller [72] proposed the idea to localize an atom by measuring the phase shift of the optical field in a cavity due to the spatially varying atom-field coupling. A related technique for the position measurement of the atom is used by Kunze et al. [75] in which the phase shift of the atomic dipole, rather than the light field is used. Kien et al. [76] further investigated this method and showed that a coherent cavity field substantially enhances the resolution as compared to a classical field. Thomas and co-workers [74] proposed and demonstrated a method called "atom imaging" based on resonance imaging, i.e., a spatially varying potential shifts the resonance frequency of an atomic transition, to localize the atom, since the resonance frequency is position dependent and position distribution is determined by spectroscopic methods. They further demonstrated that a suboptical wavelength localization can be achieved by using light-shift gradient for atom imaging [71].

Zubairy et al. [79] suggested a simple scheme to localize an atom inside the standing wave during its motion. The general idea is that the frequency of the spontaneously emitted photon carries the information about the position of the atom due to its dependence on the position dependent Rabi frequency of the driving field. In the presence of the standing wave driving field, dynamic Stark splitting of the atomic levels takes place and we get a three-peak resonance fluorescence spectrum. The splitting is directly proportional to the position-dependent Rabi frequency. Therefore an atom is localized as soon as the spontaneously emitted photon is detected.

The system considered in their work is shown in Fig. 15. One two-level atom A with energy levels $|a\rangle$ and $|b\rangle$ and transition frequency ω_{ab} that is moving along

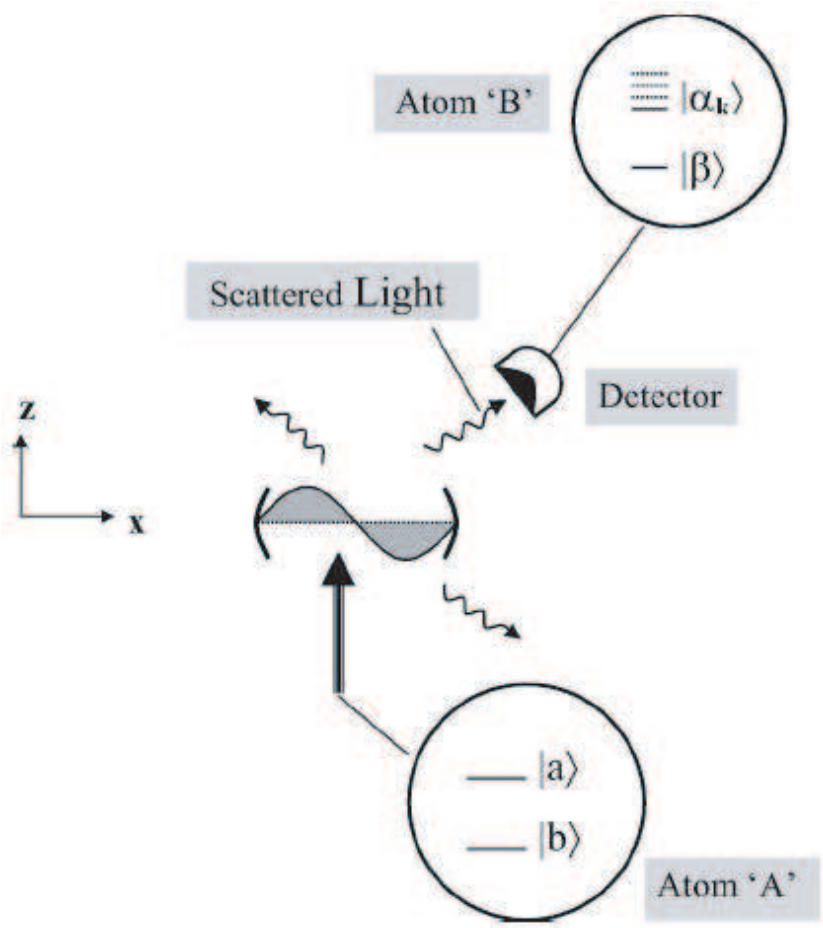

Fig. 15. Two-level atom A moving along the z axis and interacting with a resonant standing-wave light field of wave vector $\mathbf{k}$ aligned along the x axis. The driven atom A radiates spontaneously in all directions. The detector atom B, consisting of the ground level $|b\rangle$and a set of excited levels $\alpha_{\mathbf{k}}$, absorbs the emitted photon in mode $\mathbf{k}$ [79].

the z axis and interacts with a resonant standing-wave light field of wave vector $\mathbf{k}$ aligned along the x direction as shown in Fig. 15. The velocity component of the atom along the z axis is considered large enough so that the motion in this direction is treated classically. The driven atom radiates spontaneously and one of the modes of the scattered light interacts with the detector atom B, initially in its ground state. They assume that the center-of-mass momentum of the atom A along x axis does

not change appreciably during its passage through the standing wave. Then, by measuring the resonance fluorescence spectrum, they get three peaks centered at $\Delta = 0$ and $\Delta = \pm\Omega$, where Ω are the corresponding Rabi frequency. Since the Rabi frequency Ω is position-dependent $\Omega_0 \sin(kx)$, the atom now undergoes a different Rabi oscillation at a different position in a standing wave and from the measured spectrum they obtained atomic position distribution with sub-wavelength resolution (See Fig. 16).

Motivated by this work, a straightforward idea is that if we place two identical atoms inside one wavelength region but at different locations, then each of them will experience different Rabi oscillations which corresponds to $\Omega_i \sim \Omega_0 \sin kx_i$. According to the resonant fluorescence theory, the radiation field of each of them will have their own set of Mollow peaks, with the central one corresponding to $\Delta = 0$ and the side bands corresponding to $\Delta = \pm\Omega_i$. However, the detector in the far field will not be able to tell from which atoms the light come, so the spectrum actually measured by the detector will have five peaks, with the central peak at $\Delta = 0$ and the inner sidebands corresponding to $\min\{\Omega_1, \Omega_2\}$ and the outer sidebands corresponding to $\max\{\Omega_1, \Omega_2\}$. This is as illustrated in Fig. 17. Naturally, people would imagine that, after obtaining the radiation field spectrum like Fig. 17. We will be able to trace back to the location information/distance information of these two atoms using the inverse function of $\sin kx$. And obviously it is beyond the diffraction limit $\lambda/2$.

However, detailed investigation shows that cooperative effect plays an important role, since we are talking about the sub-wavelength separations between atoms. In the following, we investigate the system dynamics using master equation approach [53] including the cooperative effect. We then propose and analyze in detail the measurement procedure.

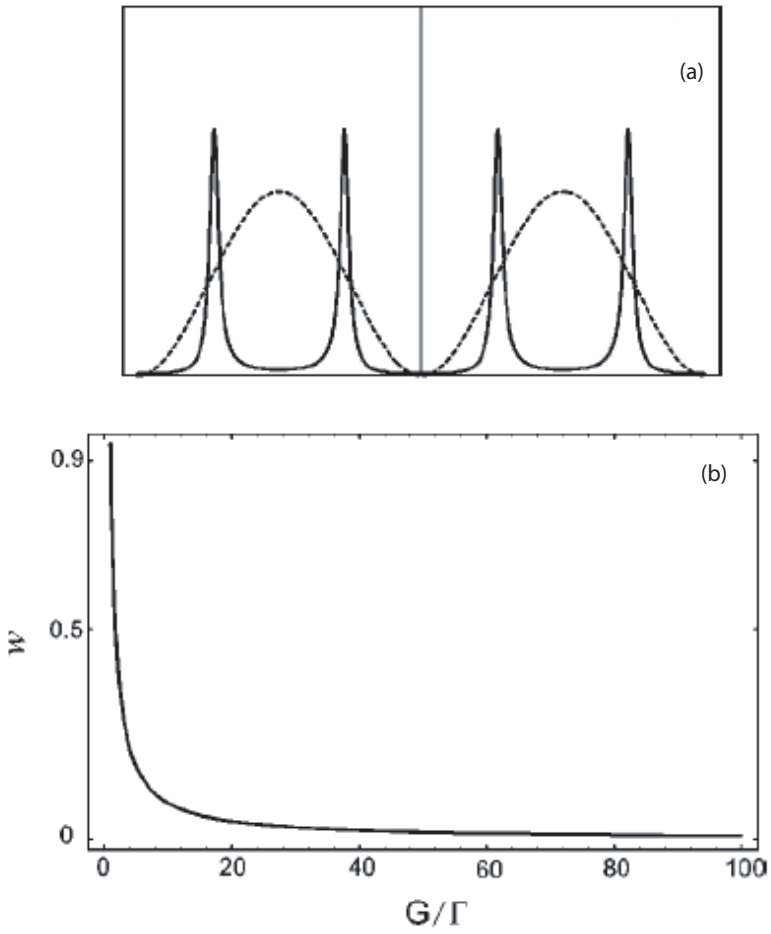

Fig. 16. (a) Conditional position distribution regarding to the position kx, where the doted line corresponds to the standing wave. Here the position information is available in the subwavelength domain of the standing-light field. (b)Plot of the width of the best resolved peaks versus Rabi frequency at the anti-node. This plot shows a strong dependence of width on the amplitude of the position-dependent Rabi frequency. [79]

C. Master Equation of the System

Our model system consists of two identical two-level atoms, with transition frequencies ω_0, a dipole transition moment μ and the decay rate γ. The atoms are assumed to be located at position $\mathbf{r}_i = (x_i, y_i, z_i)^T$ in a linearly polarized near-resonant standing

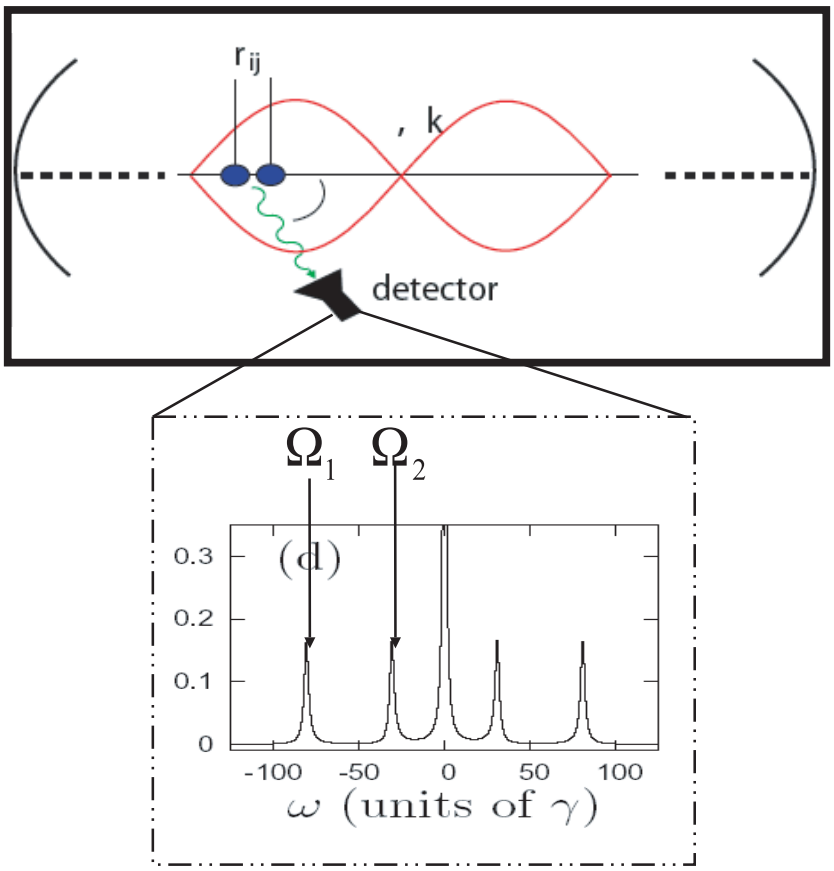

Fig. 17. Idealized resonant fluorescence spectrum for two atoms siting inside a standing wave laser field.

wave laser field (see Fig. 18 (a)). The distance between them is $r_{ij} = |\mathbf{r}_{ij}|$ with $\mathbf{r}_{ij} = \mathbf{r}_i - \mathbf{r}_j$. Further, they are coupled to all the other modes of the electromagnetic field, which are assumed to be in their vacuum state initially.

In the laboratory frame and under the rotating-wave approximation, the system evolution is described by the reduced atomic density operator ρ, which obeys the following master equation [81]

$$\frac{\partial \rho}{\partial t} = \frac{1}{i\hbar}[H, \rho] - \sum_{i,j=1}^{2} \gamma_{ij} \left([S_i^+, S_j^- \rho] - [S_j^-, \rho S_i^+] \right) . \tag{4.1}$$

Here S_i^+ and S_i^- are the atomic raising and lowing operators that raise and lower the

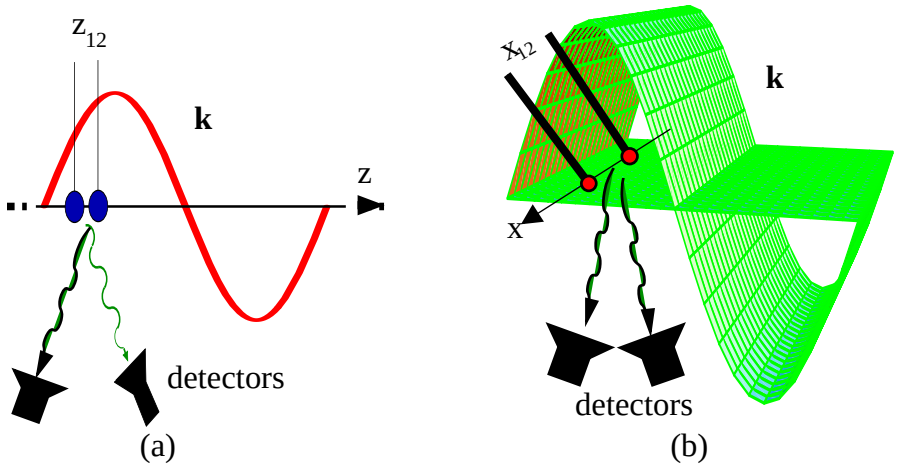

Fig. 18. Two atoms in a standing wave field with a distance r_{ij} smaller than half the the wavelength $\lambda/2$ of the driving field. Two geometries are considered in this paper: The driving field propagation direction is either (a) parallel or (b) perpendicular to the interatomic distance vector $\mathbf{r}_{12}$.

state of atom i ($i = 1, 2$). These operators satisfy the following relations ($i \neq j$),

$$(S_i^{\pm})^2 = 0\,, \quad S_i^{\pm} S_j^{\pm} = S_j^{\pm} S_i^{\pm}\,, \quad S_i^{\pm} S_j^{\mp} = S_j^{\mp} S_i^{\pm}\,. \tag{4.2}$$

The system Hamiltonian is given by $H = H_0 + H_{dd} + H_L$, where

$$H_0 = \frac{\hbar}{2}\omega_0 \sum_{i=1}^{2} (S_i^+ S_i^- - S_i^- S_i^+)\,, \tag{4.3}$$

$$H_{dd} = \hbar\Omega_{12}(S_1^+ S_2^- + S_2^+ S_1^-)\,, \tag{4.4}$$

$$H_L = \frac{\hbar}{2} \sum_{i=1}^{2} \left(\Omega_i S_i^+ e^{-i\omega_L t} + \text{H.c.}\right)\,, \tag{4.5}$$

are the free energy, the dipole-dipole interaction, and the interaction with the driving laser field, respectively. In the above equations, ω_L is the frequency of the driving field and $\mathbf{k} = k\hat{\mathbf{k}}$ is its wave vector, which is along the z axis of our coordinate frame. Ω_i is the driving field Rabi frequency of atom i ($i = 1, 2$). The parameter γ_{ij} is given

by

$$\gamma_{ij} = \frac{3}{2}\gamma \left[\frac{\sin(kr_{ij})}{(kr_{ij})} + \frac{\cos(kr_{ij})}{(kr_{ij})^2} - \frac{\sin(kr_{ij})}{(kr_{ij})^3} \right] , \tag{4.6}$$

and contains both the usual spontaneous emission rates γ of the two individual atoms ($i = j$) and collective cross-damping terms ($i \neq j$). The dipole-dipole interaction potential Ω_{12} is given by

$$\Omega_{12} = \frac{3}{2}\gamma \left[-\frac{\cos(kr_{ij})}{(kr_{ij})} + \frac{\sin(kr_{ij})}{(kr_{ij})^2} + \frac{\cos(kr_{ij})}{(kr_{ij})^3} \right] . \tag{4.7}$$

Both the terms proportional to Ω_{12} and γ_{12} in the master equation, Eq. (4.1), arise from the interaction of the atoms via the empty modes of the quantized radiation field [32]. From Eqs. (4.6) and (4.7), we can see that these two dipole-dipole interaction terms can crucially influence the system dynamics if the two atoms are very close to each other. For small interatomic distances ($kr_{ij} \ll 1$), Eq. (4.6) and (4.7) may be simplified to

$$\Omega_{12} \approx \frac{3\gamma}{2(kr_{ij})^3} , \qquad \gamma_{ij} \approx \gamma . \tag{4.8}$$

For large distances ($kr_{ij} \gg 1$), $\Omega_{12} \approx 0$ and $\gamma_{ij} \approx \gamma\delta_{ij}$, where δ_{ij} is the Kronecker Delta symbol.

Supposing that the laser propagation direction is along the interatomic distance vector, and that the position of the first atom relative to a standing wave field node is z_1, then the two Rabi frequencies are given by

$$\Omega_1 = \Omega \sin(kz_1) , \qquad \Omega_2 = \Omega \sin(kz_{12} + kz_1) , \tag{4.9}$$

where, $z_{12} = r_{12}$. Further, we suppose that the transition dipole moments of the two atoms are parallel to each other and are aligned perpendicular to the distance vector of the two atoms $\mathbf{r}_{12}$, e.g., by means of a weak external field. Note that in

other geometries, further contributions to the Master equation may arise [84]. The geometry of the system is illustrated in Fig. 18(a).

The two-time intensity-intensity correlation function of the light field detected at point $\mathbf{R}_1$ at time t_1 and at a point $\mathbf{R}_2$ at time t_2 is defined as [51]:

$$G^{(2)}(\mathbf{R}_1, t_1; \mathbf{R}_2, t_2) = \langle E^{(-)}(\mathbf{R}_1, t_1) E^{(-)}(\mathbf{R}_2, t_2) E^{(+)}(\mathbf{R}_2, t_2) E^{(+)}(\mathbf{R}_1, t_1) \rangle \,. \quad (4.10)$$

Here, $E^{(\pm)}$ are the negative and positive frequency parts of the electric field operator. The normalized intensity-intensity correlation function is defined as

$$g^{(2)}(\mathbf{R}_1, t_1; \mathbf{R}_2, t_2) = \frac{G^{(2)}(\mathbf{R_1}, t_1; \mathbf{R}_2, t_2)}{G^{(1)}(\mathbf{R}_1, t_1) G^{(1)}(\mathbf{R}_2, t_2)} \,, \quad (4.11)$$

where

$$G^{(1)}(\mathbf{R}_i, t_i) = \langle E^{(-)}(\mathbf{R}_i, t_i) E^{(+)}(\mathbf{R}_i, t_i) \rangle \quad (4.12)$$

is the first-order correlation function of the field detected at a point $\mathbf{R}_i$ at time t_i ($i = 1, 2$), i.e. the field intensity. The correlation function $G^{(2)}(\mathbf{R}_1, t_1; \mathbf{R}_2, t_2)$ is proportional to the joint probability of finding one photon at $\mathbf{R}_1$ at time t_1 and another photon at $\mathbf{R}_2$ at time t_2, and yields information about photon statistics of the emitted light.

Following the approach in [51], these two kinds of correlation functions can be written in terms of the expectation values of the atomic transition operators as follows:

$$G^{(1)}(\mathbf{R}, t) = U(\mathbf{R}) \sum_{i,j=1}^{2} \langle S_i^+(t') S_j^-(t') \rangle \, \exp(\imath k \hat{\mathbf{R}} \cdot \mathbf{r}_{ij}) \,, \quad (4.13)$$

$$\begin{aligned} G^{(2)}(\mathbf{R}_1, t_1; \mathbf{R}_2, t_2) \;&=\; U(\mathbf{R}_1) U(\mathbf{R}_2) \times \sum_{i,j,k,l=1}^{2} \langle S_i^+(t_1^{(i)}) S_j^+(t_2^{(j)}) S_k^-(t_2^{(k)}) S_l^-(t_1^{(l)}) \rangle \times \\ &\qquad \exp[\imath k (\hat{\mathbf{R}}_1 \cdot \mathbf{r}_{il} + \hat{\mathbf{R}}_2 \cdot \mathbf{r}_{jk})] \,, \end{aligned} \quad (4.14)$$

where $t' = t - R/c$, $t_i^{(\alpha)} = t_i - R_\alpha/c$, and $U(\mathbf{R}_i) = \omega_0^4 \mu^2 \sin^2\theta/(2\mathbf{R}_i^2 \pi\varepsilon_0)$ $(i, \alpha = 1, 2)$. Here, θ is the angle between the observation direction and the atomic dipole moment μ. Note that we do not include retardation effects, since it has been shown that retardation effects play a significant role in the resonant interaction of two identical atoms only if the interatomic distance is larger than the resonant wavelength [82].

Thus, the normalized intensity-intensity correlation function of the steady state can be written as

$$\begin{aligned} g^{(2)}(\mathbf{R}_1, \mathbf{R}_2; \tau) = & \lim_{t_1 \to \infty} g^{(2)}(\mathbf{R}_1, t_1; \mathbf{R}_2; t_1 + \tau) \\ = & \lim_{t_1 \to \infty} \frac{G^{(2)}(\mathbf{R}_1, t_1; \mathbf{R}_2, t_1 + \tau)}{G^{(1)}(\mathbf{R}_1, t_1) \cdot G^{(1)}(\mathbf{R}_2, t_1 + \tau)} \,. \end{aligned} \tag{4.15}$$

In our geometry, under far-field approximation, we have

$$R_1 = R_2 \,, \tag{4.16}$$

$$t_1^{(1)} = t_1^{(2)} = t_1' \,, \tag{4.17}$$

$$t_2^{(1)} = t_2^{(2)} = t_2' \,. \tag{4.18}$$

Therefore the intensity-intensity correlation function can be simplified to give

$$\begin{aligned} g^{(2)}(\mathbf{R}_1, \mathbf{R}_2; \tau) = & \lim_{t_1' \to \infty} \sum_{i,j,k,l=1}^{2} e^{\imath k(\hat{\mathbf{R}}_1 \cdot \mathbf{r}_{il} + \hat{\mathbf{R}}_2 \cdot \mathbf{r}_{jk})} \\ & \times \frac{\langle S_i^+(t_1') S_j^+(t_1' + \tau) S_k^-(t_1' + \tau) S_l^-(t_1') \rangle}{\left[\sum_{m,n=1}^{2} \langle S_m^+(t_1') S_n^-(t_1') \rangle \exp(\imath k \hat{\mathbf{R}} \cdot \mathbf{r}_{mn}) \right]^2} \,. \end{aligned} \tag{4.19}$$

Thus, we have expressed the correlation function of the electromagnetic field in terms of the correlation function of atomic operators. It is well known that the expectation value of an atomic operator Q can be written as

$$\langle Q \rangle = Tr_s(\rho Q) \,, \tag{4.20}$$

where the trace involves only atomic and laser field degrees of freedom. Substituting $S_i^{\pm}$ $(i = 1, 2)$ into Eq. (4.20) and using the master Eq. (4.1), we can get a closed set of fifteen first-order differential equations describing the evolution of the atomic variables. In a matrix notation, this set of equations can be rewritten as a inhomogeneous equation:

$$\dot{\mathbf{X}}(t) = \mathbf{M}\mathbf{X}(t) + \mathbf{I}\,, \tag{4.21}$$

where the dot indicates differentiation with respect to γt. $\mathbf{X}(t)$ is the column vector with elements

$$X_1 = \langle \tilde{S}_1^+ \rangle\,, \qquad X_2 = \langle \tilde{S}_1^- \rangle\,, \tag{4.22a}$$

$$X_3 = \langle \tilde{S}_2^+ \rangle\,, \qquad X_4 = \langle \tilde{S}_2^- \rangle\,, \tag{4.22b}$$

$$X_5 = \langle \tilde{S}_1^+ \tilde{S}_1^- \rangle\,, \qquad X_6 = \langle \tilde{S}_2^+ \tilde{S}_2^- \rangle\,, \tag{4.22c}$$

$$X_7 = \langle \tilde{S}_1^+ \tilde{S}_2^- \rangle\,, \qquad X_8 = \langle \tilde{S}_2^+ \tilde{S}_1^- \rangle\,, \tag{4.22d}$$

$$X_9 = \langle \tilde{S}_1^+(t) \tilde{S}_2^+ \rangle\,, \qquad X_{10} = \langle \tilde{S}_1^- \tilde{S}_2^- \rangle\,, \tag{4.22e}$$

$$X_{11} = \langle \tilde{S}_1^+ \tilde{S}_1^- \tilde{S}_2^- \rangle\,, \qquad X_{12} = \langle \tilde{S}_1^+ \tilde{S}_2^+ \tilde{S}_1^- \rangle\,, \tag{4.22f}$$

$$X_{13} = \langle \tilde{S}_2^+ \tilde{S}_1^- \tilde{S}_2^- \rangle\,, \qquad X_{14} = \langle \tilde{S}_1^+ \tilde{S}_2^+ \tilde{S}_2^- \rangle\,, \tag{4.22g}$$

$$X_{15} = \langle \tilde{S}_1^+ \tilde{S}_2^+ \tilde{S}_1^- \tilde{S}_2^- \rangle\,. \tag{4.22h}$$

The operators in Eq. (4.22) are defined as

$$\tilde{S}_i^{\pm}(t) = S_i^{\pm} \exp(\mp \imath \omega_L t)\,. \tag{4.23}$$

$\mathbf{M}$ is a 15×15 matrix containing the coefficients of the differential equations, and $\mathbf{I}$ is a constant column vector. The non-vanishing elements of matrix $\mathbf{M}$ and vector $\mathbf{I}$

are given in Appendix B. The dimensionless parameters are defined as

$$\beta = \frac{\Omega_1}{\gamma}\,, \qquad \beta_2 = \frac{\Omega_2}{\gamma}\,, \qquad a = \frac{\gamma_{12}}{\gamma}\,, \tag{4.24a}$$

$$b = \frac{\Omega_{12}}{\gamma}\,, \qquad \Delta = \frac{(\omega_L - \omega_0)}{\gamma}\,. \tag{4.24b}$$

For non-zero determinant of the matrix $\mathbf{M}$, the steady state solution of Eq. (4.21) is given by

$$\mathbf{X}(\infty) = -\mathbf{M}^{-1}\mathbf{I}\,. \tag{4.25}$$

Then the matrix $\mathbf{M}$ can be diagonalized by a complex invertible matrix $\mathbf{T}$. Let $\mathbf{q} = \mathbf{T}^{-1}\mathbf{M}\mathbf{T}$, $\mathbf{Y} = \mathbf{T}^{-1}\mathbf{X}$ and $\mathbf{W} = \mathbf{T}^{-1}\mathbf{I}$, then the solution of Eq. (4.21) can be rewritten as

$$Y_i(\tau) = \lim_{t\to\infty}[Y_i(t)]\exp(\mathbf{q}_{ii}\tau) - (\mathbf{q}^{-1})_{ii}[1 - \exp(\mathbf{q}_{ii}\tau)]W_i\,. \tag{4.26}$$

In order to calculate the two-time correlation function, we also need to make use of the quantum regression theorem [51]. It states that for some operator $\hat{O}$, if the time evolution of one-time expectation values can be written as

$$\langle\hat{O}(t+\tau)\rangle = \sum_j a_j(\tau)\langle\hat{O}_j(t)\rangle\,, \tag{4.27}$$

then two-time expectation values can be expressed as

$$\langle\hat{O}_i(t)\hat{O}(t+\tau)\hat{O}_k(t)\rangle = \sum_j a_j(\tau)\langle\hat{O}_i(t)\hat{O}_j(t)\hat{O}_k(t)\rangle\,. \tag{4.28}$$

With this preparatory knowledge, we can express the steady state of the first and second order correlation functions of the radiation field as follows:

$$G^{(1)}(\mathbf{R},t)^{SS} = X_\alpha + X_\beta\cos(k\hat{\mathbf{R}}\cdot\mathbf{r}_{12}) + \imath X_\gamma\sin(k\hat{\mathbf{R}}\cdot\mathbf{r}_{12})\,, \tag{4.29}$$

and

$$G^{(2)}(\mathbf{R}_1,\mathbf{R}_2,\tau)^{SS} = \Big[X_\alpha + X_\beta\cos(k\hat{\mathbf{R}}_1\cdot\mathbf{r}_{12}) + \imath X_\gamma\sin(k\hat{\mathbf{R}}_1\cdot\mathbf{r}_{12})\Big]\cdot\Big[X_\alpha + X_\beta\cos(k\hat{\mathbf{R}}_2\cdot\mathbf{r}_{12}) + \imath X_\gamma\sin(k\hat{\mathbf{R}}_2\cdot\mathbf{r}_{12})\Big] + \sum_{j=1}^{15} P_j\cdot e^{\mathbf{q}_{jj}\cdot\tau}\,. \tag{4.30}$$

Here, $X_\alpha = X_5(\infty)+X_6(\infty)$, $X_\beta = X_7(\infty)+X_8(\infty)$, and $X_\gamma = X_7(\infty)-X_8(\infty)$; an upper index "SS" indicates steady state results. Further

$$\begin{aligned} P_j = \Big[&A_j + B_j + (C_j+D_j)\cdot\cos(k\hat{\mathbf{R}}_1\cdot\mathbf{r}_{12}) \\ &+\imath(C_j-D_j)\cdot\sin(k\hat{\mathbf{R}}_1\cdot\mathbf{r}_{12})\Big] \\ \times\Big[&(T_{5j}+T_{6j}) + (T_{7j}+T_{8j})\cdot\cos(k\hat{\mathbf{R}}_1\cdot\mathbf{r}_{12}) \\ &+\imath(T_{7j}-T_{8j})\cdot\sin(k\hat{\mathbf{R}}_1\cdot\mathbf{r}_{12})\Big]\,, \end{aligned} \tag{4.31}$$

where

$$\begin{aligned} A_j =&(T^{-1})_{j3}X_{12}(\infty) + (T^{-1})_{j4}X_{11}(\infty) \\ &+ (T^{-1})_{j6}X_{15}(\infty) + (\mathbf{q}^{-1})_{jj}W_jX_5(\infty)\,, \end{aligned} \tag{4.32a}$$

$$\begin{aligned} B_j =&(T^{-1})_{j1}X_{12}(\infty) + (T^{-1})_{j2}X_{13}(\infty) \\ &+ (T^{-1})_{j5}X_{15}(\infty) + (\mathbf{q}^{-1})_{jj}W_jX_6(\infty)\,, \end{aligned} \tag{4.32b}$$

$$\begin{aligned} C_j =&(T^{-1})_{j2}X_{11}(\infty) + (T^{-1})_{j3}X_{14}(\infty) \\ &+ (T^{-1})_{j8}X_{15}(\infty) + (\mathbf{q}^{-1})_{jj}W_jX_7(\infty)\,, \end{aligned} \tag{4.32c}$$

$$\begin{aligned} D_j =&(T^{-1})_{j1}X_{12}(\infty) + (T^{-1})_{j4}X_{13}(\infty) \\ &+ (T^{-1})_{j7}X_{15}(\infty) + (\mathbf{q}^{-1})_{jj}W_jX_8(\infty)\,. \end{aligned} \tag{4.32d}$$

With all these knowledge in hand, we are able to explore the properties of the spectrum and intensity-intensity correlation function for the radiation field.

D. Resonant Fluorescence Spectrum and Distance Measurement

In this section we are going discuss the spectrum of the emitted resonance fluorescence. The total steady state resonance fluorescence spectrum $S(\omega)$ emitted by the two atoms up to a geometrical factor is given by [81]

$$S(\omega) = \mathrm{Re} \int_0^\infty d\tau e^{i(\omega-\omega_L)\tau} \sum_{i,j=1}^{2} \langle S_i^+(0) S_j^-(\tau)\rangle_s \, e^{ik\hat{\mathbf{R}}\cdot\mathbf{r}_{ij}} \,,$$

where the subindex s denotes the steady state. $\hat{\mathbf{R}}$ is the unit vector in observation direction, and we define the observation angle θ as $\theta = \arccos(\hat{\mathbf{R}} \cdot \mathbf{r}_{12}/r_{12})$. In general, the resonance fluorescence spectrum of two nearby laser-driven atoms is rather complicated [81]. The spectrum, however, simplifies considerably in limiting cases, where either the driving field Rabi frequency or the dipole-dipole interaction energy dominate the system dynamics. This will be exploited in the following, where we present in detail a measurement procedure, which allows us to extract the distance of the two atoms and their positions relative to nodes of the standing wave field, both with fractional-wavelength precision.

The first step in the measurement sequence is to apply a standing wave laser field to the two-atom system, which at an anti-node of the standing wave corresponds to a Rabi frequency Ω of a few γ. Depending on the relative separation of the atoms, different spectra can be observed. If the two atoms are very close to each other (distance

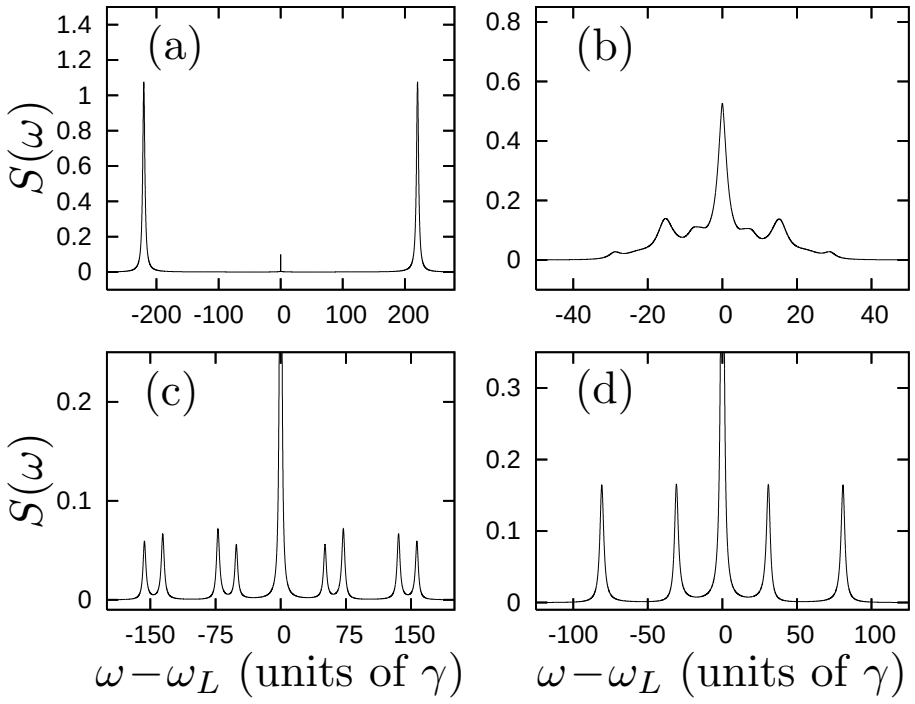

Fig. 19. Sample spectra for $\Delta = 0$, $\theta = \pi/2$, $\phi = 0.1\pi$. (a) Small separation case: $r_{12} = 0.03\lambda, \Omega = 20\gamma$ (b) Intermediate separation, weak driving field: $r_{12} = 0.08\lambda, \Omega = 20\gamma$ (c) Intermediate separation, strong driving field: $r_{12} = 0.08\lambda, \Omega = 200\gamma$ (d) Large separation case: $r_{12} = 0.6\lambda, \Omega = 100\gamma$.

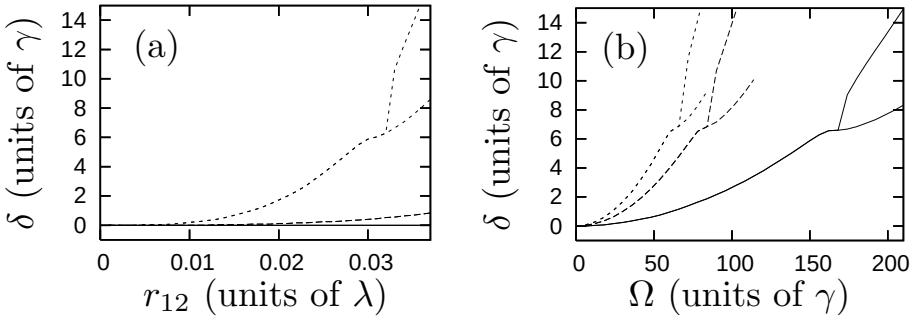

Fig. 20. Deviation $\delta = \nu_{\rm p} - \Omega_{12}$ of the peak position $\nu_{\rm p}$ from Ω_{12} for closely-spaced atoms. $\Delta = 0$, $\theta = \pi/2$, and (a) Plotted against the atomic separation. $\phi = 0.1\pi$, $\Omega = 3$ (solid), 20 (dashed), 80 (dotted). (b) Plotted against the driving field Rabi frequency. $r_{12} = 0.02\lambda$, $\phi = 0.1$ (solid), 0.25 (dashed), 0.4 (dotted). Branches correspond to splittings into two peaks.

$\leq \lambda/30$), then the spectrum is dominated by the dipole-dipole interaction energy Ω_{12}, which gives rise to sideband structures at each side of the fluorescence spectrum close to $\omega_L \pm \Omega_{12}$. A typical resonance fluorescence spectrum for this parameter range is shown in Fig. 19(a). As long as $\Omega_1, \Omega_2, \gamma \ll \Omega_{12}$ is satisfied, the sideband structures only have a small residual dependence on the Rabi frequency. Thus, the sideband peak position ν_{p} can directly be identified with Ω_{12}. Fig. 20(a) shows the deviation of the sideband peak positions from Ω_{12} versus the atomic separation distance for different Rabi frequencies Ω of the driving field. Note that the effective Rabi frequencies $\Omega_1 = \Omega \sin(\phi)$, $\Omega_2 = \Omega \sin(\mathbf{k} \cdot \mathbf{r}_{12} + \phi)$ also depend on the phase ϕ of the two atoms within the wavelength, with maximum values $\Omega_1, \Omega_2 \approx \Omega$ close to the anti-nodes. It can be seen that for weak Ω_1, Ω_2, the experimentally accessible sideband peak position and Ω_{12} coincide very well. With increasing Rabi frequency, the deviation increases, until the Rabi frequency becomes strong enough to induce a splitting of the sideband peaks, which is indicated by the branching point in Fig. 20(a). If the initial spectrum of the first measurement has insufficient signal-to-noise ratio, then the fluorescence intensity can be enhanced by increasing the driving field intensity. Note that due to the dependence of Ω_1, Ω_2 on the position of the two atoms, two experimental realizations of this measurement scheme for different positions of the two atoms may require different laser field intensities. It is also possible to extrapolate the result of several measurements to the driving field-free case in order to eliminate the effect of the driving field on the positions of the sidebands in the spectrum.

With the help of Eqs. (4.7) or (4.8), the measured Ω_{12} can easily be used to obtain the separation between the two atoms. The atomic separation is measured with increasing accuracy in the region of large slope of Ω_{12}. For maximal accuracy, Eq. (4.7) should

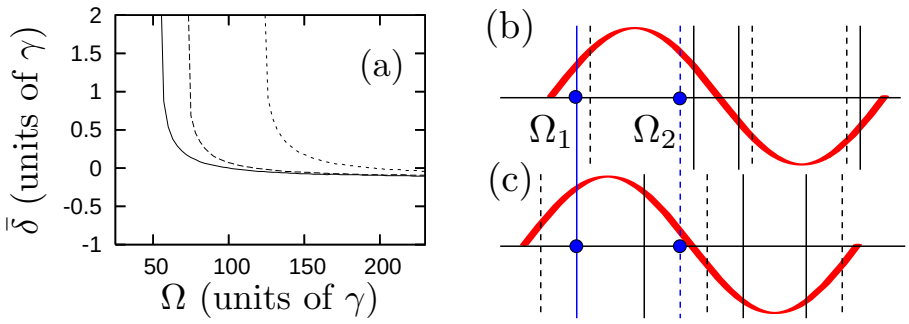

Fig. 21. (a) Deviation $\bar{\delta} = \sigma_p - 2\Omega_{12}$ of the doublet splitting σ_p from $2\Omega_{12}$ for the strong field, intermediate distance case. $r_{12} = 0.08\lambda$, $\theta = \pi/2$, and $\Delta = 0$. The positions of the atoms are $\phi = 0.1$ (solid), 0.2 (dashed), 0.3 (dotted). (b,c) Obtaining the position of the two atoms via a phase shift of the standing wave field. Solid (dashed) lines show possible atom positions for given Ω_1 (Ω_2). (b) Before, (c) after the phase shift. The only coinciding potential positions in (b) and (c) give the true atomic positions.

be numerically solved for the separation. Here, we base our discussion on the small separation limit Eq. (4.8), and allow us a small uncertainty in Ω_{12} ($\Omega_{12} \to \Omega_{12} + \delta\Omega_{12}$). We obtain

$$r_{ij} = \left(\frac{3\gamma}{2k^3\Omega_{12}}\right)^{1/3}\left(1 - \frac{\delta\Omega_{12}}{3\Omega_{12}}\right) \tag{4.33}$$

as the distance r_{ij} between the two atoms. Thus, the relative uncertainty of the final result is about 1/3 of the relative uncertainty of the measured Ω_{12}. Consider, for example, the case shown in Fig. 19(a). For the actual distance $r_{12} = 0.03\lambda$, Eq. (4.7) yields a value of $\Omega_{12} = 220.096\gamma$. From the spectrum, we obtain an experimentally accessible value of $\Omega_{12} = (220.500 \pm 22)\gamma$, where we have allowed for a relative uncertainty of the measurement of about 10%. From Eq. (4.7), the distance then evaluates to $r_{12} = (0.030 \pm 0.001)\lambda$. Thus in this case, the uncertainty of the distance measurement is about $\lambda/1000$, i.e., less than 4% of the actual distance. The possibility of matching dipole-dipole splitting energies with interatomic distances was verified

experimentally in [47] in a different setup, using non-identical molecules embedded in a crystal. Once the distance r_{12} is known, we may also determine the position of the two atoms relative to nodes of the standing wave field. For this, we note from Fig. 20(b) that—for otherwise fixed parameters—the position of the branching point depends on the effective Rabi frequencies $\Omega_1 = \Omega \sin(\phi)$, $\Omega_2 = \Omega \sin(\mathbf{k} \cdot \mathbf{r}_{12} + \phi)$, and thus on the position ϕ. If in the experiment we increase Ω up to the branching point, then the position of the atom pair relative to the standing wave field nodes can be deduced. Accurate analytic expressions for the position of the branching point, however, are difficult to obtain, as the general expression of the resonance fluorescence spectrum is complicated [81]. Thus a numerical fit as shown in Fig. 20(b) should be used to deduce the position ϕ.

If the distance between the two atoms is intermediate (about $\lambda/30 \leq r_{12} \leq \lambda/10$), then the initial weak field measurement in general yields a more complicated spectrum as, e.g., shown in Fig. 19(b). In this parameter range, neither the dipole-dipole coupling nor the driving field dominates the system dynamics. In such a case, a quantitative interpretation of the spectrum is difficult. In this case, increasing the Rabi frequency Ω leads to a spectrum as shown in Fig. 19(c). The spectrum consists of a central peak, two inner sideband doublets, and two outer sideband doublets, each symmetrically placed around the driving field frequency ω_L. The position of the inner and outer sideband doublets corresponds to the Rabi frequencies Ω_1 and Ω_2. The sideband structures are split into doublets due to the dipole-dipole coupling of the two atoms. For large Ω, the splitting approaches twice the energy Ω_{12}, as shown in Fig. 21(a). Thus the strong-field sideband doublet splitting directly yields Ω_{12} and thus the distance of the two atoms, again via Eqs. (4.7) or (4.8). For example, in Fig. 19(c), the theoretical estimate for the dipole-dipole potential is $\Omega_{12} = 10.59\gamma$ for a distance of $r_{12} = 0.08\lambda$. From the spectrum, we obtain $\Omega_{12} = (10.54 \pm 1.05)\gamma$,

where again we have allowed for an uncertainty of about 10%. From Eq. (4.7), this yields a measured distance of $r_{12} = (0.0801 \pm 0.0027)\lambda$, in good agreement with the actual value. Hence the position information can be gained. In the strong field limit, the mean frequency of the two peaks of each sideband structure corresponds to the Rabi splitting Ω_1 or Ω_2, respectively, such that (from a comparison with Ω) the positions of the individual atoms relative to standing wave field nodes can be obtained. For the setup in Fig. 19(c), we have $\phi = 0.1\pi$, $\Omega_1 = 61.80\gamma$, $\Omega_2 = 145.79\gamma$. From the spectrum, using the above procedure we obtain $\Omega_1 = (61.58 \pm 6.16)\gamma$, $\Omega_2 = (146.22 \pm 14.62)\gamma$, assuming a relative uncertainty of 10%. From $\phi = \arcsin(\Omega_1/\Omega)$, this would yield a measurement result of $\phi = (0.100 \pm 0.010)\pi$, in good agreement with the actual position of the atoms. In this intermediate distance regime, the situation slightly complicates if both atoms are located near-symmetrically around a node or an anti-node. In this case, $\Omega_1 \approx \Omega_2$, such that the two sideband doublets overlap. Then it is not obvious which peak belongs to which structure. One way to resolve this is to slightly change the standing wave field phase, such that the nodes and anti-nodes move. By this, the symmetry can be lifted to give $\Omega_1 \neq \Omega_2$. In this way the above procedure can be applied to give the separation and the positions.

If the two atoms are well-separated (about $\lambda/10 \leq r_{12} \leq \lambda/2$), then the dipole-dipole interaction contribution is negligible. In this case spectra as shown in Fig. 19(d) are obtained. The two sideband structures again can be interpreted as arising from the AC-Stark splitting due to Ω_1 and Ω_2. This time, however, the sideband peaks are not split into doublets, as Ω_{12} is small. Thus the sideband peak positions can directly be related to Ω_1 and Ω_2 and therefore to the position of the two atoms relative to the standing wave field nodes. Within one wavelength, however, in general several combinations of the positions of the two atoms are possible for measured values of Ω_1 and Ω_2 (see Fig. 21(b,c)) [83]. The additional knowledge of a large distance may allow

us to rule out some of the possible combinations as they would entail a non-vanishing dipole-dipole coupling. An identification of the actual atomic positions is possible by changing the standing wave phase, i.e. shifting the positions of the (anti-) nodes slightly. As shown in Fig. 21(b,c), a combination of the possible positions for two different standing wave phases enables us to obtain the positions of the two atoms, and thus the atomic separation. It may also be possible to use alternative schemes to restrict possible positions for the atoms, e.g. using phase-dependent schemes as discussed in [83] for single atoms. Note that this complication is not present for the case of nearby atoms, where the non-vanishing dipole-dipole energy allows to determine the distance directly.

E. Intensity-Intensity Correlation Function and Distance Measurement

Using Eq. (4.30), we can numerically calculate the normalized intensity-intensity correlation function $g^{(2)}(\tau)$. The results show very distinct behavior for different interatomic distance ranges. Fig. 22 shows several examples of the correlation function $g^{(2)}(\tau)$ for different interatomic distances, with the parameters indicated there.

It turns out that the intensity-intensity correlation function itself cannot easily be interpreted in terms of the actual interatomic distance. Instead, it is more convenient to analyze the power spectrum of the intensity-intensity correlation functions. For simplicity, the power spectrum $S(\nu)$ of $g^{(2)}(\tau)-1$ is studied here. As $\lim_{\tau\to\infty} g^{(2)}(\tau) = 1$, the constant only gives rise to a delta peak contribution at a frequency of zero in the power spectrum of $g^{(2)}(\tau)$. From Eq. (4.30), it is easy to evaluate the Fourier transform of $g^{(2)}(\tau) - 1$ as:

$$S(\nu) = \frac{1}{\mathcal{N}} \sum_{j=1}^{15} \left(\frac{\imath\, P_j}{\nu + \Im(q_{jj}) - \imath\, \Re(q_{jj})} + \frac{\imath\, P_j^*}{\nu - \Im(q_{jj}) - \imath\, \Re(q_{jj})} \right) . \tag{4.34}$$

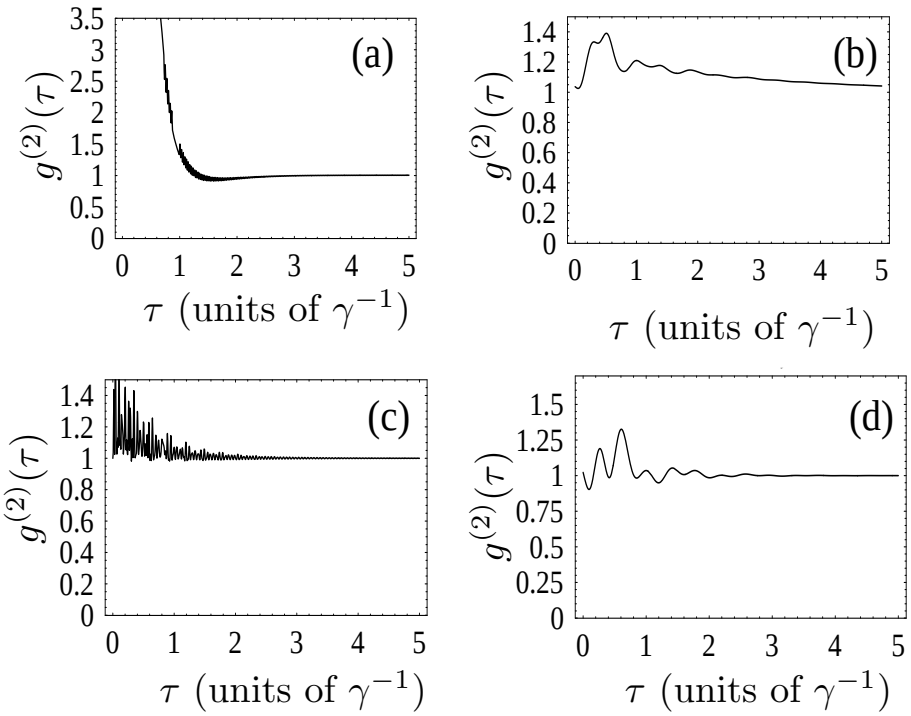

Fig. 22. Samples of $g^{(2)}(\tau)$ for $\Delta = 0$, $\hat{\mathbf{R}}_1 \cdot \mathbf{r}_{12} = \hat{\mathbf{R}}_2 \cdot \mathbf{r}_{12} = 0$, $kz_1 = 0.1\pi$. (a) Small distance case: $z_{12} = 0.03\lambda, \Omega = 20\gamma$; (b) Intermediate distance, weak driving field: $z_{12} = 0.08\lambda, \Omega = 20\gamma$; (c) Intermediate distance, strong driving field: $z_{12} = 0.08\lambda, \Omega = 300\gamma$; (d) Large distance case: $z_{12} = 0.6\lambda, \Omega = 20\gamma$.

Here, $\mathcal{N} = 2\sqrt{2\pi}[G^{(1)}(\mathbf{R}, \infty)]^2$ is a normalization constant, and $\Im(x)$ and $\Re(x)$ denote the imaginary and the real part of x, respectively. The power spectrum $|S(\nu)|$ is shown in Fig. 23, 24, 25, 26, with same parameters as in Fig. 22. With the help of Fig. 23, 24, 25, 26, it is clear that the different behavior of the intensity-intensity correlation functions is due to different frequency components dominating the system. These frequency components are related to the position and distance information of the two atoms. With the help of Eq. (4.34), we can use the two atomic position parameters z_1 and z_{12} to fit the measured correlation function and spectrum using well-developed experimental data analysis techniques. This process provides the position and distance information between the two atoms.

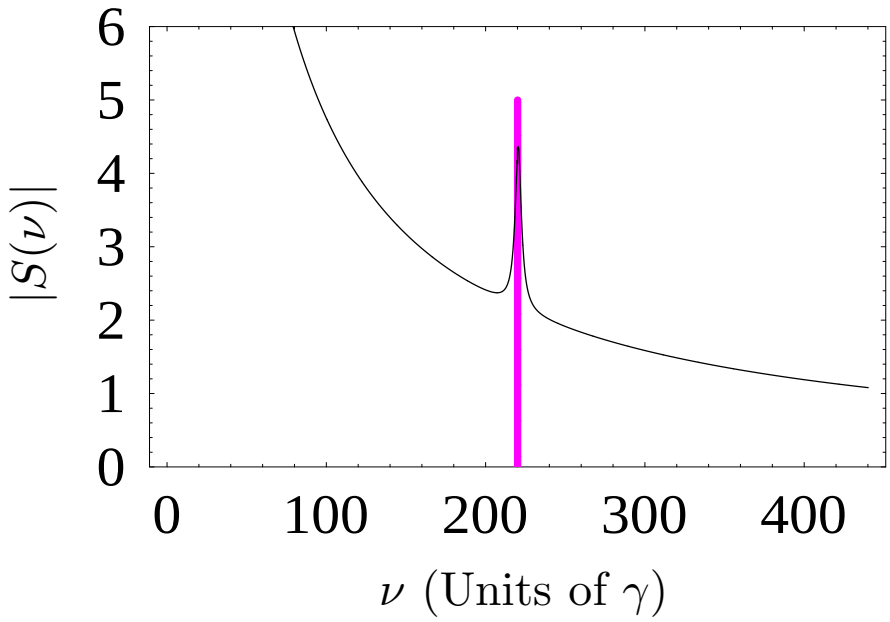

Fig. 23. Power spectra of the $g^{(2)}(\tau)$ sample shown in Fig. 22 (a). Small distance case: $z_{12} = 0.03\lambda, \Omega = 20\gamma$. The dash-dotted line indicates the position of Ω_{12}.

Based on the intensity-intensity correlation function of the resonance fluorescence light field, we are able to extract spacial information out by evaluating the power spectrum from it and fitting it numerically. However, our investigation of the properties of $g^{(2)}(\tau)$ and $|S(\nu)|$ show that in certain limiting cases, it is possible to obtain the distance and position information directly from the power spectrum with satisfactory precision, i.e., without the fitting of the full spectrum. This will be discussed together with the measurement procedure in the following.

Again, the first step is to apply a standing wave laser field to the two-atom system, which corresponds to a maximum Rabi frequency Ω of about 20γ for an atom sitting at an anti-node of the standing wave. The laser propagation direction is along the connection vector $\mathbf{r}_{12}$ of the two atoms. Since we are working on the far field region and the interatomic distance is much smaller than the distance from atoms system to the detectors, we can always arrange the two photon detectors at

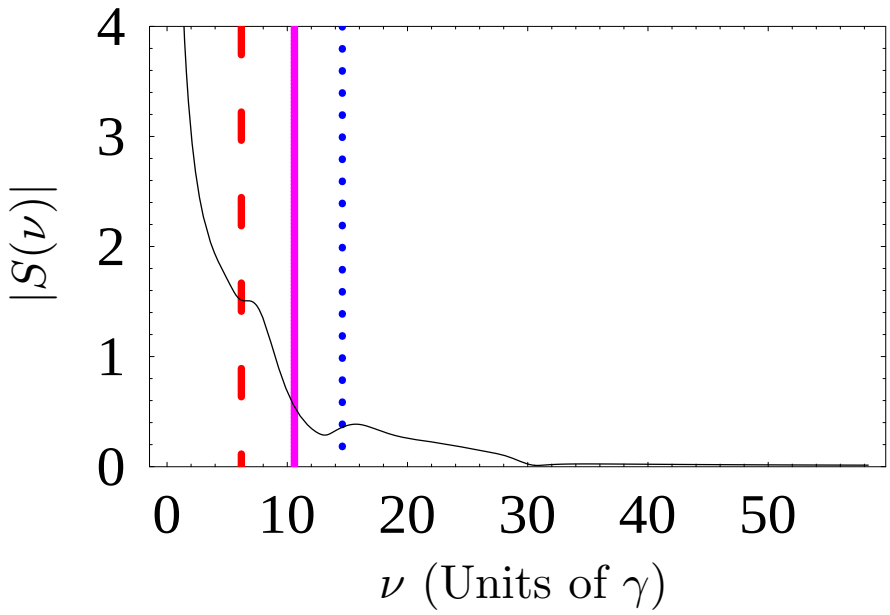

Fig. 24. Power spectra of the $g^{(2)}(\tau)$ samples shown in Fig. 22(b). Intermediate distance, weak driving field: $z_{12} = 0.08\lambda, \Omega = 20\gamma$. The solid line indicates the position of Ω_{12}, the dashed line indicates the position of Ω_1, and the dotted line indicates the position of Ω_2.

positions $\mathbf{R}_1$ and $\mathbf{R}_2$ with $R_1 = R_2$ and directions perpendicular to the interatomic distance vector ($\mathbf{R}_1 \perp \mathbf{r}_{12}$, $\mathbf{R}_2 \perp \mathbf{r}_{12}$). Using coincidence measurement techniques, the intensity-intensity correlation function of the emitted light field can be measured. Based on the results of the $g^{(2)}(\tau)$ measurement, three different parameter ranges can be distinguished:

(a) If $g^{(2)}(\tau)$ and its power spectrum are similar to those in Fig. 22(a) and Fig. 23, then the interatomic distance is small ($z_{12} \leq \lambda/30$). In Fig. 22 (a) and Fig. 23, the actual interatomic distance is $z_{12} = 0.03\lambda$, which corresponds to an interaction energy of $\Omega_{12} = 220.096\gamma$. The system evolution is dominated by the dipole-dipole interaction energy Ω_{12}, which gives rise to a single peak structure in the $g^{(2)}$ spectrum. As shown in Fig. 23, the peak center ν_{p} is coincident with the dipole-dipole interaction coefficient Ω_{12} indicated by a dash-dotted line. Thus, a

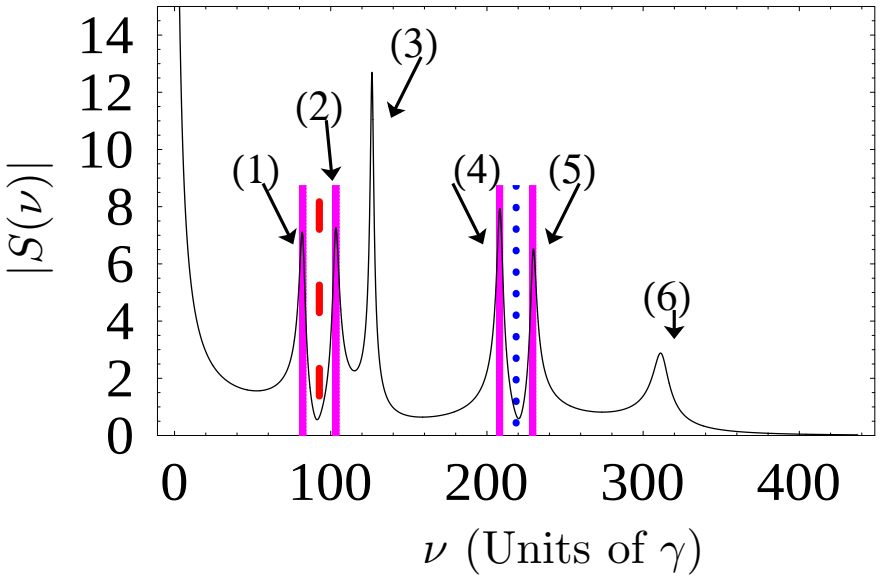

Fig. 25. Power spectra of the $g^{(2)}(\tau)$ samples shown in Fig. 22(c). Intermediate distance, strong driving field: $z_{12} = 0.08\lambda, \Omega = 300\gamma$. The solid lines indicate the positions of $\Omega_1 \pm \Omega_{12}$ and $\Omega_2 \pm \Omega_{12}$, the dashed line indicates the position of Ω_1, and the dotted line indicates the position of Ω_2 .In the spectrum, the peaks (1), (2), (3), (4), (5) and (6) correspond to frequencies $\Omega_1 - \Omega_{12}, \Omega_1 + \Omega_{12}, \Omega_2 - \Omega_1, \Omega_2 - \Omega_{12}, \Omega_2 + \Omega_{12}$ and $\Omega_1 + \Omega_2$.

measurement of the peak position ν_{p} allows us to gain an estimate of Ω_{12} and thus of the interatomic distance via Eq. (4.7).

In a measurement, two error sources have to be distinguished. The first error source is related to experimental imperfections, and corresponds to uncertainties in the measurement of the spectra shown in Fig. 23, 24, 25, 26. In the following, for simplicity, we will cover such uncertainties by an overall relative experimental uncertainty U^{exp}.The position of the peak in the spectrum Fig. 23 is $\nu_p = 220.49\gamma$. Assuming an experimental uncertainty of $U^{exp} = 10\%$, the experimentally accessible value for Ω_{12} thus is $\Omega_{12}^{exp} = (220.49 \pm 22.05)\gamma$. From Eq. (4.7), Ω_{12}^{exp} yields a measured distance of $z_{12}^{exp} = (0.030 \pm 0.001)\lambda$, which is in very good agreement with the actual

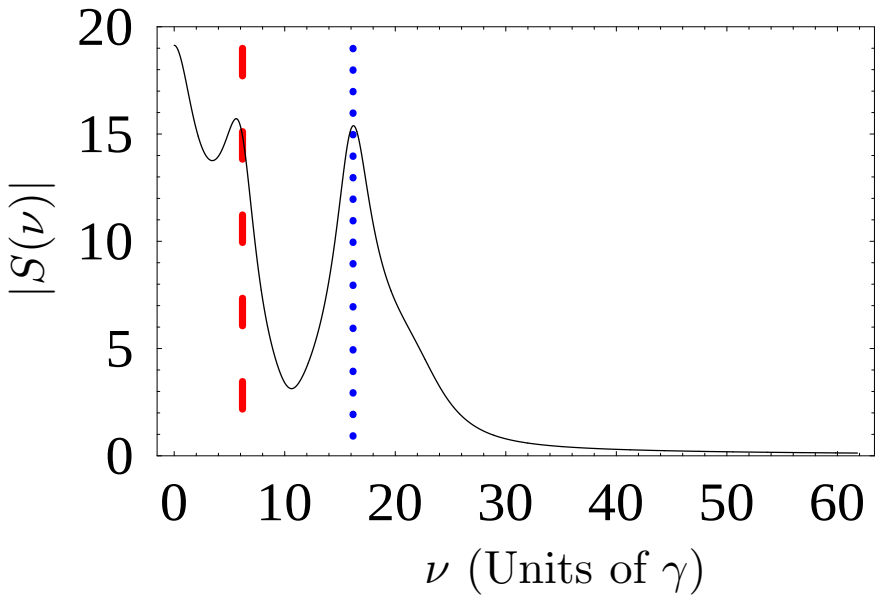

Fig. 26. Power spectra of the $g^{(2)}(\tau)$ samples shown in Fig. 22(d). Large distance case: $z_{12} = 0.6\lambda, \Omega = 20\gamma$. the dashed line indicates the position of Ω_1, and the dotted line indicates the position of Ω_2.

value $z_{12} = 0.03\lambda$. Note that due to the structure of Eq. (4.7), for small distances, the experimental uncertainty of z_{12}^{exp} is only about $U^{exp}/3$ [49]. In this example, the absolute measurement uncertainty for the distance is less than 0.4% of the wavelength λ.

The second source is a systematic error, and is due to the fact that the peak position $\nu_{\rm p}$ accessible in experiments does not exactly coincide with the theoretical interaction energy Ω_{12}. This deviation is generally negligible for small interatomic distances, but will be discussed further below in this subsection.

If we look more closely at the details of the peak in Fig. 23, it reveals a more complicated structure. In Fig. 27, it can be seen that the dominating peak is overlayed by a Fano-like "spike" structure. One way of avoiding such complications is to adjust the geometry of the system to the setup in Fig. 18(b), where the driving field propagates perpendicular to the interatomic distance vector of the two atoms. In this

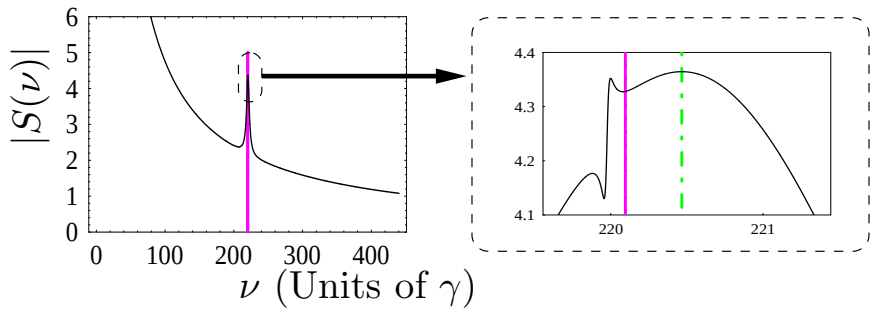

Fig. 27. Detailed spectra for small interatomic distances under different alignments. The two atoms are aligned along the propagation direction of the driving field, as shown in Fig. 18 (a)In the enlargements, solid vertical lines indicate the actual value of Ω_{12}, whereas the dashed lines indicate the peak center of the plotted spectra.

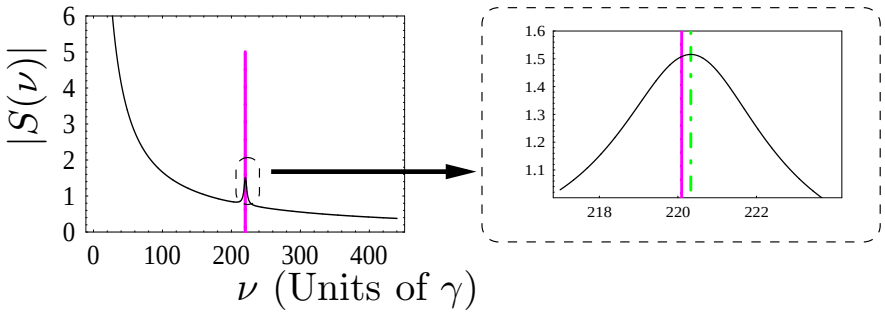

Fig. 28. Detailed spectra for small interatomic distances under different alignments. (The interatomic distance vector is perpendicular to the laser propagation direction, as shown in Fig. 18(b). In the enlargements, solid vertical lines indicate the actual value of Ω_{12}, whereas the dashed lines indicate the peak center of the plotted spectra.

configuration, the two atoms see the same driving field ($\Omega_1 = \Omega_2$). This symmetry simplifies the power spectrum of $g^{(2)}$, as shown in Fig. 28. On the other hand, resolving this structure in the experiment may provide a more accurate measurement of the interatomic distance, as discussed in the next paragraph.

We now turn to a more thorough study of the deviation of the experimentally

accessible peak position $\nu_{\rm p}$ from the theoretical value of Ω_{12} in the geometry described in Fig. 18(a). Fig. 29 shows this relative deviation $U_d = (\nu_{\rm p} - \Omega_{12})/\Omega_{12}$ versus the atomic separation for different Rabi frequencies Ω of the driving field. Fig. 31 shows the deviation U_d versus the Rabi frequency for different positions of the first atom. It is apparent that as long as $\Omega, \gamma \ll \Omega_{12}$ is satisfied, the peak position $\nu_{\rm p}$ can directly be identified with Ω_{12}; the deviation U_d is much smaller than 1%. If for a specific setup the experimental uncertainties U^{exp} are smaller than U_d, then the accuracy of the distance measurement can be maximized by fitting the whole $g^{(2)}$ spectrum numerically, taking the approximate results of the above scheme as a starting point. In Fig. 29 and Fig. 31, we also find branching points similar to those found in our previous work [49]. However, it is very difficult to get accurate analytic relations between the position of the branching points and the system parameters of interest without a numerical fit. Therefore, here we only focus on the distance information. One can, however, also take advantage of the "spike" as shown in Fig. 27 instead of avoiding it by switching to a new alignment. A numerical investigation shows that the position $\nu_{\rm d}$ of the dip behind this "spike" is much closer to Ω_{12} than the peak position $\nu_{\rm p}$ found in the previous part. For example, in Fig. 27, one finds $\nu_{\rm d} = 220.079\gamma$, such that the deviation from Ω_{12} is only 0.008%. This is significantly less than the deviation between $\nu_{\rm p}$ and Ω_{12}, which is approximately 0.17%. Thus the systematic error U_d of this method is very small, and the error of the final result will dominated by the other error sources summarized in U^{exp}.

(b) If the measured $g^{(2)}(\tau)$ and its power spectrum are similar to those in Fig. 22(b) and Fig. 24, then the interatomic distance is in the range $\lambda/30 - \lambda/10$, which we call the "intermediate distance case". In this regime, the effect of the driving field and the dipole-dipole interaction between the two atoms are comparable to each other. As a result, the correlation function and its power spectrum are rather

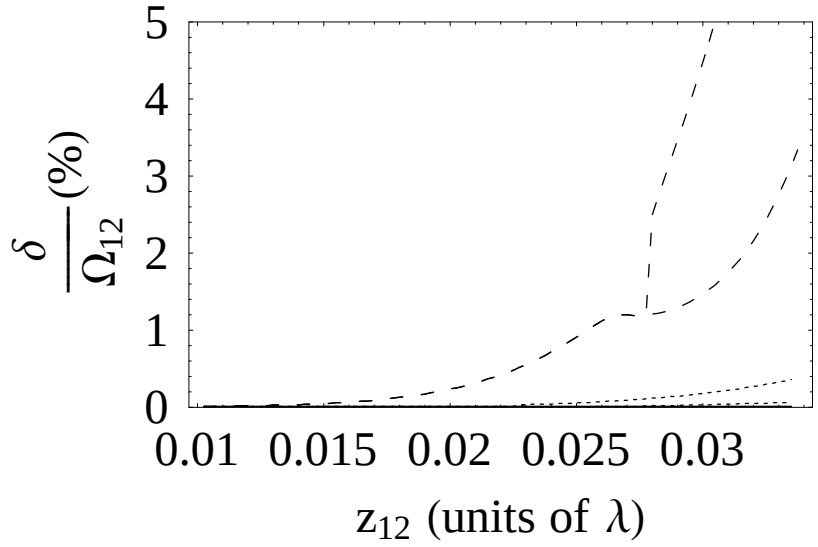

Fig. 29. Deviation $\delta/\Omega_{12} = (\nu_{\rm p}-\Omega_{12})/\Omega_{12}$ of the peak position $\nu_{\rm p}$ from Ω_{12} for closely-spaced atoms in the geometry shown in Fig. 18(a). $\Delta = 0$, $\hat{\mathbf{R}}_1\cdot\mathbf{r}_{12} = \hat{\mathbf{R}}_2\cdot\mathbf{r}_{12} = 0$, and plotted against the interatomic separation. $kz_1 = 0.1\,\pi$, $\Omega = 3$ (solid), 20 (doted), 80 (dashed). Branches correspond to splittings into two peaks.

complicated. All frequency components related to these two interactions and their combinations show up in the power spectrum. One way of avoiding this complication is to increase the intensity of the driving field, typically such that the maximum Rabi frequency reaches about 200γ. While the driving field intensity is increased, one continuously measures the intensity-intensity correlation function and its power spectrum. Eventually, the spectrum looks like Fig. 25, where all the frequency peaks are well separated, and there are two doublets which maintain the same doublet-splitting σ_s during the increase of the field intensity. These doublets can be identified with the frequencies $\Omega_1 \pm \Omega_{12}$ and $\Omega_2 \pm \Omega_{12}$. For example, in Fig. 25, the theoretical value for $2\Omega_{12}$ is 21.189γ, corresponding to an actual value of $z_{12} = 0.08\lambda$. On the other hand, the experimentally accessible splitting of the doublet around Ω_1 is $\sigma_s = 21.63\gamma$. Allowing for an experimental uncertainty $U^{exp} = 5\%$, the measured splitting thus is

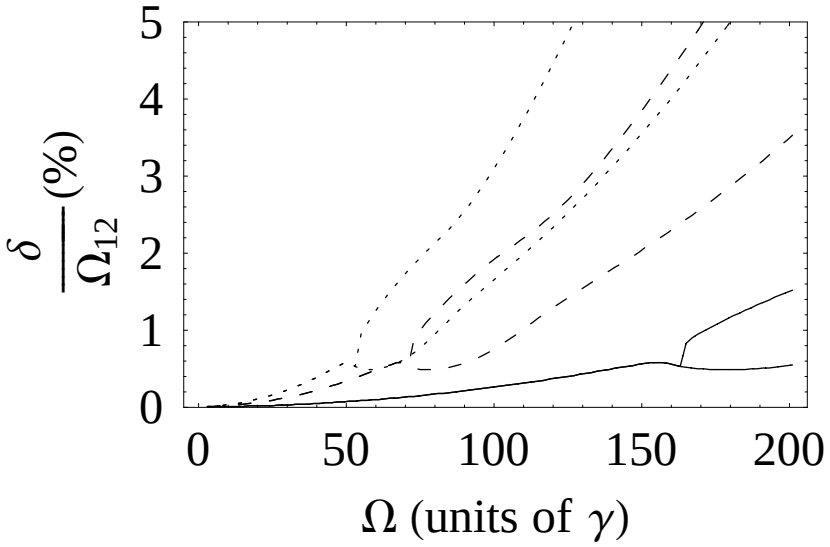

Fig. 30. Deviation $\delta/\Omega_{12} = (\nu_{\rm p}-\Omega_{12})/\Omega_{12}$ of the peak position $\nu_{\rm p}$ from Ω_{12} for closely-spaced atoms in the geometry shown in Fig. 18(a). $\Delta = 0$, $\hat{\mathbf{R}}_1\cdot\mathbf{r}_{12} = \hat{\mathbf{R}}_2\cdot\mathbf{r}_{12} = 0$, and plotted against the driving field Rabi frequency. $z_{12} = 0.02\,\lambda$, $kz_1 = 0.1\,\pi$ (dotted), $kz_1 = 0.25\,\pi$ (solid), $kz_1 = 0.4\,\pi$(dashed). Branches correspond to splittings into two peaks.

$2\Omega_{12}^{exp} = (21.63 \pm 1.1)\gamma$. Using Eq. (4.7), the measured interatomic distance evaluates to $z_{12}^{exp} = (0.079 \pm 0.0014)\lambda$, which again is in good agreement with the actual value.

We now turn to the discussion of the systematic error sources in this case. Fig. 31 shows the relative deviation $U_d = (\nu_p - \Omega_{12})/\Omega_{12}$ of the experimentally accessible doublet splitting σ_s from the desired value $2\Omega_{12}$ versus the driving field Rabi frequency for different position of the first atom. It can be seen that this deviation can be kept less than 5%, if the driving field is strong enough ($\Omega \gg \Omega_{12}$). Apart from increasing the intensity of the driving field, the field phase can also be adjusted such that the atoms come close to a node. Then, the effective Rabi frequencies Ω_1 and Ω_2 increase. Again, more accurate information can be obtained by a numerical fit of the measured spectrum, starting from the approximate values obtained via the above scheme.

(c) Finally, if the $g^{(2)}(\tau)$ and its power spectrum are similar to those in Fig. 22(d)

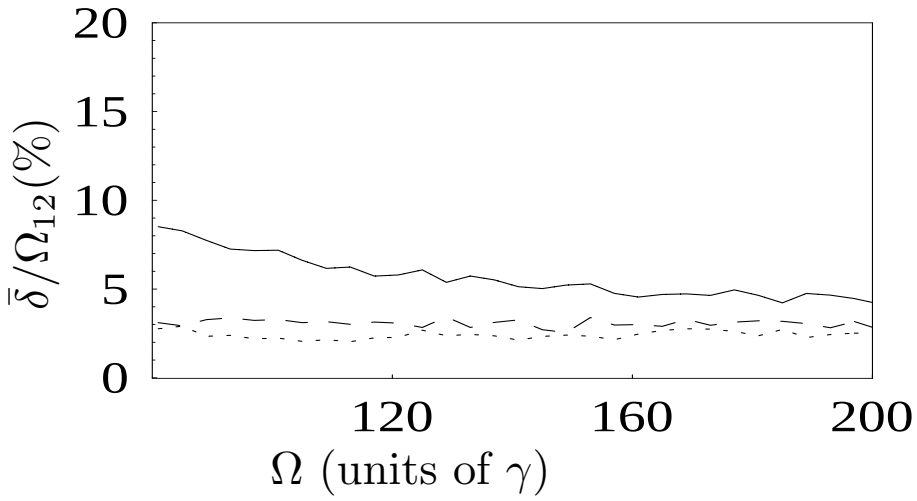

Fig. 31. Deviation $\bar{\delta} = \sigma_{\rm p} - 2\Omega_{12}$ of the doublet splitting $\sigma_{\rm p}$ from $2\Omega_{12}$ for the strong field, intermediate distance case. $r_{12} = 0.08\lambda$, $\theta = \pi/2$, and $\Delta = 0$. The positions of the atoms are $\phi = 0.1$ (solid), 0.2 (dashed), 0.3 (dotted).

and Fig. 26, it means that the interatomic distance is much larger than in the previous two cases. Here we suppose that the two atoms are confined to within one quarter of a wavelength, as larger distances are accessible by classical measurement schemes, or by the scheme considered in our previous work [49]. For larger distances, the dipole-dipole interaction is very small. The system is dominated by the interaction between the atoms and the laser field. The two peak visible in Fig. 26 in the spectrum of $g^{(2)}$ correspond to the Rabi frequencies Ω_1 and Ω_2 seen by the two atoms. The two peaks can be identified easily by increasing the driving field intensity. The interatomic distance r_{12} can then be evaluated through the expressions Eq. (4.9) for Ω_1 and Ω_2.

F. Discussions

Detection Geometry Issue: Up to this point, we have focussed our analysis on a system geometry where both detectors are equidistant to the scattering atom pair and aligned orthogonal to the interatomic distance vector. The two-photon cor-

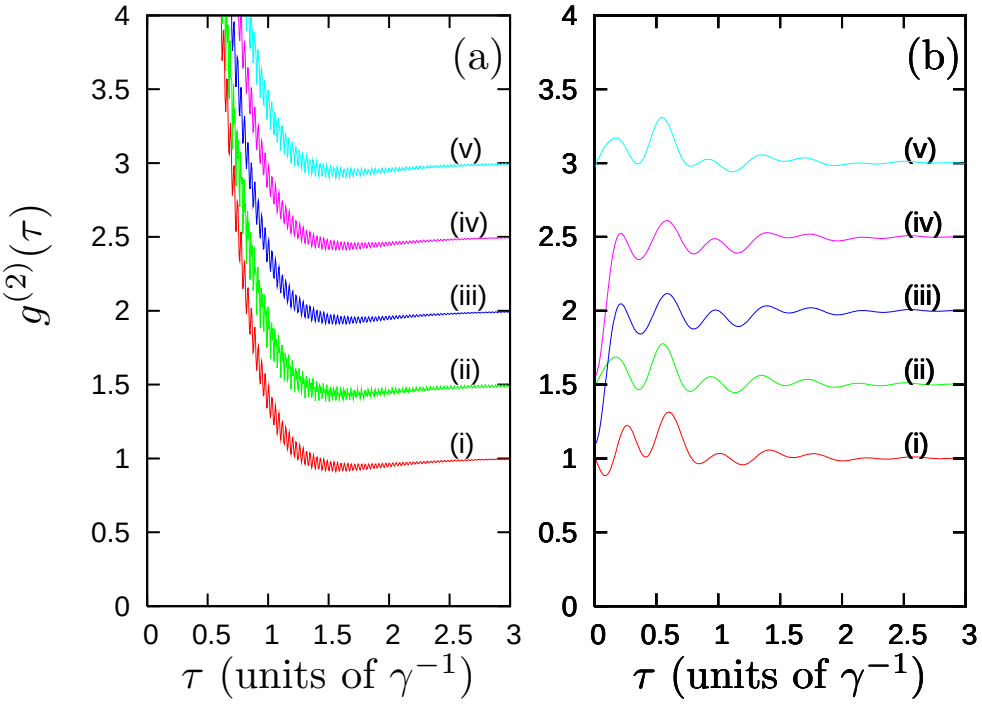

Fig. 32. Dependence of the intensity-intensity correlation function on the geometrical setup of the detectors. Subfigure (a) corresponds to the small distance case, with parameters as in Fig. 22(a), whereas subfigure (b) shows the large-distance case as in Fig. 22(d). The respective curves in the subfigures correspond to different detector setups: (i) $\theta_1 = \pi/2, \theta_2 = \pi/2$, (ii) $\theta_1 = 0, \theta_2 = 0$, (iii) $\theta_1 = \pi/2, \theta_2 = 0$, (iv) $\theta_1 = \pi/2, \theta_2 = \pi/4$, (v) $\theta_1 = \pi/4, \theta_2 = \pi/4$. Here, θ_i ($i \in \{1, 2\}$) are the angles between the interatomic distance vector $\mathbf{r}_{12}$ and the observation directions $\mathbf{R}_i$ of the two detectors. Note that the curves have been shifted by integer multiples of 0.5 in y-direction in order to allow for a comparison. Without this artificial shift, all curves roughly coincide with the respective curves (i), but with different high-frequency modulation structure in (a), and different values for $\tau \to 0$ in (b).

relation function, however, is also known to exhibit angular correlation effects for different detector positions [87]. Results for the intensity-intensity correlation function for several detection setups are shown in Fig. 32. It can be seen that the shape of the correlation function does change with the detection geometry. For example,

in Fig. 32(b), curves (i), (ii) and (iv) tend to 1 for $\tau \to 0$, whereas curves (iii) and (iv) tend to 0 in this limit. The corresponding power spectra are shown in Fig. 33. From this figure it is apparent that the observables crucial to our distance analysis, namely, the positions of the different peaks in the power spectrum, are hardly affected by the detector setup. This can intuitively be understood from our analysis of the peak structure in Fig. 25. There we found that the peak positions depend on characteristic frequencies determined by the internal dynamics of the two-atom system, which is independent of the external detector geometry. Thus, one can expect the peak positions to be unaffected by the detection system, whereas the peak amplitudes are subject to amplification or attenuation due to spatial interference effects. For example, in Fig. 25(b), the amplitude of the left peak at around $\nu = 6\gamma$ strongly depends on the detection geometry, further supported by an overall attenuation of the power spectrum for certain detector positions. From our numerical analysis, we find that the detector positions shown in Fig. 18 and used throughout our analysis are well-suited for the whole range of considered distances.

Limitation Issue: The possible range of separation between the two atoms which can be measured is limited, as the dipole-dipole coupling Ω_{12} rapidly increases with decreasing separation as r_{12}^{-3}. For our model to remain valid, however, $\Omega_{12} \ll \omega_0$ should be fulfilled, as otherwise also counter-rotating terms should be included in the master equation Eq. (4.1). From Eq. (4.8), we find $r_{12} \sim [3\gamma/(2k^3\Omega_{12})]^{1/3}$. For $\gamma \sim 10^7$ Hz, $\Omega_{12} \leq 10^{13}$ Hz, we obtain $r_{12} \geq \lambda/550$. For a typical wavelength of 500 nm, the minimum separation is about 9Å. Note that this limitation only applies to the distance of the two atoms itself; the uncertainty of the distance measurement can be well below $\lambda/550$. Another limitation arises from electron shell deformations, if the interatomic distance approaches the spatial extend of the atomic wavefunctions.

Fundamental constraints also arise from quantum or thermal uncertainties in the

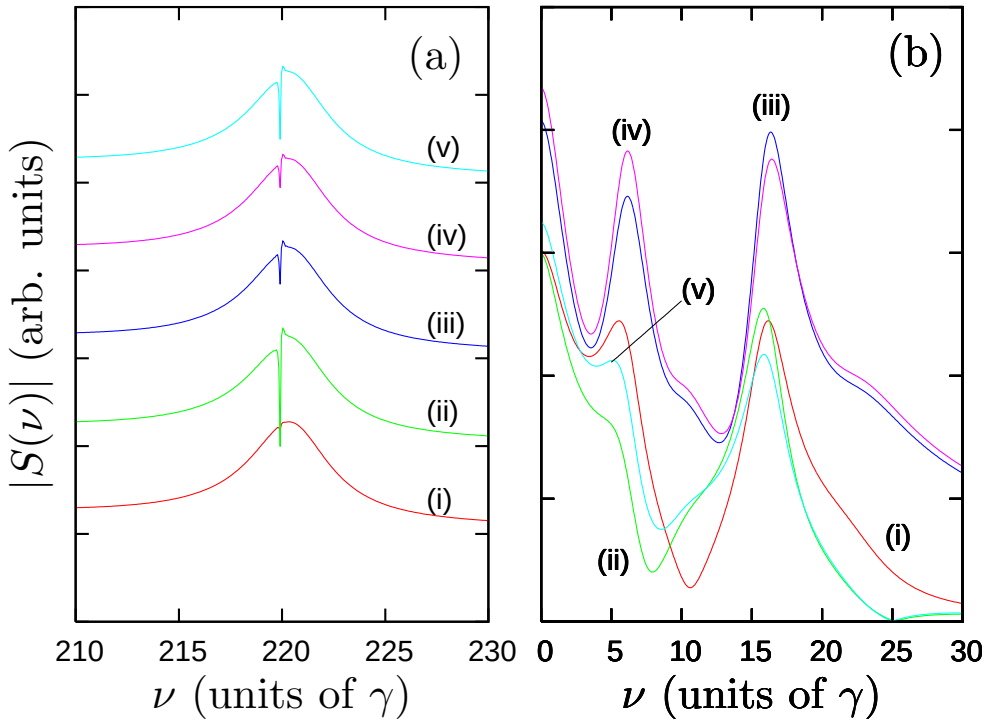

Fig. 33. Power spectra of the intensity-intensity correlation functions shown in Fig. 32. In subfigure (a), the curves have been shifted by integer multiples of 0.5 in y-direction in order to allow for a comparison. In subfigure (b), no additional shift has been applied.

position of the particles. Note, however, that for harmonic oscillations of the particles around their equilibrium positions, the classical turning points of the motion can be measured via the optical far-field properties. These again allow to determine the mean interactomic distance [49].

Summary: In summary, we discussed the properties of the resonant fluorescence spectrum and the intensity-intensity correlation function of the fluorescence field emitted by two nearby atoms placed inside a standing wave laser field. In particular, we showed how interatomic distance information can be obtained by analyzing the power spectrum of the correlation function. Our scheme allows to measure interatomic distances from the classical refraction limit $\lambda/2$ down to about $\lambda/550$ using

detectors with state-of-the-art time resolution. For a typical optical wavelength, the range is thus from several hundred nanometers to few nanometers.

CHAPTER V

XUV RADIATION GENERATION VIA RAMAN SUPERRADIANCE

In this chapter we discussed another important application of cooperative effect , which is that the intense short pulses of XUV radiation can be produced by Raman superradiance from visible or IR laser pulses driving atoms or ions. The process depends on the generation and utilization of atomic coherence as is the case in lasing without inversion. However, the radiation process is not stimulated emission, but is rather cooperative spontaneous emission in the sense of Dicke. More precisely, the many atom mathematics of the problem is the same as that of coherent anti-Stokes Raman scattering.

In the following we present and develope the physics behind XUV generation via Raman superradiance. After a short introduction in section A, in section B we discuss the Raman superradiance process in the weak excitation limit (including single photon excitation); In section C we then discuss preparation of the Raman coherence, which is characterized by the density matrix element ρ_{bd} in the notation of Fig. 34a. In particular we study the generation of Raman coherence via via breaking of adiabatic; And finally in section D we provide several discussions and conclusions.

A. Introduction

Quantum coherence has been used to make novel lasers which operate without population inversion [88]. Another kind of coherent emission of radiation without population inversion is Dicke superradiance [1] which is not a stimulated emission process but rather a cooperative spontaneous emission process. In the present paper, we propose and analyze a new kind of XUV source based on conversion of short pulses of IR and/or visible radiation via a hyper Raman process [89], as depicted in Fig. 34.

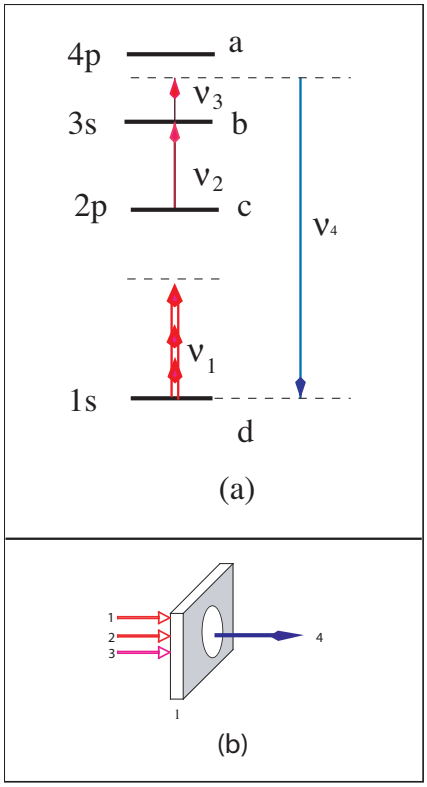

Fig. 34. (a) Level scheme. Double line indicates strong driving field with frequency ν_1 and Rabi frequency Ω_1 coupling states $|d\rangle$ and $|c\rangle$ via multiphoton absorbtion, or breaking adiabaticy etc. The detuning between the field frequency and the transition energy ω_{cd} is $\Delta = \omega_{cd} - \nu_1$. Subsequently the second (π-pulse) field with frequency ν_2 resonant with ω_{bc} is applied; The third pulse with frequency ν_3 then scatters off the Raman coherence generated by the first two pulses producing the XUV field 4. The detuning between field 3 and transition energy from a to b is $\delta = \omega_{ab} - \nu_3$. (b) Sketch of a gas or solid of thickness l containing the atoms.

In the first step we excite the atoms (e.g., from the $1s$ to $2p$ states of H or He^+, etc.) via a short pulse of femto- or attosecond radiation (e.g., from a conventional Ti-sapphire laser system). The degree of excitation is governed by the ratio of the Rabi frequency Ω to the atomic excitation frequency ω, and/or by rapidly switching the atom-field coupling. In the systems we envision Ω/Δ can easily be of order 10^{-2} to 10^{-1}. The second (π-pulse) field with frequency ν_2 resonant with ω_{bc}, the transition frequency between level $|b\rangle$ and $|c\rangle$ (see Fig. 34), is applied. As we shall see this is sufficient to generate ultra short intense pulses of XUV radiation.

Table I. Parameters of ns, ps, and as pulses. The transition dipole moment can be expressed as $\wp = \sqrt{3\pi\epsilon_0\hbar c^3\gamma_0/\omega^3} \simeq 0.5 \times 10^{-29}$ Cm, where γ_0 is the single atom decay rate from level $|c\rangle$ to $|d\rangle$. The Rabi frequency is given by $\Omega = \frac{\wp}{\hbar}E = \wp\sqrt{W/(\epsilon_0 Ac\tau)}$.

	picosecond	femtosecond	attosecond
pulse energy, W(μJ)	1 to 10^3	1 to 10^3	1 to 10^3
pulse area, A (mm^2)	10^{-2}	10^{-2}	10^{-2}
pulse length, τ	1.0 ps	10 fs	100 as
Detuning, Δ (eV)	1.0 (Cs)	10 (H)	10^2 (Li^+)
Radiation fequency, ν (eV)	0.1	1.0	10.0
Edge frequency α/Δ	0.1	0.1	0.1
Rabi frequency, Ω/Δ	10^{-2} to 10^{-1}	10^{-2} to 10^{-1}	10^{-2} to 10^{-1}

In the second step, we apply another pulse which scatters off the Raman coherence (prepared in step one), generating short wavelength anti-Stoke radiation as

depicted in Fig. 1. As noted earlier [90], the generation of the anti-Stokes field is a co-operative spontaneous emission process. That is, the radiation rate will be governed by $N\gamma$ where N is the number of radiators and γ is the Weisskopf-Wigner decay rate of a single atom. Another important aspect of Raman Superradiance is that (contrary to conventional superfluorescence) we do not require gain or population inversion, see Fig. 35. As Dicke [23] has noted in a similar context:

> It should be noted that this idealized "laser" [our quotes] continues to radiate coherently long after the lower energy level has a population greater than the upper.

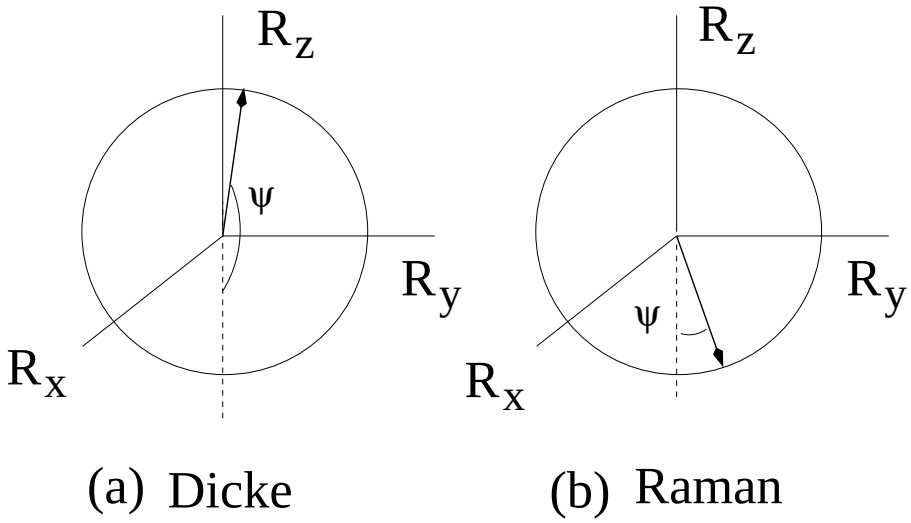

Fig. 35. (a) Orientation of Bloch vector for Dicke (a) and coherent Raman superradiance (b).

However, as is discussed in more detail below, the present decay rate Γ_N (going as N) should not be confused with the case of maximal superradiant emission, which goes as N^2.

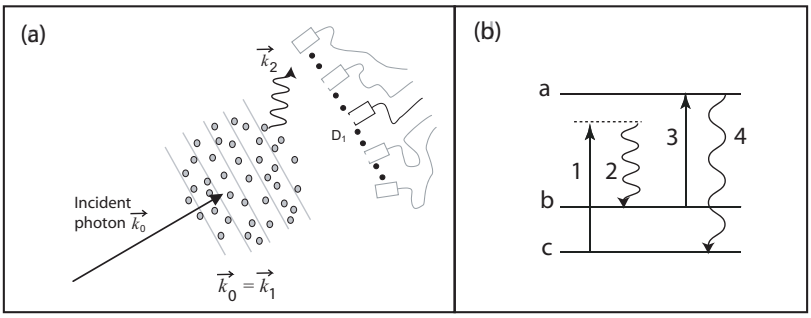

Fig. 36. (a) Proposed setup for conditional preparation and detection of directed spontaneous emission of photon from an extended ensemble of atoms via the Raman process in which an incident photon (1) is scattered from an ensemble of atoms and a Stokes photon (2) is generated. The observation of photon (2) conditions the atomic array such that one atom (but we don't know which one) is now in the b state. Upon detection of the conditioning photon a π pulse (3) is sent in and the atom in the b state is promoted to a state a. In this way, following Vuletic, we have prepared state given by Eq. (5.1).

B. Coherent Raman Superradiance

As that has been shown in Chapter III, the (conditional) N atom swept gain "timed" Dicke state

$$|+\rangle_{k_0} = \frac{1}{\sqrt{N}} \sum_j e^{i\vec{k}_0 \cdot \vec{r}_j} |b_1, b_2, ..., a_j, ..., b_N\rangle |0\rangle \ , \tag{5.1}$$

can be prepared via the conditional Raman process (see Fig. 36) and the decay from this $|+\rangle$ state to ground state as indicted in Fig. 2 will be an speeded exponential decay with the decay constant

$$\Gamma_N \approx \left(\gamma_0 \frac{N}{V} \lambda^2 R\right) \frac{\alpha}{2\pi^3} \, , \tag{5.2}$$

which we called single phone superradiance.

In the following we sketch a derivation of the generation of the anti-Stokes field. The effective Raman Hamiltonian may be written as

$$V(t) = \sum_j G_j \left(|d\rangle \langle b|\right)_j \hat{a}_3 \hat{a}_4^+ e^{-i(\omega_b + \nu_3 - \nu_4)t} + \text{adj} \tag{5.3}$$

where G_j is the Raman coupling strength between the j^{th} atom and the fields 3, 4 which are described by the annihilation ($\hat{a}_3$) and creation operators (a_4^+). For the present purposes, we may write the coupling constant as $G_j = g_3 g_4 (\delta + i\gamma)^{-1} e^{i(\vec{k}_3 - \vec{k}_4)\cdot\vec{r}_j}$; where $g_3 = (\wp_{ab}/\hbar)\mathcal{E}_3$ with $\wp_{ab}$ being the dipole matrix element between a, b and the electric field per photon $\mathcal{E}_3 = \sqrt{\hbar\nu_3/\epsilon_0 V}$ where ϵ_0 is the permittivity of free space and $V = Ac\tau$ is the volume of a pulse of area A and length $c\tau$. A similar expression for the coupling frequency g_4 connecting a, d applies with $\nu_3 \to \nu_4$. The detuning $\delta = \omega_{ab} - \nu_3$ is indicated in Fig. 34, γ is the coherence decay rate, $\vec{k}_4$ is the wave vector for the XUV mode, and $\vec{k_3}$ is the wave vector for the probe field.

Using the Heisenberg equation of motion for $\hat{a}_4$ with the Hamiltonian (5.3) to obtain $a_4(\tau)$, forming the number operator $a_4^\dagger(\tau)a_4(\tau)$ and taking expectation values we find

$$n_4 \cong n_3 \kappa^2 \left[\sum_i \rho_{bb}^i + \sum_{i \neq j} e^{i(\vec{k}_4 - \vec{\kappa})\cdot(\vec{r}_i - \vec{r}_j)} \rho_{db}^i \rho_{bd}^j \right], \tag{5.4}$$

where n_3 and n_4 are the average photon numbers, ρ_{ab}^i is the (Raman coherence) density matrix element for the i^{th} atom, $\kappa = (\wp/\hbar)^2(\hbar\nu/\epsilon_0 cA)/\delta$ and for simplicity we have set $\wp_{da} = \wp_{ab} = \wp$ and $\mathcal{E}_{03} = \mathcal{E}_{04} = \sqrt{\hbar\nu/\epsilon_0 V}$. Equation (5.4) is revealing since we can arrange that $\Omega_{03}\tau \sim \pi$ and $\Omega_{03} \sim \delta$ so that Equation (5.4) reduces to the familiar cooperative emission double sum over the atomic phase factors.

As is shown in detail in [20, 21], the double sum in Eq.(5.4) is the essence of Dicke superradiance in the low excitation limit such that the many atom decay rate is governed by $\gamma_0 N$ where γ_0 is the single atom decay rate. Similarly, we find that

the photon flux, in the case of the disc (Fig. 34b) and the needle is given by

$$n_4 = \begin{cases} \kappa_D \frac{\lambda^2}{A}(N|\rho_{bd}|)^2 n_3 & \text{Disk} \\ \kappa_N \frac{\lambda}{L}(N|\rho_{bd}|)^2 n_3 & \text{Needle} \end{cases} \tag{5.5}$$

where the constants $\kappa_D = (3/8\pi)\kappa^2$ and $\kappa_N = (3/8)\kappa^2$.

It is instructive to compare superradiance we have found here with classic works [9, 91, 92, 93]. Usually, superradiance (superflourecence) requires population inversion [1] which can be created by a strong laser pulse (see Fig. 35a). Then, the superradiant pulse is formed at some delay after excitation (lethargy time) and the pulse is shorter than the single atom decay time. Here, we applied laser fields that do not create population inversion between levels a and d, but induced atomic coherence on the superradiant transition is created. Also, it is important to understand the role of strong absorption in this case, because of larger population in the ground state. Following [7], let us introduce $\psi = \int_{-\infty}^{t} W_4(t')dt'$. Then the propogation equation is given by

$$\frac{\partial^2 \psi}{\partial z \partial t} = -\frac{3\lambda^2 \mathcal{N}\gamma_r}{8\pi} \sin(\psi + \psi_0) \tag{5.6}$$

where we introduce $\psi_0 = \rho_{bd} \int_{-\infty}^{+\infty} W_4(t')dt'$ that is determined by initial coherence (ρ_{bd}) induced by the laser fields, and $\mathcal{N} = N/V$ is the density of atoms, λ is the wavelength of the transition, and γ_r is the rate of spontaneous emission. For small initial angles, $\psi_0 \ll 1$, the solution is given by [54] $\psi(t,z) \simeq \psi_0 J_0\left(\sqrt{\frac{3\lambda^2 z\mathcal{N}\gamma_r t}{8\pi}}\right)$, where J_0 is the Bessel function. From this solution one can directly see that the emission accurs immediately, without any delay. The system does not need a build up time to phase and synchronize all atomic dipoles to start emission; and the pulse generated by the system, of duration $T_R = 8\pi/(3\lambda^2 \mathcal{N} z\gamma_r)$, may be much shorter than any relaxation times.

C. Generate Raman Coherence via Breaking of Adiabaticity

Given the small values of ρ_{bd} commonly associated with multiphoton excitation, we are motivated to investigate other ways of producing Raman coherence and turn now to generation of coherence via breaking of adiabaticity. To this end, we recall that for a step function (sharp) turn on of a pulse connecting $|d\rangle$ and $|c\rangle$ we have in the limit that $\Delta \gg \Omega$

$$C(t)_{\text{step}} \cong -\frac{2i\Omega_{10}}{\Delta}e^{i\Delta t} - \frac{2i\Omega_{10}}{\Delta}e^{(-i\frac{\Omega_{10}{}^2}{\Delta}t)} \ . \tag{5.7}$$

The product of Eq. (5.7) with $e^{-i\omega_c t}$ gives the time dependence of the "dressed" level $|c\rangle$. The high frequency term then yields a dressed state going as $e^{-i\nu_i t}$ while the second low frequency term in Eq. (5.7) goes essentially as $e^{-i\omega_c t}$. Eq. (5.7) might seem to say that the probability amplitude for the excited state is of order $2\Omega_{10}/\Delta$. This is misleading. Any pulse with rounded edges will yield a $C(t)$ which has a much reduced low frequency (second term in Eq. (5.7)) contribution. To understand this we recall that the population in $|c\rangle$ will tend to adiabatically follow the pulse. For example, the famous hyperbolic secant pulse of Hahn and McCall for which $\Omega_1(t) = \Omega_0 \ \text{sech}(\Omega_0 t)$ partially excites each atom to the excited state but for large times ($t >> \Omega_0^{-1}$) the atoms are always returned to the ground state.

Thus we are led to consider replacing the step function pulse shape by

$$\Omega_1(t) = \Omega_0(1 + \tanh(\alpha t)) \ . \tag{5.8}$$

As will be discussed in detail elsewhere Eq. (5.8) yields

$$C(t)_{\text{tanh}} \cong \frac{2\Omega_0}{\Delta}e^{i\Delta t} - \frac{\sinh(\pi\Omega_0/\alpha)}{\sinh(\pi\Delta/\alpha)}e^{i8\Omega_0^2 t/\Delta}. \tag{5.9}$$

Usually, the low frequency term will be exponentially small and only the high

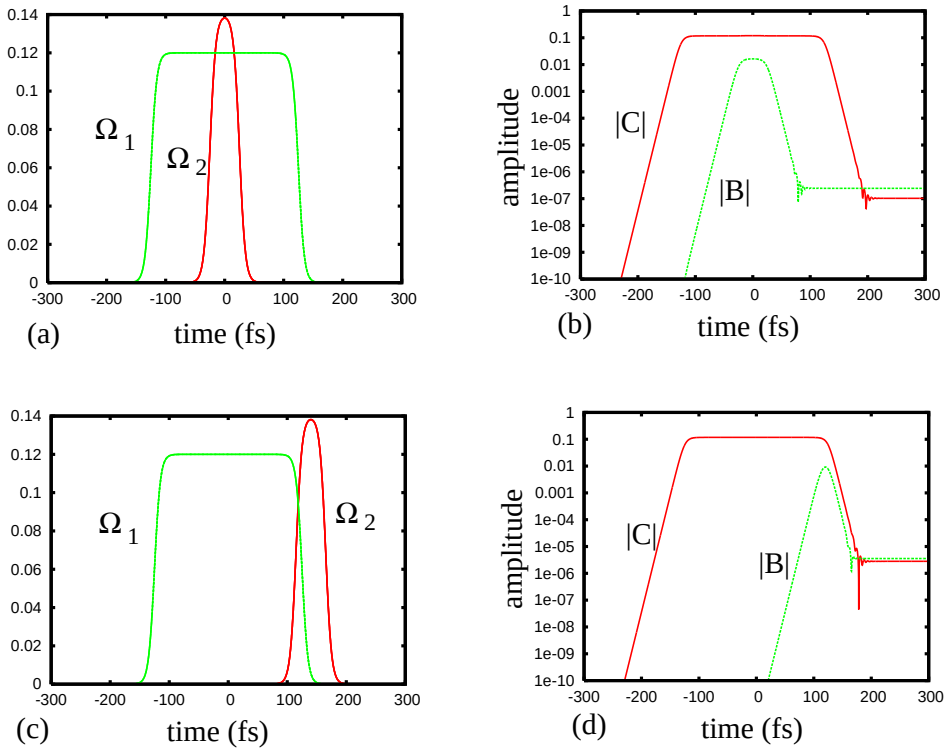

Fig. 37. Time dependence of pulses $\Omega_1(t)$ and $\Omega_2(t)$ (in fs^{-1}) and amplitudes for levels $|b>$ and $|c>$ for two cases. In the first case $\Omega_1(t)$ and $\Omega_2(t)$ both have maxima at $t = 0$ (a). The corresponding amplitudes are shown in (b). Coherence left in the level $|b>$ is $B(+\infty) = 1 \times 10^{-7}$. In the second case the pulse $\Omega_2(t)$ is delayed with respect to $\Omega_1(t)$ (c). The corresponding amplitudes are pictured in (d), $B(+\infty) = 3 \times 10^{-6}$. The excited coherence for the delayed pulses is 30 times larger. In last case $\frac{\Omega_1}{\Delta} = 0.12$ and $\frac{\Omega_2}{\Delta} = 0.14$ while $\alpha_1 = \alpha_2 = 0.1$.

frequency term remains. However, if we break adiabatic following, e.g., by making the turn on time $\tau = 1/\alpha$ small enough, we can arrange to leave the atom partially excited after the pulse is past, see Fig. 37.

Having set the stage, we now proceed to investigate breaking of adiabaticity as a means of enhancing ρ_{bd}. In particular, we propose to drive the atom from $|c\rangle$ to $|b\rangle$ by means of an attosecond π pulse, i.e., we tailor $\Omega_2(t)$ such that $\Omega_{20}\tau_2 \simeq \pi$. Thus

we next consider the driven three level problem described by the state vector

$$|\Psi\rangle = B(t)e^{-i\omega_b t}|b\rangle + C(t)e^{-i\omega_c t}|c\rangle + D(t)|d\rangle \ . \tag{5.10}$$

We assume that $c-b$ transition is driven in resonance by pulse $\Omega_2(t)$ with frequency $\nu_2 = \omega_b - \omega_c$. $\Omega_2(t)$ only couples levels $|b>$ and $|c>$, while $\Omega_1(t)$ couples $|c>$ and $|d>$. In the rotating wave approximation the atomic evolution is described by the following equations

$$\dot{B} = -i\Omega_2(t)C \tag{5.11a}$$

$$\dot{C} = -i\Omega_2^*(t)B - i\Omega_1(t)e^{-i\Delta t}D \tag{5.11b}$$

$$\dot{D} = -i\Omega_1^*(t)e^{i\Delta t}C. \tag{5.11c}$$

First we apply the pulse $\Omega_1(t) = \Omega_{10}[1+\tanh(\alpha t)]$ and turn on $\Omega_2(t)$ when $\Omega_1(t)$ is saturated (that is at $t \gg 1/\alpha$). If the pulse $\Omega_1(t)$ is adiabatic then $C(t)$ is given by Eq. (5.9), the second term is exponentially small, and we omit it. Then $B(t)$ evolves as

$$\frac{B(t)}{D(t)} \approx -2i\frac{\Omega_{10}}{\Delta}\int_{-\infty}^{t} dt'\Omega_2(t')e^{-i\Delta t'}. \tag{5.12}$$

For example, if we take $\Omega_2(t) = \Omega_{20}\ \mathrm{sech}[\alpha(t-t_0)]$ (where $t_0 \gg 1/\alpha$) and ask for $B(t)$ at times $t-t_0$ large compared to α^{-1} we find

$$|B| \approx \frac{\Omega_{10}\Omega_{20}}{\Delta\alpha}\frac{2\pi}{\cosh(\pi\Delta/2\alpha)}. \tag{5.13}$$

To estimate the magnitude of (5.13), let us consider the example of a pulse with a few cycle (attosecond) raise time for which $\alpha \simeq \nu_2$. Then for the previous case of Hydrogen, in which we take $\Delta/\nu_2 \simeq 5$, we have $[\cosh 5\pi/2]^{-1} = 7.7\times10^{-4}$ and for Helium, for which $\Delta/\nu_2 \simeq 10$, we have $[\cosh 5\pi]^{-1} = 3.0\times10^{-7}$ and the attosecond Raman coherence for hydrogen and helium is then of order 10^{-7} and 10^{-10} respectively.

For multiphoton excitation, the hydrogen and helium Raman coherence is of order 10^{-10} and 10^{-20}. In both multiphoton and attosecond examples, we take $\frac{\Omega_{10}}{\Delta} = 10^{-2}$, $\frac{\Omega_{10}}{\alpha} = 10^{-1}$ and $\frac{\Delta}{\alpha} \simeq 5$ for hydrogen and 10 for helium.

It is important to note that while $\rho_{bd} \sim B$ given by Eq. (5.13) goes as $e^{-\pi\Delta/2\alpha}$ for a sech(αt) pulse; ρ_{bd} goes as $e^{-\Delta^2/\alpha^2}$ for a Gaussian $e^{-\alpha^2 t^2}$ pulse. The pulse shape, as well as the width, is crucial. This and other important issues such as the rotating wave approximation etc, will be discussed at length elsewhere.

We conclude this discussion of adiabatic behavior by comparing the previous analytical result with numerical simulations ("computer experiment") in which we take pulses 1 and 2 to have the form

$$\Omega_i(t) = \Omega_{i0}\frac{1}{2}\left[\tanh\left[\alpha_{i,a}\left(t + \frac{T_i}{2}\right)\right] + \tanh\left[\alpha_{i,b}\left(\frac{T_i}{2} - t\right)\right]\right] . \tag{5.14}$$

In simulations we take $T_1 = 250\frac{1}{\Delta}$, $T_2 = 50\frac{1}{\Delta}$, $\alpha_{1a} = \alpha_{1b} = 0.03\Delta$, $\alpha_{2a} = 0.08\Delta$, $\alpha_{2b} = 0.16\Delta$. The numerical results are in agreement with the (approximate) analytical solutions. Figure 37 shows amplitudes $|B|$ and $|C|$ vs time for two cases. In the first case $\Omega_1(t)$ and $\Omega_2(t)$ both have maxima at $t = 0$. In the second case the pulse $\Omega_2(t)$ is delayed with respect to $\Omega_1(t)$ which results in greater population left in the level $|b>$.

D. Discussion and Conclusions

Comparison with nonlinear upconversion: The present approach to XUV generation differs from conventional sum frequency up conversion several ways. For example, the present conversion frequency is larger than the usual (nonresonant) NLO process. Furthermore, the present Raman superradiant process has a very different physical basis and temporal behavior. In conventional NLO all fields are present simultane-

ously whereas in the present approach the Raman coherence ρ_{db} can be prepared and the prep lasers shut off before the drive field, at ν_3, is turned on. This can, and does, provide an extra control feature.

The generation of Raman coherence via breaking of adiabaticity is another feature made possible by attosecond pulses. For example, the timing of the π pulse reative to the nonresonant drive pulse shows temporal behavior (see Fig.7) which would not be anticipated from the usual NLO perspective.

Raman vs cascade superradiance: As has been emphasized in Section II on coherent Raman superradiance, conventional Dicke superradiance requires population inversion and a build up time of some picoseconds. Raman superradiance, on the other hand, does not require a population inversion and does not require a build up time.

Cascade superradiance, in which population inversion is established on some level relative to another intermediate level, is closer to the (hyper) Raman superradiance discussed here. For example, the beautiful experiments of Hartmann and co-workers [94] in a three level system in which the superradiance on the upper two levels is followed by superradiance on the lower two. Again, however, gain and a build up time are rquired.

In recent experiments we have found that yoked superradiance in ^{87}Rb builds up in some 10's of picoseconds. Raman superradiance, however, is essentially simultaneous with the driving pulse.

Coherent control via breaking of adiabaticity: The use of edge effects and pulse shaping has both simple and subtle features. It is easy to see that without some sort of intervention the atom will return to the ground state after the $\Omega_1(t)$ pulse passes, when applying the Hahn - McCall 2π pulse in which $\Omega(t) = \Omega_0 \,\mathrm{sech}\Omega_0 t$.

Using a resonant π pulse, i.e. taking $\theta_2 = \int_{-\infty}^{\infty} dt' \,\Omega_2(t') = \pi$, together with the intense Ω_1 pulse has interesting features. First of all breaking adiabaticity with a

sharp edge on the Ω_2 pulse allows for the selective coherent population of state $|b\rangle$. That is, if we use a shape edged $\Omega_1(t)$ arrangement then we would excite many states (not just $|c\rangle$). However, when using the Ω_1 and Ω_2 combination, we can preferentially select $|b\rangle$.

Another point that should be mentioned is the misconception that the "edge effects are just giving us the high frequency needed to make the $d \rightarrow c$ transition possible". While this is a sometimes useful observation, it is overly simplistic. The real physics is in the breaking of adiabatic following. For example, suppose we turn off the field coupling by (e.g. switching off the matrix element $\wp$). Then we would break adiabaticity but the "high frequency photons generated by sharp edges" picture does not apply.

Experiment Attempt: The experiment group at TaMU already conduct experiments on Rb gas support the present theoretical results. In particular we prepare coherence on the 5D ($|c\rangle$ state) and then apply a time delayed pulse to the 12P ($|b\rangle$ state). Several characteristic behavior has been observed. Similar experiment has been carrier out by EEEE et al in the context of tunable coherent XUV source[108].

CHAPTER VI

SUMMARY

In summary, we study the cooperative effect in the spontaneous emission process of multi-atoms. Particularly, we study the dynamics of the cooperative spontaneous radiation from an ensemble of N atoms which is uniformly excited by absorbing a single photon. We reveal that there are two different regimes in which the system exhibits totally different behaviors. One of them is the superradiance type of behavior: the system decays much quicker than single atom decay, with a decay rate proportional to $N(\lambda/R)^2$, where N is the atom numbers, R is the size of the atom cloud, and λ is the wavelength. We call it Markovian regime because the sytem does not persist memory effect. The other regime is called non-Markovian regime and the system oscillates with effective Rabi oscillation frequency Ω while slowly decaying with a rate proportional to the photon escaping rate. The effective Rabi oscillation is a new type of dynamics which analogs well known Cavity QED behavior.

In the Markovian regime, we study the system dynamics as a many-body eigenfunction and eigenvalue problem. For a dense cloud, we find analytical solutions for the eigenstates and corresponding eigenvalues, which can help to generally describe the system dynamics for any initial conditions in this regime.

One of the applications of the cooperative effect is in atom microscopy. We propose a scheme to measure the distance between two atoms/molecules beyond diffraction limit. It covers the whole range from half the wavelength to sub-nanometers, utilizing both the atom localization technique and the collective frequency shift effect due to the cooperative effect in the radiation of the two atoms. We also propose a scheme to generate Coherent XUV radiation using Raman-type superradaince.

REFERENCES

[1] R.H. Dicke, Phys. Rev. **93**, 99 (1954).

[2] G. S. Agarwal, Phys. Rev. **178**, 2025(1969); Phys. Rev. A, **2**, 2038(1970); Phys. Rev. A, **4**, 1778(1971); Phys. Rev. A, **7**, 1195(1973).

[3] F. T. Arrechi and E. Courtens, Phys. Rev. A, **2**, 1730 (1970).

[4] N. E. Rehler and J. H. Eberly, Phys. Rev. A **3**, 1735 (1971).

[5] A. V. Andreev, Sov. J. Quantum Electron. **8**, 476 (1978).

[6] R. Bonifacio and L.A. Lugiato, Phys. Rev. A **11**, 1507 (1975). See also Opt. Commun. **19**, 172 (1976); Phys. Rev. A **18**, 1129 (1978).

[7] J. C. MacGillivray and M. S. Feld, Phys. Rev. A, **14**, 1169 (1976).

[8] E. L. Hahn, Phys. Rev. **80**, 580(1950).

[9] N. Skribanowitz, I. P. Herman, J. C. MacGillivray, and M. S. Feld, Phys. Rev. Lett. **30**, 309 (1973).

[10] Ph. Cahuzak, H. Sontag and P.E. Toschek, Opt. Comm. **31**, 37(1979).

[11] S. Liberman and P. Pillet, Phys. Rev. Lett. **41**, 1237(1978).

[12] M. Gross, C. Fabre, P. Goy, S. Haroche and J.M. Raimond, Phys. Rev. Lett. **43**, 343(1979).

[13] R. I. Karasik, K. Marzlin, B. C. Sanders, and K. B. Whaley, Phys. Rev. A **76**, 012331 (2007).

[14] H. Hammer, Opt. Spectrosc. **99**, 320 (2005).

[15] J. P. Clemens, L. Horvath, B. C. Sanders, and H. J. Carmichael, Phys. Rev. A **68**, 023809 (2003).

[16] A. Gorshkov, A. André, M. Fleishauer, A. Sorensen, and M. Lukin, to be published.

[17] T. Chanelire, D. N. Matsukevich, S. D. Jenkins, S.-Y. Lan, T. A. B. Kennedy and A. Kuzmich, Nature **438**, 833 (2005).

[18] A. Kuzmich, W.P. Bowen, A.D. Boozer, A. Boca, C.W. Chou, L.M. Duan and H.J. Kimble, Nature **423**, 731 (2003); C.W. Chou, S.V. Polyakov, A. Kuzmich and H.J. Kimble, Phys. Rev. Lett. **92**, 213601 (2004); C.W. Chou, J. Laurat, H. Deng, K.S. Choi, H. de Riedmatten, D. Felinto, H.J. Kimble, Science **316**, 1316 (2007).

[19] A. T. Black, J. K. Thompson, and V. Vuletić, Phys. Rev. Lett. **95**, 133601 (2005).

[20] M. Scully, E. Fry, C.H.R. Ooi and K. Wodkiewicz, Phys. Rev. Lett. **96**, 010501 (2006).

[21] M. Scully, Laser Phys. **17**, 635 (2007) .

[22] I. E. Mazets and G. Kurizki, J. Phy. B: At. Mol. Opt. Phys. **40**, 105 (2007).

[23] R. H. Dicke, Quantum Electronics, proceedings of the third international congress, Columbia University Press, New York (1964).

[24] F.W. Cummings, Phys. Rev. A **33**, 1683 (1986); F.W. Cummings, Phys. Rev. Lett. **54**, 2329 (1985); F.W. Cummings and A. Dorri, Phys. Rev. A **28**, 2282 (1983).

[25] G. Benivegna ad A. Messina, Phys. Lett. A **126**, 249 (1988).

[26] V. Buzek, G. Drobny, M. G. Kim, M. Havukainen, and P. L. Knight, Phys. Rev. A **60**, 582 (1999).

[27] V. Buzek, Phys. Rev. A **39**, 2232 (1989).

[28] V. Ernst, Z. Physik **218**, 111(1969).

[29] B. R. Mollow, Phys. Rev. **188**, 1969 (1969).

[30] G. S. Agarwal, A. C. Brown, L. M. Narducci, and G. Vetri, Phys. Rev. A **15**, 1613 (1977).

[31] A. S. Jahangir Amin and J. G. Cordes, Phys. Rev. A **18**, 1298 (1978).

[32] G. Lenz and P. Meystre, Phys. Rev. A **48**, 3365 (1993).

[33] T. Richter, Opt. Acta, **30**, 1769 (1983).

[34] H. S. Freedhoff, Phys. Rev. A **19**, 1132 (1979); R. D. Griffin and S. M. Harris, Phys. Rev. A **25**, 1528 (1982).

[35] Z. Ficek, R. Tanaś, and S. Kielich, Opt. Acta, **30**, 713 (1983).

[36] Z. Ficek and R. Tanaś, Phys. Reports, **372**, 369 (2002).

[37] M. Macovei and C. H. Keitel, Phys. Rev. Lett. **91**, 123601 (2003).

[38] G. C. Hegerfeldt and D. Seidel, J. Opt. B: Quantum Semi. Opt. **4** 245 (2002).

[39] C. Skornia, J. van Zanthier, G. S. Agarwal, E. Werner, and H. Walther, Phys. Rev. A, **64** 063801 (2001).

[40] M. O. Scully and C. H. Raymond Ooi, J. Opt. B: Quantum Semiclass. Opt. **6**, S575(2004).

[41] M. Minsky, Microscopy Apparatus. US patent No. 3013467(1957).

[42] S. W. Hell, Nature Biotechnology, **21**, 1347 (2003).

[43] U. W. Rathe and M. O. Scully, Lett. Math. Phys. **34**, 297 (1995); A. N. Boto *et al.*, Phys. Rev. Lett. **85**, 2733 (2000); M. D'Angelo, M. V. Chekhova and Y. Shih, *ibid.* **87**, 013602 (2001).

[44] M. O. Scully and K. Drühl, Phys. Rev. A **25**, 2208 (1982); M. O. Scully and C. H. Raymond Ooi, J. Opt. B: Quantum Semiclass. Opt. **6**, S816 (2004); A. Muthukrishnan, M. O. Scully and M. S. Zubairy, *ibid.* S575 (2004).

[45] W. Denk, J.H. Strickler and W.W. Webb, Science **248**, 73 (1990).

[46] A. Lewis, M. Isaacson, A. Harootunian, and A. Muray, , Ultramicroscopy **13**, 227 (1984); A. Lewis, H. Taha, A. Strinkovski, A. Manevitch, A. Khatchatouriants, R. Dekhter and E. Ammann, Nature Biotechnology **21**, 1378 (2003).

[47] C. Hettich, C. Schmitt, J. Zitzmann, S. Kuhn, I. Gerhardt, and V. Sandoghdar, Science **298**, 385 (2002).

[48] E. Betzig, Opt. Lett. **20**, 237 (1995).

[49] J.-T. Chang, J. Evers, M. O. Scully, and M. S. Zubairy, Phys. Rev. A in print (2006).

[50] T. Azim, M. Ikram, and M. S. Zubairy, J. Opt. B: Quantum Semiclass. Opt. **6**, 248 (2004); F. Ghafoor, S. Qamar, and M. S. Zubairy, Phys. Rev. A. **65**, 043819 (2002); S. Qamar, S.-Y. Zhu, and M. S. Zubairy, Phys. Rev. A **61**,

063806 (2000); F. L. Kien, G. Rempe, W. P. Schleich, and M. S. Zubairy, Phys. Rev. A, **56**, 2972 (1997); M. Sahrai, H. Tajalli, K. T. Kapale, and M. S. Zubairy, Phys. Rev. A, **72**, 013820(2005).

[51] M. O. Scully and M. S. Zubairy, *Quantum Optics*, (Cambridge University Press, Cambridge, England, 1997).

[52] L. Mandel and E. Wolf, *Optical Coherence and Quantum Optics*, (Cambridge University Press, England, 1995).

[53] G. Agarwal, *Quantum Statistical Theories of Spontaneous Emission* in Springer Tracts in Modern Physics, vol. 70 (Springer-Verlag, Berlin, 1976).

[54] D.C. Burnham and R.Y. Chiao, Phys. Rev. **188**, 667 (1969).

[55] E. Ressayre and A. Tallet, Phys. Rev. A, **15**, 2410 (1977).

[56] A. V. Andreev, V. I. Emel'yanov, and Yu. A. II'inskii, Usp. Fiz. Nauk **131**, 653(1980) (Sov. Phys, Usp. **23 (8)**, 493 (1980));A. V. Andreev, Zh. Eksp. Teor. Fiz. **72**, 1397 (1977)[Sov. Phys. JETP **45**, 734 (1977)]; A. V. Andreev, Kvantovaya Elektron. (Moscow) **5**, 830 (1978) [Sov. J. Quantum Electron. **8** , 476 (1978)].

[57] R. H. Lehmberg, Phys. Rev. A, **2**, 883 (1970).

[58] W. Heitler, *The Quantum Theory of Radiation* (3rd edition), (Oxford Press, London, 1954).

[59] P. W. Milonni and P. L. Knight, Phys. Rev. A **10**, 1096 (1974).

[60] G. Lenz and P. Meystre, Phys. Rev. A **48**, 3365 (1993).

[61] R. H. Lehmberg, Phys. Rev. A **2**, 883 (1970).

[62] R. Friedberg and S. R. Hartmann and J. T. Manassah, Phys. Rep. **7**, 101 (1973).

[63] Z. Ficek, R. Tanas, and S. Kielich, Physica A **146**, 452 (1987).

[64] I.S. Gradshteyn and I.M. Ryzhik, *Table of Integrals, Series and Products* (4th edition), (Academic Press, London, 1980).

[65] Milton Abramowitz and Irene A. Stegun, *Handbook of Mathematical Functions: with Formulas, Graphs, and Mathematical Tables* (10th edition), (Dover Publications, 1965).

[66] Anatoly Svidzinsky, J.-T. Chang, and M. O. Scully, to be published.

[67] M.J. Stephen, J. Chem. Phys. **40**, 669 (1964); C.S. Chang and P. Stehle, Phys. Rev. A **4**, 630 (1971); P.W. Milonni and P.L. Knight, Phys. Rev. A **10**, 1069 (1974); R. Bonifacio, H. Hopf, P. Meystre and M. Scully, Phys. Rev. A **12**, 2568 (1975).

[68] E.R. Buley and F.W. Cummings, Phys. Rev. **134**, A1454 (1964); V. Ernst and P. Stehle, Phys. Rev. **176**, 1456 (1968); C.R. Stroud, J.H. Eberly, W.L. Loma and L. Mandel, Phys. Rev. A **5**, 1094 (1972); J.H. Eberly, J. Phys. B: At. Mol. Opt. Phys. **39**, S599 (2006).

[69] For a discussion of the closely related problem of N atoms or nuclei interacting with $X-$ray radiation see, e.g., U. van Bürck, D. Siddons, J. Hastings, U. Bergmann, and R. Hollatz, Phys. Rev. B **46**, 6207 (1992); Y. Kagan, Hyperfine Int. **123**, 83 (1999); H.J. Lipkin, Phys. Rev. Lett. **58**, 1176 (1987); G.T. Trammel and J.P. Hannon, Phys. Rev. B **18**, 165 (1978); Phys. Rev. Lett. **61**, 653 (1988) and references therein.

[70] K. S. Johnson, J. H. Thywissen, N. H. Dekker, K. K. Berggren, A. P. Chu, R. Younkin, and M. Prentiss, Science **280**, 1583 (1998); V. Westphal and S. W. Hell, Phys. Rev. Lett. 94, 143903 (2005).

[71] J. E. Thomas and L. J. Wang, Phys. Rep. **262**, 311 (1995).

[72] P. Storey, M. Collet, and D. F. Walls, Phys. Rev. Lett. **68**, 472 (1992); M. A. M. Marte and P. Zoller, Appl. Phys. B: Photophys. Laser Chem. **54**, 477 (1992).

[73] R. Quadt, M. Collett, and D. F. Walls, Phys. Rev. Lett. **74**, 351 (1995); A. M. Herkommer, H. J. Carmichael, and W. P. Schleich, Quantum Semiclassic. Opt. **8**, 189 (1996).

[74] J. E. Thomas, Phys. Rev. A **42**, 5652 (1990); K. D. Stokes, C. Schnurr, J. R. Gardner, M. Marable, G. R. Welch, and J. E. Thomas, Phys. Rev. Lett. **67**, 1997 (1991); J. R. Gardner, M. L. Marable, G. R. Welch, and J. E. Thomas, Phys. Rev. Lett. **70**, 3404 (1993).

[75] S. Kunze, K. Dieckmann, and G. Rempe, Phys. Rev. Lett. **78**, 2038 (1997);

[76] F. L. Kien, G. Rempe, W. P. Schleich, and M. S. Zubairy, Phys. Rev. A **56**, 2972 (1997).

[77] S. Kunze, G. Rempe, and M. Wilkins, Europhys. Lett. **27**, 115 (1994).

[78] A. M. Herkommer, W. P. Schleich, and M. S. Zubairy, J. Mod. Opt. **44**, 2507 (1997); S. Qamar, S.-Y. Zhu, and M. S. Zubairy, Opt. Commun. **176**, 409 (2000); E. Paspalakis and P. L. Knight, Phys. Rev. A **63**, 065802 (2001).

[79] S. Qamar, S.-Y. Zhu, and M. S. Zubairy, Phys. Rev. A. **61**, 063806 (2000);

[80] E. Betzig, Opt. Lett. **20**, 237 (1995).

[81] T. G. Rudolph, Z. Ficek, and B. J. Dalton, Phys. Rev. A **52**, 636 (1995); J. G. Cordes and W. Roberts, Phys. Rev. A **29**, 3437 (1984).

[82] P. W. Milonni and P. L. Knight, Phys. Rev. A **10**, 1096 (1974).

[83] F. Ghafoor, S. Qamar, and M. S. Zubairy, Phys. Rev. A **65**, 043819 (2002); M. Sahrai, H. Tajalli, K. T. Kapale, and M. S. Zubairy, Pys. Rev. A **72**,013820 (2005).

52, 636 (1995); J. G. Cordes and W. Roberts, Phys. Rev. A **29**, 3437 (1984).

[84] J. Evers, M. Kiffner, M. Macovei and C. H. Keitel, Phys. Rev. A **73**, 023804 (2006).

[85] Z. Ficek and S. Swain, *Quantum Interference and Coherence: Theory and Experiments*, (Springer, Berlin, 2005).

[86] G. S. Agarwal, Quantum Optics, in *Springer Tracts in Modern Physics*, vol. 70, (Springer, Berlin, 1974).

[87] H. Steudel and Th. Richter, Ann. Phys. (Leipzig) **35**, 122 (1978).

[88] O. Kocharovskaya, *Phys. Rep.*, **219**, 175 (1992); S.E. Harris, *Physics Today*, **50**, 36 (1997).

[89] R. W. Boyd, *Nonlinear Optics*, (Academic Press, Boston, 1992).

[90] G. I. Petrov, R. Arora, V. V. Yakovlev, Xi Wang, A. V. Sokolov, and M. O. Scully, PNAS, **104**, 7776 (2007).

[91] I.P. Herman, J. C. MacGillivray, N. Skribanowitz and M.S. Feld, *Laser Spectroscopy,* edited by R.J. Brewer and A. Mooradian (Plenum, New York, 1974).

[92] N.E. Rehler and J.H. Eberly, Phys. Rev. A **3**, 1735 (1971).

[93] R. Bonifacio and P. Schwendimann, Phys. Rev. A, **4**, 302 (1971); R. Bonifacio, P. Schwendimann and F. Haake, Phys. Rev. A, **4**, 854 (1971).

[94] J.H. Brownell, X. Lu, and S. R. Hartmann, Phy. Rev. Lett. **75**, 3265 (1995); X. Lu, J. H. Brownell, and S. R. Hartmann, Laser Phys. **5**, 526 (1995).

[95] M. Gross, C. Fabre, P. Pillet and S. Haroche, Phys. Rev. Lett. **36**, 1035 (1976).

[96] A. Flusberg, T. Mossberg and S.R. Hartmann, Phys. Lett. **58A**, 373 (1976); Phys. Rev. Lett. **38**, 59 (1977).

[97] M. Gross, J.M. Raimond, and S. Haroche, Phys. Rev. Lett. **40** 1711 (1978).

[98] A. Crubellier, S. Liberman and P. Pillet, Phys. Rev. Lett. **41**, 1237 (1978).

[99] E. Ressayre and A. Tallet, Phys. Rev. Lett. **30**, 1239 (1973); **37**, 424 (1976); Phys. Rev. A **15**, 2410 (1977).

[100] R. Glauber and F. Haake, Phys. Lett. 68A, 29 (1978); F. Haake, Phys. Rev. Lett. 41, 1685 (1978); F. Haake, J. Haus, H. King, G. Schroder and R. Glauber, Phys. Rev. A **20,** 2047 (1979).

[101] F. Haake, H. King, G. Schroder, J. Haus, R. Glauber, and F. Hopf, Phys. Rev. Lett. **42,** 1740 (1979); **45**, 558 (1980).

[102] M.F.H. Schuurmans, D. Polder and Q.H.F. Vrehen, J. Opt. Soc. Am. **68**, 699 (1978); D. Polder, M.F.H. Schuurmans and Q.H.F. Vrehen, Phys. Rev. A **19**, 1192 (1979); Q.H.F. Vrehen and J.J. der Weduwe, Phys. Rev. A **24**, 2857 (1981). (1976).

[103] C.R. Stroud, J.H. Eberly, W.L. Lama and L. Mandel, Phys. Rev. A **5**, 1094 (1972).

[104] V. Ernst and P. Stehle, Phys. Rev. **176**, 1456 (1968).

[105] F.T. Arrechi and E. Courtens, Phys. Rev. A **2**, 1730 (1970).

[106] J.H. Eberly, Am. J. Phys. **40**, 1374 (1972).

[107] J. Okada, K. Ikeda, and M. Matsuoka, Opt. Commun. **27**, 321 (1978); K. Ikeda, J. Okada, and M. Matsuoka, J. Phys. Soc. Jpn. **48**, 1636 (1980).

[108] R. T. Hodgson, P. P. Sorokin, and J. J. Wynne, Phys. Rev. Lett. **32**, 343 (1974).

APPENDIX A

SOLUTION OF INTEGRAL EQUATION

We introduce $x = k_0 r$ and rewrite Eq. (3.30) as

$$\frac{4\pi}{k_0^3}\frac{N}{V}\int_0^{k_0 R} dx' x'^2 \beta(x') \begin{cases} j_n(x') h_n^{(1)}(x)/j_n(x), & x > x' \\ h_n^{(1)}(x'), & x \le x' \end{cases} = \frac{\lambda_n}{j_n(x)}\beta(x). \tag{A.1}$$

Taking derivative over x from both sides of Eq. (A.1) we obtain

$$\frac{4\pi}{k_0^3}\frac{N}{V}\left[\frac{h_n^{(1)}(x)}{j_n(x)}\right]' \int_0^x dx' x'^2 j_n(x')\beta(x') = \lambda_n \frac{d}{dx}\left[\frac{\beta(x)}{j_n(x)}\right]. \tag{A.2}$$

Then, taking into account that

$$\frac{d}{dx}\left[\frac{h_n^{(1)}(x)}{j_n(x)}\right] = \frac{i}{x^2 j_n^2(x)}$$

we rewrite Eq. (A.2) as

$$i\int_0^x dx' x'^2 j_n(x')\beta(x') = \tilde{\lambda}_n x^2 j_n^2(x)\frac{d}{dx}\left[\frac{\beta(x)}{j_n(x)}\right]. \tag{A.3}$$

where

$$\tilde{\lambda}_n = \frac{k_0^3 V}{4\pi N}\lambda_n = \frac{k_0^3 R^3}{3N}\lambda_n.$$

Differentiation Eq. (A.3) over x yields

$$i x^2 j_n(x)\beta(x) = \tilde{\lambda}_n \frac{d}{dx}\left\{x^2 j_n^2(x)\frac{d}{dx}\left[\frac{\beta(x)}{j_n(x)}\right]\right\}. \tag{A.4}$$

Taking into account

$$\frac{d}{dx}\left\{x^2 j_n^2(x)\frac{d}{dx}\left[\frac{\beta(x)}{j_n(x)}\right]\right\} = j_n(x)[x^2\beta''(x) + 2x\beta'(x) + (x^2 - n^2 - n)\beta(x)]$$

Eq. (A.4) reduces to

$$x^2\beta''(x) + 2x\beta'(x) + \left[x^2\left(1 - \frac{i}{\tilde{\lambda}_n}\right) - n^2 - n\right]\beta(x) = 0. \tag{A.5}$$

General solution of Eq. (A.5) is

$$\beta(x) = C_1 j_n(ax) + C_2 h_n^{(1)}(ax), \tag{A.6}$$

where

$$a = \sqrt{1 - \frac{i}{\tilde{\lambda}_n}}. \tag{A.7}$$

One should take $C_2 = 0$ because integration with the Bessel function $h_n^{(1)}$ $(n > 0)$ in Eq. (A.1) diverges at $x' = 0$. So, the eigenfunction is

$$\beta(\mathbf{r}) = j_n(ak_0 r)\, Y_{nm}(\hat{r}). \tag{A.8}$$

Substitute (A.8) into Eq. (A.1) yields

$$\int_0^{k_0 R} dx' x'^2 j_n(ax') \begin{cases} j_n(x')h_n^{(1)}(x), & x > x' \\ j_n(x)h_n^{(1)}(x'), & x \le x' \end{cases} = \tilde{\lambda}_n j_n(ax). \tag{A.9}$$

Integral in Eq. (A.9) can be calculated using

$$\int dx x^2 j_n(ax)\, j_n(x) = \frac{x^2}{1-a^2}\left[a j_n(x)\, j_{n-1}(ax) - j_{n-1}(x)\, j_n(ax)\right], \tag{A.10}$$

$$\int dx x^2 j_n(ax)\, h_n^{(1)}(x) = \frac{x^2}{1-a^2}\left[a h_n^{(1)}(x)\, j_{n-1}(ax) - h_{n-1}^{(1)}(x)\, j_n(ax)\right], \tag{A.11}$$

and an identity

$$j_n(x)\, h_{n-1}^{(1)}(x) - h_n^{(1)}(x)\, j_{n-1}(x) = \frac{i}{x^2}. \tag{A.12}$$

This results in

$$\int_0^{k_0R} dx' x'^2 j_n\left(ax'\right) \begin{cases} j_n(x')h_n^{(1)}(x), & x > x' \\ j_n(x)h_n^{(1)}(x'), & x \leq x' \end{cases} =$$

$$= \tilde{\lambda}_n j_n\left(ax\right) + i(k_0R)^2 \tilde{\lambda}_n j_n(x) \left[a h_n^{(1)}\left(k_0R\right) j_{n-1}\left(ak_0R\right) - h_{n-1}^{(1)}\left(k_0R\right) j_n\left(ak_0R\right) \right]. \tag{A.13}$$

We obtain that the integral equation is satisfied provided the last term in Eq. (A.13) is equal to zero. This yields the following equation for the eigenvalues

$$a = \frac{j_n\left(ak_0R\right)}{j_{n-1}\left(ak_0R\right)} \frac{h_{n-1}^{(1)}(k_0R)}{h_n^{(1)}(k_0R)}. \tag{A.14}$$

APPENDIX B

MATRIX ELEMENTS

The non-vanishing elements of vector $\mathbf{I}$ are $\mathbf{I}_1 = \imath\beta^*/2$, $\mathbf{I}_2 = -\imath\beta/2$, $\mathbf{I}_3 = \imath\beta_2^*/2$, $\mathbf{I}_4 = -\imath\beta_2/2$. The non-vanishing elements of matrix $\mathbf{M}$ are as follows:

$$\mathbf{M}_{(1,1)} = -(1+\Delta)\,, \qquad \mathbf{M}_{(1,3)} = -(1-\imath b)\,,$$
$$\mathbf{M}_{(1,5)} = -\imath\beta^*\,, \qquad \mathbf{M}_{(1,12)} = 2(a-\imath b)\,,$$
$$\mathbf{M}_{(2,2)} = -(1-\imath\Delta)\,, \qquad \mathbf{M}_{(2,4)} = -(a+\imath b)\,,$$
$$\mathbf{M}_{(2,5)} = \imath\beta\,, \qquad \mathbf{M}_{2,11} = 2(a+\imath b)\,,$$
$$\mathbf{M}_{(3,1)} = -(a-\imath b)\,, \qquad \mathbf{M}_{(3,3)} = -(1-\imath b)\,,$$
$$\mathbf{M}_{(3,6)} = -\imath\beta_2^*\,, \qquad \mathbf{M}_{(3,14)} = 2(a-\imath b)\,,$$
$$\mathbf{M}_{(4,2)} = -(a+\imath b)\,, \qquad \mathbf{M}_{(4,4)} = -(1-\imath\Delta)\,,$$
$$\mathbf{M}_{(4,6)} = \imath\beta_2\,, \qquad \mathbf{M}_{(4,13)} = 2(a+\imath b)\,,$$
$$\mathbf{M}_{(5,1)} = -\imath\beta/2\,, \qquad \mathbf{M}_{(5,2)} = \imath\beta/2\,,$$
$$\mathbf{M}_{(5,5)} = -2\,, \qquad \mathbf{M}_{(5,7)} = -(a+\imath b)\,,$$
$$\mathbf{M}_{(5,8)} = -(a-\imath b)\,, \qquad \mathbf{M}_{(6,3)} = \imath\beta_2^*/2\,,$$
$$\mathbf{M}_{(6,4)} = \imath\beta_2^*/2\,, \qquad \mathbf{M}_{(6,6)} = -2\,,$$
$$\mathbf{M}_{(6,7)} = -(a-\imath b)\,, \qquad \mathbf{M}_{(6,8)} = -(a+\imath b)\,,$$
$$\mathbf{M}_{(7,1)} = -\imath\beta_2/2\,, \qquad \mathbf{M}_{(7,4)} = \imath\beta^*/2\,,$$
$$\mathbf{M}_{(7,5)} = -(a+\imath b)\,, \qquad \mathbf{M}_{(7,6)} = -(a-\imath b)\,,$$
$$\mathbf{M}_{(7,7)} = -2\,, \qquad \mathbf{M}_{(7,11)} = -\imath\beta^*\,,$$
$$\mathbf{M}_{(7,14)} = \imath\beta_2\,, \qquad \mathbf{M}_{(7,15)} = 4a\,,$$

$$\mathbf{M}_{(8,2)} = \imath\beta_2^*/2\,, \qquad \mathbf{M}_{(8,3)} = -\imath\beta/2\,,$$

$$\mathbf{M}_{(8,5)} = -(a - \imath b)\,, \qquad \mathbf{M}_{(8,6)} = -(a + \imath b)\,,$$

$$\mathbf{M}_{(8,8)} = -2\,, \qquad \mathbf{M}_{(8,12)} = \imath\beta\,,$$

$$\mathbf{M}_{(8,13)} = -\imath\beta_2^*\,, \qquad \mathbf{M}_{(8,15)} = 4a\,,$$

$$\mathbf{M}_{(9,1)} = \imath\beta_2^*/2\,, \qquad \mathbf{M}_{(9,3)} = \imath\beta^*/2\,,$$

$$\mathbf{M}_{(9,9)} = -2(1 + \Delta)\,, \qquad \mathbf{M}_{(9,12)} = -\imath\beta^*\,,$$

$$\mathbf{M}_{(9,14)} = -\imath\beta_2^*\,, \qquad \mathbf{M}_{(10,2)} = -\imath\beta_2/2\,,$$

$$\mathbf{M}_{(10,4)} = -\imath\beta/2\,, \qquad \mathbf{M}_{(10,9)} = -2(1 - \imath\Delta)\,,$$

$$\mathbf{M}_{(10,10)} = \imath\beta\,, \qquad \mathbf{M}_{(10,13)} = \imath\beta_2\,,$$

$$\mathbf{M}_{(11,5)} = -\imath\beta_2/2\,, \qquad \mathbf{M}_{(11,7)} = -\imath\beta/2\,,$$

$$\mathbf{M}_{(11,10)} = -\imath\beta^*/2\,, \qquad \mathbf{M}_{(11,11)} = -(3 - \imath\Delta)\,,$$

$$\mathbf{M}_{(11,13)} = -(a - \imath b)\,, \qquad \mathbf{M}_{(11,14)} = \imath\beta_2\,,$$

$$\mathbf{M}_{(12,5)} = -\imath\beta_2^*/2\,, \qquad \mathbf{M}_{(12,8)} = \imath\beta^*/2\,,$$

$$\mathbf{M}_{(12,9)} = \imath\beta^*/2\,, \qquad \mathbf{M}_{(12,10)} = -\imath\beta/2\,,$$

$$\mathbf{M}_{(12,12)} = -(3 - \imath\Delta)\,, \qquad \mathbf{M}_{(12,14)} = -(a + \imath b)\,,$$

$$\mathbf{M}_{(12,15)} = \imath\beta_2^*\,, \qquad \mathbf{M}_{(13,6)} = -\imath\beta/2\,,$$

$$\mathbf{M}_{(13,8)} = -\imath\beta_2/2\,, \qquad \mathbf{M}_{(13,11)} = -(a - \imath b)\,,$$

$$\mathbf{M}_{(13,13)} = -(3 - \imath\Delta)\,, \qquad \mathbf{M}_{(13,15)} = \imath\beta\,,$$

$$\mathbf{M}_{(14,6)} = \imath\beta^*/2\,, \qquad \mathbf{M}_{(14,6)} = \imath\beta_2^*/2\,,$$

$$\mathbf{M}_{(14,9)} = -\imath\beta_2/2\,, \qquad \mathbf{M}_{(14,12)} = -(a + \imath b)\,,$$

$$\mathbf{M}_{(14,14)} = -(3 + \imath\Delta)\,, \qquad \mathbf{M}_{(14,15)} = -\imath\beta^*\,,$$

$$\mathbf{M}_{(15,11)} = \imath\beta_2^*/2\,, \qquad \mathbf{M}_{(15,12)} = -\imath\beta_2/2\,,$$

$$\mathbf{M}_{(15,13)} = \imath\beta^*/2\,, \qquad \mathbf{M}_{(15,14)} = -\imath\beta/2\,,$$

$$\mathbf{M}_{(15,15)} = -4\,.$$

VITA

Juntao Chang

Physics Dept. c/o Dr. M. Suhail Zubairy

Texas A&M University 4242

College Station, Texas 77843-4242

Education:

Texas A&M University, College Station, Texas

Ph.D. in Quantum Optics GPA: 3.9/4.0 Advisor: Dr. M. Suhail Zubairy

Institute of Physics, Chinese Academy of Sciences, Beijing, China

M.S. in Optics, GPA: 3.75/4.0 Advisor: Dr. Ling-An Wu

Physics Department, Peking University, Beijing, China

B.S. in Physics; B.S. in Economics (minor) GPA: 3.3/4.0

Selected Publications:

1. Anatoly A. Svidzinsky, Jun-Tao Chang and Marlan O. Scully, Phys. Rev. Lett. 100, 160504 (2008).

2. Anatoly Svidzinsky, Jun-Tao Chang, Phys. Rev. A. 77, 043833 (2008).

3. Jun-Tao Chang and M. Suhail Zubairy, Phys.Rev. A. 77, 012329 (2008).

4. J.-T. Chang, J. Evers, M. O. Scully, M. S. Zubairy, Phys. Rev. A 73, 031803 (R) (2006).

5. J.-T. Chang, J. Evers, M. S. Zubairy, Phys. Rev. A 74, 043820 (2006).